AFFDL-TR-68-102

TURBULENT BOUNDARY LAYER SKIN FRICTION, HEAT TRANSFER AND PRESSURE MEASUREMENTS ON HYPERSONIC INLET COMPRESSION SURFACES

M. O. Ryder, Jr.

Cornell Aeronautical Laboratory, Inc.

TECHNICAL REPORT AFFDL-TR-68-102

July 1968

Air Force Flight Dynamics Laboratory
Air Force Systems Command
Wright-Patterson Air Force Base, Ohio

NOTICES

When Government drawings, specifications, or other data are used for any purpose other than in connection with a definitely related Government procurement operation, the United States Government thereby incurs no responsibility nor any obligation whatsoever; and the fact that the Government may have formulated, furnished, or in any way supplied the said drawings, specifications, or other data, is not to be regarded by implication or otherwise as in any manner licensing the holder or any other person or corporation, or conveying any rights or permission to manufacture, use, or sell any patented invention that may in any way be related thereto.

This document has been approved for public release and sale; its distribution is unlimited.

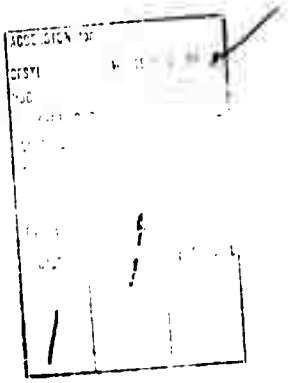

Copies of this report should not be returned unless return is required by security considerations, contractual obligations, or notice on a specific document.

TURBULENT BOUNDARY LAYER SKIN FRICTION, HEAT TRANSFER AND PRESSURE MEASUREMENTS ON HYPERSONIC INLET COMPRESSION SURFACES

M. O. Ryder, Jr.

FOREWORD

The experimental research effort reported herein was conducted by the Hypersonic Facilities Department of Cornell Aeronautical Laboratory of Cornell University, Buffalo, New York, for the Flight Dynamics Laboratory, Air Force Systems Command, United States Air Force, on Contract F33615-67-C-1203 of Project No. 1366. The contractor's report number is AF-2389-Y-3.

The work reported herein covers both phases of a two-phase program which began in January 1967 and was conducted under the technical cognizance of Mr. Dennis Sedlock of the Flight Dynamics Laboratory's Internal Aerodynamics Group. The final report was submitted in April 1968.

This technical report has been reviewed and is approved.

Philip P. Antonatos
Chief, Flight Mechanics Division
Air Force Flight Dynamics Laboratory

ABSTRACT

An experimental study of turbulent boundary layer flow, under the influence of adverse pressure gradients typical of hypersonic inlets, was conducted in the Cornell Aeronautical Laboratory 96-inch Leg of the Hypersonic Shock Tunnel on a two-dimensional and an axisymmetric model each instrumented with skin friction, heat transfer and pressure gages. Tests were conducted over a Mach and Reynolds number range of 6.74 to 11.37 and 1.05×10^6 per ft. to 2.93×10^7 per ft., respectively. These test conditions produced boundary layer transition on the forward portions of the models without resorting to artificial trips. It was possible to attain a fully turbulent boundary layer before the start of the adverse pressure gradient region for most of the axisymmetric model tests but for most of the two-dimensional tests, transition was not completed until after the start of the pressure gradient.

A comparison of the pressure data with the inviscid pressure distribution was made and good agreement is generally found indicating very little change in effective model shape due to boundary layer growth. This result is a consequence of the large model size relative to the boundary layer thickness, i.e., high Reynolds number flows over large models.

An important conclusion resulting from this program was that turbulent boundary layers can negotiate large adverse pressure gradients without separating. Comparison with some existing laminar boundary layer data indicate that a turbulent boundary layer can negotiate adverse pressure gradients at least an order of magnitude greater than those gradients which will separate a laminar layer.

TABLE OF CONTENTS

LIST OF TABLES

LIST OF ILLUSTRATIONS

LIST OF ILLUSTRATIONS (Cont.)

Figure

NOMENCLATURE AND SYMBOLS

Symbol		Unit
C_p	Specific heat at constant pressure	ft-lbs/slug-°R
H	Enthalpy	ft-lbs/slug
M	Mach number	
P	Pressure	psia
q	Dynamic pressure, $1/2\,\rho\,U^2$	psia
q	Heat transfer rate	Btu/ft^2-sec
Re/ft	Reynolds number per foot, $\frac{\rho U}{\mu}$	
T	Temperature	°R
U	Velocity	ft/sec
X	Axial distance from leading edge	inches
$\sqrt{C^*}$	Square root of the constant of proportionality in the linear viscosity law based on a reference temperature T*	
α	Angle of attack	degrees
μ	Absolute viscosity coefficient	slugs/ft-sec
ρ	Density	slugs/cu. ft
ϕ	Roll	degrees
ψ	Yaw	degrees
τ	Skin friction	psia

$$C^* = \frac{\mu}{\mu}^* \frac{T}{T^*}$$

Subscripts

AV	Average
i	Incident shock in shock tube
o	Nozzle reservoir conditions
o'	Stagnation conditions behind a normal shock
ts	Test section initial conditions
w	Initial conditions at wall
x	Axial distance from leading edge
∞	Free stream conditions
1	Initial driven tube conditions
4	Conditions behind reflected shock

Superscripts

*	Eckert reference temperature

BLANK PAGE

SECTION I

INTRODUCTION

Hypersonic inlet design and performance estimation are dependent upon a thorough knowledge of the boundary layer flow on the various compression surface comprising the inlet configuration. Boundary layer growth can alter the effective shape of the inlet giving a different shock wave pattern both at the leading edge of the inlet and internally with the result that the mass flow captured and the total pressure losses are both affected. In addition, boundary layer separation from the inlet compression surfaces may occur creating additional shock waves with further losses in total pressure. Boundary layer transition will occur, except at very high altitudes (>150K) and Mach numbers (>12), with a resultant increase in aerodynamic heating and skin friction drag. Despite the increased heating and drag, a turbulent boundary layer may be an asset because of its ability to negotiate larger adverse pressure gradients than laminar boundary layers can without separating. The wall skin friction of turbulent boundary layers in adverse pressure gradients comprises the subject matter of this report.

The effort reported herein is concerned with the experimental investigation of turbulent boundary layers on continuous compression surfaces at hypersonic Mach numbers under the influence of large adverse pressure gradients. Freestream conditions of sufficiently high Reynolds numbers were available to attain natural boundary layer transition within reasonable model lengths and thereby avoid introducing boundary layer trips as an influence in the experiments. Direct local skin friction measurements, in addition to pressure and heat transfer rates, were made on continuous compression surfaces to provide data which can be used to evaluate the applicability of existing turbulent boundary layer theories. In addition the data can be used to improve existing, or develop new, methods of predicting turbulent boundary layer characteristics.

SECTION II

TEST EQUIPMENT

1. CAL 96-INCH LEG OF THE HYPERSONIC SHOCK TUNNEL

The basic components of the 96-Inch Leg of the Hypersonic Shock Tunnel are shown in Figure 1. The tunnel employs a chambered reflected shock tube with a 5-inch inside diameter driver and a 4-inch inside diameter driven section. The driver tube is 16 feet long and is externally heated with a resistance heater up to temperatures of 1200°R. The driven tube length is 48.5 feet long and is always at the ambient temperature. The driver gas was a mixture of helium and air with a maximum helium purity of 98.5% while the driven gas was dry air. Steady flow test times of the order of 2 to 5 milliseconds, which allowed ample time to measure skin friction, pressure and heat transfer rates on the models, were achieved using the tailored-interface technique to be described later.

The long models tested in the present program made it desirable to avoid the streamwise pressure gradients typical of conical nozzle expansions. Consequently two axisymmetric contoured nozzles, providing parallel flow with no pressure gradients in the streamwise direction for several feet, were used for the expansion. One nozzle is designed for a Mach number of 8 and the other for 16. Both nozzles were used over a Mach number range by employing removable throat inserts of various diameters. Both nozzles have been calibrated, using pitot pressure survey rakes, over the range of operating conditions used in the subject program.

The test air expands through the nozzles into a 96-inch diameter test section in which the models are supported on an angle of attack sector as shown in Figures 2 and 3. Test air passes downstream of the test section into a receiver tank large enough to maintain flow for the desired duration. The models are isolated from tunnel accelerations by mounting the model support system on the laboratory floor and using a flexible bellows to provide a vacuum seal between the sector and the tunnel. The 16-inch diameter schlieren windows shown in the figures were used to obtain a single spark flow photograph for most runs of the test program.

2. SHOCK TUNNEL OPERATING PRINCIPLES

The shock tube is separated into regions of high and low pressure by a diaphragm (Figure 4). The wave phenomena begin with the rupture of the diaphragm, permitting expansion of the high-pressure driver gas into the lower pressure section and the generation of a shock wave which propagates through the low-pressure air. Between the shock wave and the gas interface (the contact surface separating the driver gas and the driven air) there exists a steady state region which is at a high temperature and pressure.

The downstream end of the shock tube is terminated by a convergent-divergent nozzle. The ratio of the nozzle throat area to the shock tube cross-sectional area is small, however, so that the primary shock wave is nearly completely reflected upstream from the throat, leaving a region of almost stagnant, compressed, and heated air at the end of the low-pressure section of the shock tube. This processed air is expanded through the nozzle to the desired test condition.

By proper control of the initial conditions in the driver and driven sections, the gas interface becomes transparent to the shock wave reflected upstream from the throat, i.e., no gasdynamic waves result from this interface-shock interaction that can subsequently disturb the steady test-air-supply conditions. Since the states of the gases on both sides of the interface must be carefully matched, this method is called the "tailored-interface" technique (Reference 1). The limiting wave, which then determines the maximum available testing times for the tailored-interface technique, is the leading expansion wave reflected from the driver end of the tube. The test times available are approximately eight times those achieved with the same length tube operating as a conventional nonreflected shock tunnel.

The temperature of the air behind the reflected shock in the driven section of the tube (corresponding to the "reservoir" or "supply" temperature in conventional wind tunnel terminology) is a function of the strength or velocity of the shock wave through the driven tube. If the stagnation temperature is to be duplicated at a given flight Mach number, the shock velocity or shock Mach number is then uniquely determined. The shock Mach number is, in turn, a function of the pressure ratio across the diaphragm for given driver gas mixtures and initial temperatures of the driver and driven gas. In order to tailor at various shock strengths, provision is made to vary the velocity of sound of the driver gas by mixing the driver gas with other gases and by heating.

3. MODELS

The models are of two basic shapes, two-dimensional (Phase I tests) and axisymmetric (Phase II tests) and are typical of the types of compression surfaces which might be used in hypersonic inlets. High shock losses at hypersonic speeds dictate that initial angles of inlet surfaces be small. Consequently the two-dimensional model has a sharp leading edge and an initial wedge angle of 3 degrees and the axisymmetric nose is a sharp hollow cylinder which was vented downstream of the model, allowing flow through the interior of the body. The aft regions of both models are designed for isentropic continuous compression which produces the adverse pressure gradient regions of interest in this test program.

a. Two-Dimensional Model, E-2

The two-dimensional model was designed and fabricated by the General Electric Company on Air Force Contract Number AF 33(675)-11747. This model, with a cowl attached, was tested by General Electric in their Missiles and Space Division shock tunnel facility. The G.E. test program (Reference 2) investigated cowl shock and compression surface laminar boundary layer interaction whereas the present tests are concerned with turbulent boundary layer characteristics under the influence of isentropic compression.

The two-dimensional model consisted of a wedge with an angle of 3° for the first 5 inches followed by a region designed for isentropic compression. The curved surface aerodynamic contours are based on a Method-of-Characteristics solution and laminar boundary layer analyses. Using the GE/Bertram viscous interaction program described in Reference 3, a solution for the upstream wedge region determined the boundary layer displacement thickness and surface pressure distribution. At the station 5 inches from the leading edge, the computed value of the Cohen and Reshotko (Reference 4) pressure gradient parameter, η , is -0.5 reflecting the viscous induced weak favorable pressure gradient. Aft of this 5 inch station η is varied linearly to a value of 0.12 at station 15 inches. Downstream of the 15-inch station the wall contour is designed to maintain a constant value of η of 0.12. The final wall angle was approximately 17.5 degrees. Photographs and drawings of the two-dimensional model comprise Figures 5 and 6, respectively. Locations of the model instrumentation are given in Figure 7.

b. Axisymmetric Model

The axisymmetric model was designed and fabricated by the Lockheed-California Company on Air Force Contract Number AF 33(657)-8833. This model was tested by Lockheed in the Arnold Engineering Development Center (AEDC) 50-inch diameter Tunnel B and the 40-inch Tunnel A, both of the von Karman Facility. The model was tested at Mach numbers of 5, 6 and 8 over a range of Reynolds numbers per foot of 1.6 to 6.9 million. Boundary layer trips were used for the AEDC tests whereas natural transition was achieved for the tests reported herein. Heat transfer and pressure data were obtained in the AEDC test which are reported in Reference 5.

The axisymmetric model consisted of a sharp leading edge hollow cylinder nose followed by an isentropic compression region which was designed for a focused isentropic compression at a Mach number of 8. The high rate of wall turning in the aft region of this model is readily apparent in the pressure data which will be discussed later. In addition, a blunt nose was provided to be interchanged with the sharp hollow nose to obtain blunt nose data. The downstream end of the model was terminated with a conical flare specifically designed to prevent the expansion from feeding upstream and modifying the boundary layer in the aft region. The final wall angle was approximately 30 degrees. Photographs and drawings of the axisymmetric model comprise Figures 8 and 9, respectively. Locations of the model instrumentation are given in Figure 10.

4. INSTRUMENTATION

a. Skin Friction

The large aerodynamic forces involved in this test program necessitated the development of a new high load skin friction gage with both a linear response to higher skin friction forces and a mechanically stronger gage structure to survive the large tunnel stopping loads experienced by the model and gages. Early attempts in this current program to use existing skin friction gages which had been previously used at lower Reynolds number conditions (Reference 6) indicated that these gages were not linear up to the maximum wall shear forces expected in this program and that they would not physically survive the environment. Hence a more rugged skin friction gage using the same basic principles as the existing gages was developed.

The CAL skin friction gage designed for this test employs the piezoelectric effect to convert a mechanical stress to an electric charge output. Lead zirconium titanate crystals are stressed by a force acting on a diaphragm and flexure system shown in Figure 11. Response is to a force applied tangentially to the diaphragm as shown by the arrow in Figure 11 indicating airflow direction. The flexures, which are cemented to the diaphragm and crystals with a high temperature bonding material, carry the skin friction force from the diaphragm to the crystals. These flexures are designed to be weak in bending to isolate the crystals from diaphragm warping which could be caused by pressure or thermal effects. Force normal to the diaphragm resulting from pressure loading is eliminated by allowing the gas to flow underneath the diaphragm and around the crystals. In addition, what little normal force does get to the crystal is in a direction in which the crystal has zero theoretical and little actual sensitivity. Using Invar for the diaphragm further reduces temperature effects by minimizing thermal warping which could transmit forces to the crystals. Compensation for acceleration effects is accomplished by an additional crystal and mass system which has the same acceleration sensitivity as the active system and is electrically wired in opposition to the active system.

The crystals are bimorph configurations which consist of two layers of lead zirconium titanate that have been polarized in opposite directions in order that the combination will be sensitive to bending in one plane but relatively insensitive to all other strains. They will, therefore, have little response to temperature change. The crystals are used in a cantilevered beam mode with one end rigidly bonded into the gage housing and the other end attached to the diaphragm. Two bimorphs are used in the active gage in order to make a stronger crystal-diaphragm structure. The crystals are coated with an electrical insulator to avoid effects of charged particles in the airflow.

In addition to developing a more rugged skin friction gage for this program, a new technique of mounting the gage in the model was used to isolate the gage from model accelerations. Although the internal acceleration compensation of the skin friction gage was generally sufficient to

eliminate errors due to acceleration from the average output during the test time, it was discovered that the gages were being physically damaged by accelerations of the model during tunnel flow breakdown (Figure 12(a)). These model accelerations were measured and were found to be many times greater than the accelerations experienced during the test time and to contain frequencies on the order of 10 to 12 kc which is approximately the natural frequency of the gages. The resulting resonance of the gages was felt to be largely responsible for the damage experienced. To isolate the instrumentation from the model excitation, a shock mount was designed and bench checked for the skin friction gage. This mount provided for rubber support of the gage with no metal-to-metal contact between the gage and the model. To further "de-tune" the gage from the model excitations, a mass was added to the back of the gage housing which lowered the natural frequency of the gage-mass system. Typical skin friction gage outputs during testing are indicated in Figure 12.

The new shock mounting system for the skin friction gages ensures that the gage unit is not stressed by the gage mounting and consequently the need to calibrate the gages after installation in the model is eliminated. Calibration of the gage outside the model was not only possible but desirable since, for concave curvatures, such as existed on these models, it is not possible to apply a purely tangential force to the gage diaphragms. The calibration consists of applying known forces to the diaphragms in the skin friction direction using weights. The gages were calibrated from .006 psi to 2.8 psi and were linear over this range to within ±2%.

The flat diaphragm shown in Figure 11 was used for model E-2 which had very little curvature over a surface distance in the flow direction of 1/4-inch. These same diaphragms were then hand-contoured to the local model radius for the axisymmetric model and again the surface contour over a length of 1/4-inch was neglected.

b. Heat Transfer

Heat transfer rates were determined by a technique that relies on sensing the transient surface temperature of the model. The sensing element is a thin platinum strip painted on a Pyrex substrate which conforms to the local model contour. The gage is then fired at controlled conditions, resulting in a thin film of metal, typically 0.1 micron thick by 5 mm by 0.5 mm, and fused to the Pyrex insert. Since the heat capacity of the gage is negligible, the film temperature is equal to the instantaneous surface temperature and is related to the heat transfer rate to the model by the theory outlined in Section V of this report and discussed in detail in Reference 7. Temperature histories from the platinum strips were fed into a passive analog network which produced a step output that was proportional to the heat transfer rate to the model. An IBM 360 computer program then uses the analog network output voltages to compute heat transfer rates. The computer automatically makes small corrections for the variation with temperature of the heat transfer gage substrate (Pyrex) properties and the nonlinear resistance-temperature characteristics of the platinum strip.

c. Pressure

The model pressures were measured with miniature ceramic piezoelectric crystal transducers. Their small size permits installation inside the model close to the orifice in the model surface, thus minimizing pneumatic lag. These transducers are available in several sizes and pressure ranges so that the type best suited for the estimated pressure range at a given model position can be used. Proper shielding of the sensing element precludes temperature effects during the short test time. In the transducer used to measure the pressures of the current program, a dual-element transducer was used to reduce acceleration effects to an indicated pressure of $\leq .0008$ psi/g. Pressures on the order of 0.1-60 psi were measured with this transducer. The pressure transducer indicates the pressure rise over the initial pre-run test section pressure which is usually on the order of 3 microns as determined by a Pirani vacuum gage which is periodically checked against a McLeod gage as a standard. The voltage output of each gage is calibrated against applied pressure through the model surface orifice after the gage has been installed in the model. Transducers are selected such that the voltage output is linear with pressure over the range of pressures encountered. Pressure transducers are normally calibrated before a series of runs. The details of the design, fabrication, and calibration of the pressure transducers used in the present test series are described in Reference 8.

d. Flow Visualization

Flow photographs were taken, either schlieren or shadowgraph, for both test phases using a single-pass parallel light system which viewed approximately the aft 16 inches on both models. This region of the models had the maximum adverse pressure gradient and consequently was of the most interest. The majority of the photographs were taken using shadowgraph since this system was superior to schlieren for observing the boundary layer. The schlieren system generally had too much sensitivity for these high density flows. The few schlieren photographs obtained were taken with the knife edge horizontal.

5. DATA ACQUISITION

The electrical signals from the heat transfer, skin friction and pressure transducers were recorded on 44 channels at 50-microsecond intervals on the magnetic storage drum of a Navigation Computer Corporation MCL-100 data acquisition system. The information was then transferred to magnetic tape for use as the input to the data reduction program. The data were also reproduced on a pen-type recorder for immediate examination and preliminary calculation.

SECTION III

TEST PROCEDURE

1. TEST PROGRAM

The two-dimensional and axisymmetric model test program and test conditions are presented in Tables I and V, respectively. The test program was specified by the Air Force Flight Dynamics Laboratory. Run 18, which is not shown in the test program, was an instrumentation diagnostic run which produced no model data. On Run 19, the first run on the axisymmetric model, most of the rearward data on the model were lost because the recording equipment gain settings were based on pretest estimates which proved to be too small in the aft region of the model.

2. CALIBRATION

The detailed calibration data are kept on file at CAL.

a. Skin Friction

The skin friction gages were calibrated using known weights to apply shear forces to the gage diaphragm. Gage outputs were displayed on oscilloscopes and photographed using Polaroid cameras. Dividing the weights by the area of the diaphragm gave the equivalent shear stresses corresponding to the respective gage outputs. The gages were checked for electrical leakage after installation in the models. The gage sensitivities determined by the calibration were used to select recording equipment gains during the test.

b. Heat Transfer

The heat transfer gages were calibrated prior to the tests to determine the changes in resistance of the elements with temperature. At the temperatures encountered in these tests, these changes are linear and the resistance at only two temperatures need be determined. This calibration is then used to set the gain of the recording equipment for the expected temperature increase.

c. Pressure

The pressure gages were calibrated (i.e., voltage output versus applied pressure) and checked for air and electrical leakage after installation in the model. The voltage-pressure relation is linear over the range of pressure normally encountered during testing.

These calibrations, in conjunction with estimated values of model pressures provide the basis for adjusting amplifier gains to achieve maximum "readability" of the data recording system.

SECTION IV

TEST CONDITIONS

The test conditions of pressure, temperature and Reynolds number are computed by assuming isentropic expansion of the test gas from the conditions behind the reflected shock in the tube to the test section Mach number which has been previously determined from airflow calibrations. The calculation of test section free-stream parameters includes the effect of molecular vibration assuming a simple harmonic oscillator model for the diatomic constituents of air.

The stagnation enthalpy and temperature of the air behind the reflected shock are determined respectively from

$$H_0 = H_1 \ (H_4/H_1) \tag{1}$$

and

$$T_0 = T_1 \ (T_4/T_1) \tag{2}$$

where H_4/H_1 and T_4/T_1, are functions of U_i, the incident shock velocity (Reference 9-11). U_i is obtained by measuring the time taken by the shock wave to pass between two stations in the shock tube. H_1 is taken from Reference 12 and T_1 is measured prior to each run. Free-stream static temperature is obtained from

$$T_\infty = \frac{H_0}{\bar{C}_{p\infty AV}} \left(1 + \frac{\gamma_\infty - 1}{2} \frac{C_{p\infty}}{\bar{C}_{p\infty AV}} M_\infty^2\right) \tag{3}$$

where γ_∞ is a function of $C_{p\infty}$; $C_{p\infty}$ and $\bar{C}_{p\infty AV}$ include vibrational heat capacity and are functions of T_∞, requiring an iteration between T_∞ and C_p. Free-stream pressure is calculated using

$$P_\infty = \frac{\rho}{\rho_p} P_0 \left(1 + \frac{\gamma - 1}{2} M_\infty^2\right)^{-\frac{\gamma}{\gamma - 1}} \tag{4}$$

where

$$\frac{\rho}{\rho_p} = \frac{(\rho/\rho_0)_{\text{real}}}{(\rho/\rho_0)_{\text{perfect}}}$$

is the real gas correction to the ideal static to total pressure ratio as described in Reference 13 but suitably modified to include vibrational specific heat in the test section, and P_0 is the measured pressure behind the reflected shock. The source data used in this technique are References 12 and 14.

Free-stream velocity, density and dynamic pressure are respectively calculated from

$$U_\infty = M_\infty \sqrt{\gamma_\infty \bar{R} T_\infty} \tag{5}$$

$$\rho_\infty = P_\infty / R T_\infty \tag{6}$$

$$q_\infty = \tfrac{1}{2} \rho_\infty U_\infty^2 \tag{7}$$

Values for absolute viscosity (μ) used to compute Reynolds numbers were obtained from Reference 15 for temperatures below 500°R and from Reference 16 for temperatures above 500°R.

Stagnation conditions behind a normal shock in the test section are based on the data of Reference 14.

SECTION V

DATA REDUCTION

1. SKIN FRICTION

The skin friction gage output is a direct function of the average shear stress over the gage diaphragm and the sensitivity of the gage, which was determined during gage calibration. Dividing gage output by gage sensitivity gives average shear stress directly.

2. HEAT TRANSFER

The "thin-film" heat transfer gage is a resistance thermometer which reacts to the local surface temperature of the model. The theory of heat conduction in a nonhomogeneous body is used to relate the surface temperature to the rate of heat transfer. Since the resistance element has negligible effect on the Pyrex substrate surface temperature, the substrate can be characterized as being semi-infinite, homogeneous and isotropic. The general heat conduction equation is

$$\rho c(T)\frac{\partial T}{\partial \tau} = \frac{\partial}{\partial X}\left[K(T)\frac{\partial T}{\partial X}\right] \tag{8}$$

where ρ, C, and K are substrate density, specific heat and thermal conductivity, respectively, and X is the substrate depth.

If the substrate properties are independent of temperature; i.e., if the temperature change is less than 100°R, a closed-form solution is obtained for the heat transfer rate,

$$\dot{q}(t) = \frac{1}{2}\left(\frac{\pi\rho c k}{t}\right)^{1/2}\left[T(t) + \frac{1}{\pi}\int_0^t \frac{\lambda^{1/2}T(t) - t^{1/2}T(\lambda)}{(t-\lambda)^{3/2}}\,d\lambda\right] \tag{9}$$

For evaluating the integral numerically, the equation is recast in the following form:

$$\dot{q}(n) = \frac{1}{2\sqrt{\pi}\Delta t}\left[(\rho c k)_n^{1/2} T_n\left(\frac{\pi + \sum_{\rho=0}^{\rho=n-1}\frac{\rho^{1/2}}{(n-\rho)^{3/2}}}{n^{1/2}}\right) - \sum_{\rho=0}^{\rho=n-1}\frac{T_\rho(\rho c k)^{1/2}_\rho}{(n-\rho)^{3/2}}\right] \tag{10}$$

where t = time interval between tabulated data points (typically, 50 microseconds)

n = time index of the point

ρ = running time index

subscript n = value of parameters at n^{th} time increment

subscript p = value of parameters at p^{th} time increment

When the gage temperature rise is greater than 100°R the temperature dependence of $(\rho c k)^{1/2}$ and the variation of the electrical properties of the resistance element with temperature are accounted for in the computer program.

Frequently heat transfer data are obtained by solving Equation (9) directly by the use of q-meters, which are passive electrical analog networks, in conjunction with the heat transfer gage. The analog is based on the fact that the equation for heat conduction in a semi-infinite solid is identical to that for a semi-infinite electrical transmission line with distributed series resistance and shunt capacitance. In practice, it has been found feasible to construct the analog of a number of circuit elements consisting of parallel resistor-capacitor elements in a series arrangement. A time and heat transfer rate dependent correction must be applied to the q-meter output to account for gage property variations with temperature.

3. PRESSURE

The pressure transducers measure the difference between the internal case pressure and the model pressure. The case pressure is equal to the initial test section pressure (on the order of 3 microns) and is added to the measured pressure to obtain the absolute pressure.

SECTION VI

DISCUSSION OF RESULTS

The results of this program provide wall skin friction data for turbulent boundary layers in adverse pressure gradients on slender continuous compression bodies typical of the components of hypersonic inlets. In addition one very important characteristic of turbulent boundary layer flows, namely resistance to separation from the wall, can be observed from the wall measurements of skin friction, heat transfer and pressure. The ability of turbulent boundary layers to negotiate rather large adverse pressure gradients without separating is clearly seen by comparing the data herein with the work of Reference 6 which contains wall data obtained for laminar boundary layers in adverse pressure gradients. All the turbulent data obtained in this program were taken using natural boundary layer transition.

The two models were tested at nominal Mach numbers of 7, 8, 10, and 11, and a range of Reynolds numbers at each Mach number. The maximum Reynolds number was limited by the facility and/or instrumentation capabilities and the minimum Reynolds number was limited by the desire to have transition occur before the start of the adverse pressure gradient. This latter restraint was relaxed for many of the two-dimensional tests in order to obtain a larger range in Reynolds number variation. The two-dimensional model was tested at zero degrees angle of attack for Mach numbers of 8, 10 and 11 and at zero, four and eight degrees for a Mach number of 7. These angle of attack runs at Mach 7 were included to obtain data for a lower local Mach number since it was not possible to run the facility at a lower free stream Mach number. The axisymmetric model was tested at zero degrees angle of attack only. In addition to the sharp nose runs on the axisymmetric model, three runs were made with a blunt nose installed in order to obtain a lower local Mach number.

1. TWO-DIMENSIONAL MODEL TEST

The details of the test conditions and run schedule for the two-dimensional model are given in Table I. Data obtained were skin friction, heat transfer rates, pressure and flow photographs. Tabulated skin friction, heat transfer rates and pressure data are given in Tables II, III, and IV, respectively. Skin friction, heat transfer rates and pressure plots are given in Figures 13, 14, and 15, respectively. Flow photographs, either schileren or shadowgraph, for the two-dimensional model test comprise Figure 16. A reference length is indicated in Figure 16(a) to aid in scaling from the photographs. The testing was started using schlieren photography of the flow but a change to shadowgraph was made when it became apparent that the over-sensitive schlieren system showed little boundary layer detail.

Examination of the plotted heat transfer rates and skin friction data shows the approximate location of transition on the model. Although it was desired to have transition completed at the start of the adverse pressure

gradient which was five inches from the leading edge, this generally was not possible since the short distance requires free stream Reynolds numbers beyond the facility capability. However, for the Mach number 7 runs transition was completed within about 10 inches of the model nose and for two of the angle of attack runs transition was completed before the start of the adverse pressure gradient. The higher Mach number testing required a foot or more to achieve a fully turbulent boundary layer. Included on the heat transfer rates plots (Figure 14), are maximum and minimum readings of the transitional heat transfer data. A sample of transitional heat transfer and skin friction data can be seen in Figure 12(c). Note that the heat transfer and skin friction excursions due to turbulent bursts are not as large of a percentage of the average reading for skin friction as they are for heat transfer. This lesser sensitivity to turbulent burst is believed to be a result of an averaging nature of the relatively large area of the skin friction gauge diaphragm. The ratio of the area of the diaphragm to the area of the platinum element on a surface temperature gauge is greater than 10. However, it is still possible to see differences in the skin friction traces as well as the heat transfer for transitional and laminar or turbulent traces as is illustrated in Figure 12.

It should be noted that data from skin friction position 5 have been excluded from this report since these data were always about one half the expected value and examination of the gage after the test indicated some irregularities in its construction. Also the skin friction data from the first four positions on Runs 4 and 5 (see Figure 13(b)) were of poor quality and therefore no significance should be given to the distributions indicated for these points. It is clear that the values of skin friction were small indicating laminar or transitional flow which is in agreement with the heat transfer measurements shown in Figure 14(b).

The heat transfer and skin friction data distributions along the model exhibit considerable waviness even in the turbulent boundary layer region. This waviness is believed to be real and not a fault of the instrumentation since two rather different types of instrumentation operating on fundamentally different principles both show waviness and pre- and post-test calibrations of the skin friction gages showed excellent linearity and repeatability. Admittedly, the argument would be stronger if the waviness shown by the two types of instrumentation was always in phase but there may be reasons for a phase shift. The waviness may result from the fact that for most runs transition is occurring in an adverse pressure gradient or from nonisentropic compression. Careful examination of the flow photographs of Figure 16 reveals what appear to be weak shock waves emanating from the surface in some cases. The fact that the pressure distributions generally appear smooth is not necessarily a contradiction in that it has been observed in the past that sensitivity to flow irregularities is greatest for skin friction gages, somewhat less for heat transfer and least for pressure. A good example of these relative sensitivities will be shown later in the discussion of the blunt nose data from the axisymmetric models.

Edge effects, which could affect the levels of the data distributions on the model do not appear to be significant judging from the pressure data. Comparison of the overall pressure rise from the data with the predicted inviscid pressure rise shows good agreement of the lower Mach number, higher Reynolds number conditions; a decrease in the experimental pressure rise compared to the inviscid pressure rise is observed at the higher Mach number, lower Reynolds number conditions. This behavior is qualitatively correct for viscous effects since at the lower Mach number, higher Reynolds number conditions the boundary layer is thinner and the pressure distribution should be closer to the inviscid predictions. Conversely, edge effects should be more important at the lower Mach numbers and would tend to make agreement with the inviscid values poorer. Base effects at the rear of the model appear to affect only the last pressure measurement on some runs as can be seen in Figure15(c) and (d).

The apparent double shock visible in the flow photographs of Figure 16 is believed to be caused by very small amounts of leading edge waviness which produces a shock sheet of increasing thickness in the downstream direction. The optical system photographs the cross-section projection of this shock sheet. The work of References 2 and 6 using similar models indicates the same shock behavior. Work performed at CAL and reported in Reference 2 shows several flow photographs of a sharp leading edge model with the leading edge in the field of view and the origination of the apparent double shock at the leading edge is visible.

2. AXISYMMETRIC MODEL TEST

The details of the test conditions and run schedule for the axisymmetric model are given in Table V. Data obtained were skin friction, heat transfer rates, pressure and flow photographs. Tabulated skin friction, heat transfer and pressure data are given in Tables VI, VII, and VIII, respectively. Skin friction, heat transfer and pressure plots are given in Figures 17, 18, and 19, respectively. Flow photographs, either schlieren or shadowgraph, for the axisymmetric model test comprise Figure 20. A reference length, the distance normal to the side of the pitot probe to the model surface, measured in the plane of the forward face of the probe, is included in Figure 20(a) to aid in scaling from the photographs. The testing was started using shadowgraph based on what was learned from the two-dimensional model testing and changed to schlieren when it was observed that more system sensitivity was needed.

As a result of having about 23 inches of model length upstream of the start of the adverse pressure gradient region for the sharp nose configuration, transition was completed before the start of the gradient on all but two sharp nose model test runs at a nominal Mach number of 10. Natural transition was desired since data obtained from tripped boundary layers can be affected by the tripping process as is evident in Reference 17 and as will be shown a little later in this discussion. On the blunt nose configuration the effect of bluntness delayed transition into the gradient region for the two lower Reynolds

number runs. For the sharp nose model all the data distributions appear reasonably smooth and rise to very high values at the rear of the model. With the exception of the Mach number 11 runs, the pressure data agrees quite well with the inviscid estimates as can be seen in Figure 19. At the Mach number 11 condition the boundary layer apparently had more influence in reducing the amount of compression of the flow over the model. It should be noted that due to the very rapid rise in the data at the rear of the model, waviness in the distributions like that observed on the two-dimensional model would be difficult to observe and hence it cannot necessarily be concluded that the waviness isn't present. The only evidence of possible base effects appears to be in the Mach number 11 data where the last pressure position appears to be reading low compared to the experimental distribution suggested by the pressures upstream of it. For the lower Mach number data the most rearward pressures seem to be slightly above the inviscid estimates, suggesting that a local shock may be present near the rear of the model. The flow photographs of Figure 20 do show a rather abrupt compression near the rear of the model but it is difficult to conclude that a secondary shock is present.

In an attempt to see if the large increase in all the data levels toward the rear of the model was reasonable, a comparison of heat transfer data from the present tests with data from Reference 5 was made for a Mach number 8 test condition that was common to both sets of data. The results of this comparison can be seen in Figure 18(c). The data of Reference 5 were obtained with tripping devices on the forward portion of the model. As can be seen the tripped boundary layer data, which are shown for wall to total temperature ratios of 0.36 and 0.44 as noted, fall considerably below the natural transition results of the present tests which were conducted at a wall temperature ratio of 0.34. The upstream data points from the tripped test fell below the range of the plot but are included with appropriate notations. Included on the plot is a flat plate theory* line from the method of Reference 18. Other predicted heating rates from the work of Van Driest and Von Karman were also examined and were found to range up to a value of about 3.4 Btu/ft^2-sec for the two foot station on the forward cylindrical section of the model. It is clear that the present data obtained with natural boundary layer transition is in better agreement with theory than the data resulting from boundary layer tripping. The qualitative relationship of the natural transition data to the tripped boundary layer data is in agreement with the results of Reference 17 which indicates that for a given distance aft of the natural transition point on a model, tripped boundary layers give lower heating rates than boundary layers which have experienced natural transition. Interestingly enough the tripped boundary layer heat transfer data indicate a ratio of increase from the front to the rear of the model which is greater than the corresponding ratio for the natural transition data but the maximum level reached is less. Consequently, the large rise in heat transfer rate from the front to the rear of the model observed in the present test does not appear unusual and from the relationship between heat transfer and skin friction a large increase in skin friction from the front to the rear of the model is also reasonable.

*Comparing flat plate estimates with data from axisymmetric bodies is valid when the boundary layer thickness is small compared to the body radius as is certainly the case for these high Reynolds number test conditions and large model size.

The last three runs of the axisymmetric model test were conducted with a blunt nose installed on the model to reduce the local flow Mach number. Unfortunately this blunt configuration produced a bow shock which intersected the nozzle wall and reflected back over the rear of the model nearly hitting the rear corner as can be seen in Figures 20(m), 20(n), and 20(o). Since the model length and the length of the test rhombus were nearly the same, it was not possible to withdraw the model from the nozzle without affecting the flow over the rear of the model and furthermore hardware did not exist to allow this change in model position. Theoretically, since the reflected shock missed the rear of the model, the flow over the model should be unaffected. Examination of the pressure distributions (Figure 19(e)) and comparison with the inviscid estimates seems to bear this out and the heat transfer data (Figure 19(e)) exhibit a smooth distribution from front to rear. However, the skin friction data distributions are very erratic in the adverse pressure gradient region as can be seen by examining Figure 17(e). In this Figure all the skin friction data traces for the blunt nose runs are presented to demonstrate the erratic nature of these data. An average reading from a step output, typical of the other data presented in this report, would have little meaning for most of these traces.

These blunt nose runs were made at the same free stream conditions as Runs 28 and 29 which did not produce erratic data. The two primary differences between the two groups of runs were first, nose geometry and second, the bow shock reflection from the nozzle. Both the nose geometry and the bow shock intersection with the nozzle could combine to give a system of compression and expansion waves. The waves from the expansion around the blunt nose reflecting from the bow shock and/or shocks from the nozzle boundary layer separation ahead of the model bow shock intersection point may very well interact to produce the observed skin friction gage behavior. The lack of visible evidence of the hypothetical wave systems in the flow photographs and the apparent smoothness in the pressure and heat transfer distributions may not be contradictory but may be only the result of relative sensitivities of the instrumentation. It is very possible that a secondary weak wave system may not show in the flow photographs because of the basic sensitivity of the schlieren system or the predominance of the basic flow structure. It is also known to be true from previous work (Reference 6), that skin friction gages are much more sensitive to flow disturbances than heat transfer or pressure. Careful examination of the heat transfer raw data does show more unsteadiness than usual but not enough, it is felt, to invalidate the time averaged reading presented herein.

Admittedly, this explanation of the erratic skin friction data is very hypothetical but the alternative of condemning the skin friction gage performance does not seem to be justified since pre- and post-test calibrations agreed within ±3% in magnitude and ±2% in linearity. The absolute skin friction and pressures levels to which the skin friction gages were subjected were actually considerably less on the blunt nose runs than on the sharp nose runs 28 and 29 conducted at the same free stream conditions, hence the blunt nose testing did not represent an extreme test environment. The pressure data in fact indicate that the gross model flow field was about as predicted as can be seen in Figure 19(e).

SECTION VII

PRECISION OF DATA

Test Conditions

The data reduction program computes free-stream static pressure from the following equation:

$$P = (P/P_p)(1 + .2M^2)^{-3.5} P_0 \qquad (11)$$

where (P/P_p) is the real gas correction for static to total pressure ratio and is subject to negligible error in an individual program. Based on the agreement of pressure transducers, the reservoir pressure measurements are considered accurate to ±3%.

The effect of Mach number on free-stream pressure may be determined as follows: Each nozzle-throat combination employed is calibrated prior to its use on a program by measuring the ratio of pitot to reservoir pressure. The computed values of free-stream Mach number from a large number of runs normalized to a given condition are used to calculate a standard deviation in nominal Mach number at that condition and these deviations are as follows:

Nominal Mach Number	Standard Deviation (σ)
11.2	.1255
9.9	.0911
8.0	.0765
6.8	.0709

If there is a normal error distribution in the calibration, then the mean Mach number value may be taken to be the actual value of M_∞. The validity of assuming a normal error distribution may be seen by an analysis of pitot and reservoir pressure errors as they affect M_∞. The ratio of pitot to reservoir pressure can be expressed as:

$$P_0'/P_0 = \left(\frac{6M_\infty^2}{M_\infty^2 + 5}\right)^{7/2} \left(\frac{6}{7M_\infty^2 - 1}\right)^{5/2} \qquad (12)$$

but since the Mach numbers of interest are hypersonic, a reasonable assumption is:

$$M_\infty^2 + 5 \approx M_\infty^2, \text{ and } 7M_\infty^2 - 1 \approx 7M_\infty^2 \qquad (13)$$

therefore

$$P_o'/P_o = C/M_\infty^5 \tag{14}$$

Applying the "most probable error" analysis (Reference 19) to equation (14) yields:

$$\frac{dM_\infty}{M_\infty} = \sqrt{1/25\left(\frac{dP_o}{P_o}\right)^2 + 1/25\left(\frac{dP_o'}{P_o'}\right)^2} \tag{15}$$

Again based on the agreement of pressure transducers, pitot pressure measurements are considered accurate to ±5%. Using accuracy figures of ±3% and ±5% for reservoir and pitot pressure, respectively, in the above equation it can be shown that the "most probable error" for M_∞ is ±1.2%. Since $\sigma/M \leq 1.2\%$ then, σ can be seen to be within the accuracy of reservoir and pitot pressures.

The precision within within which P_∞ is known is affected by both the accuracy within which P_o is measured and the accuracy within which is known.

Now by applying the "most probable error" analysis to equation (1), it can be shown that:

$$\frac{dP_\infty}{P_\infty} = \sqrt{\left[\frac{1.4M_\infty^2}{1+2M_\infty^2}\right]^2\left(\frac{dM_\infty}{M_\infty}\right)^2 + \left(\frac{dP_o}{P_o}\right)^2} \tag{16}$$

Employing accuracies of ±3% and ±1.2% for reservoir pressure and Mach number, respectively, it can be shown that the "most probable errors" in P_∞ to be expected during this test program are:

M_∞	MPE_{P_∞}
11.2	±8.7%
9.9	±8.5%
8.0	±8.3%
6.8	±8.2%

Model Attitude

The model attitude was set with an inclinometer at the desired angle of attack which is estimated to be within ±0.1°.

Skin Friction

The errors involved in calibrating the skin friction gages are the following:

Calibrating weight errors	±0.4%
Metric diaphragm diameter	±0.22%
Reduction of calibration data	±2%

Taking the square root of the sum of the squares of these errors gives an overall error for the calibrations of ±2.4%. The skin friction gage pre- and post-test calibrations actually agreed to within ±3% for all models. Linearity of all skin friction gages is within ±2% as determined from the calibrations.

To assess the accuracy of the test data it is necessary to consider calibration accuracy, the Navcor recording equipment resolution, and trace reading accuracy. The calibrations are known to within ±3%. Navcor resolution is ±0.05 volts which produces an error of ±1% assuming a five volt data output. Maximum error in the data reduction trace reading is ±2%. Combining these gives a "most probable error" of ±3.8%.

Two other potentially important sources of error in skin friction measurement are acceleration and pressure sensitivity of the gages. The acceleration sensitivity of the gages utilized in this investigation is so low that model acceleration does not affect the accuracy of the skin friction data. The data have a maximum error due to pressure sensitivity of ±7% pressure sensitivity error is computed for those gages, gage locations and test conditions giving the maximum error. The majority of the skin friction data have a smaller pressure sensitivity error because the test conditions and gage locations were such as to give a larger ratio of measured skin friction to measure pressure. The resulting overall accuracy for most of the skin friction data then becomes about ±6%.

Heat Transfer

Calibrations to determine the heat gages' temperature-resistance characteristics are conducted with an error potential of 1 percent. Far more significant than this is the repeatability of the heat gage during test. A series of shock tunnel tests designed to determine repeatability of the heat transfer data has shown that the RMS deviation of the repeatability is ±3 percent. Combining these errors indicates that the relative RMS deviation of the heat transfer data is about ±3.2 percent.

Pressure

The pressure transducers are accurate to ±1% of their maximum calibration pressure. On the basis of consistency and repeatability of the pressure data, it is estimated that these data are accurate to within ±5%.

SECTION VIII

CONCLUSIONS

Hypersonic shock tunnel tests were conducted on a two-dimensional and an axisymmetric compression body typical of hypersonic inlet compression surfaces to obtain wall skin friction data for a turbulent boundary layer in an adverse pressure gradient. Both models were instrumented in the continuous compression regions with skin friction, heat transfer and pressure gages. Each model was tested at a nominal Mach number of 11, 10, 8 and 7 with a Reynolds number variation at each Mach number. Testing was conducted at large Reynolds numbers to obtain natural boundary layer transition on the models. Wall measurements were concentrated in the adverse pressure gradient regions and included laminar, transitional and turbulent data, depending upon the location of transition relative to the instrumentation. Flow photographs, either schlieren or shadowgraph, were obtained for most runs of the program.

As a result of the experimental hypersonic turbulent boundary layer investigation reported herein the following conclusions are reached.

1. Turbulent boundary layers can negotiate much larger adverse pressure gradients without separating compared to laminar boundary layers. The validity of this conclusion is easily seen by comparing the data herein with the data from Reference 6 which contains separated laminar boundary layer data taken in an adverse pressure gradient. Comparison of the two-dimensional model data indicates that the maximum adverse pressure gradient for the turbulent tests was about two times the gradient for the laminar tests and comparison of the axisymmetric model data from the present tests with the axisymmetric data of Reference 6 indicate a ratio of about ten to one for the adverse pressure gradient. No indications of separation were observed in the data presented herein.

2. Nose bluntness delays transition as can be seen by comparing the data from the blunt nose axisymmetric model with the sharp nose results at the same freestream conditions.

3. The boundary layer does not appreciably change the model pressure from the inviscid distribution if the boundary layer thickness is small compared to the model thickness.

4. Skin friction gages appear to be sensitive to flow non-uniformities that are undetected by heat transfer or pressure instrumentation.

5. At a given position downstream of the natural transition point on a model, heat transfer and skin friction data from a tripped boundary layer will be less than the corresponding data resulting from natural transition.

SECTION IX

REFERENCES

1. Hertzberg, A., Wittliff, C.E., and Wilson, M.R., "The Tailored-Interface Hypersonic Shock Tunnel," Journal of the Aerospace Sciences, Vol. 26, No. 4, April 1959, pp. 219-228.

2. Kutschenreuter, Paul H., Jr., et al, "Investigation of Hypersonic Inlet Shock-Wave Boundary Layer Interaction," AFFDL-TR-65-36, March 1965.

3. Harshman, D.L., et al, "Analytical and Experimental Evaluation of Inlet Compression Systems in the Mach Range 10 to 25," Technical Documentary Report No. ASD-TRD-63-629.

4. Cohen, C.B., and Reshotko, E., "The Compressible Laminar Boundary Layer with Heat Transfer and Arbitrary Pressure Gradient," NACA Report 1294, 1956.

5. Stroud, J.F. and Miller, L.D., "An Experimental and Analytical Investigation of Hypersonic Inlet Boundary Layers," AFFDL-TR-65-123, Vol. I and II, August 1965.

6. Ryder, M.O., "Skin Friction, Heat Transfer and Pressure Measurements on Hypersonic Inlet Compression Surface in the Mach Number Range 7.5 to 16," AFFDL-TR-65-199, December 1965.

7. Vidal, R.J., "Transient Surface Temperature Measurements," Cornell Aeronautical Laboratory, Inc., Report No. 114, March 1962.

8. Martin, J.F., Duryea, G.R., and Stevenson, L.M., "Instrumentation for Force and Pressure Measurements in a Hypersonic Shock Tunnel," CAL Report No. 113, January 1962.

9. Reece, J.W., "Shock Tube Theory for Real Air with Applications to Wind Tunnel Testing and to Flight Simulation," CAL Experimental Facilities Division, WTH-003, October 1958 (Revised August 1959).

10. Wittliff, C., Unpublished Normal Shock Calculations Using Duff's Computing Procedure, Aerodynamics Research Department, CAL about 1963.

11. Lewis, Clark H. and Burgess, E.G., "Charts of Normal Shock Wave Properties in Imperfect Air," AEDC-TDR-64-43, March 1964.

REFERENCES (Concluded)

12. Hilsenrath, J., Beckett, C.W., et al, "Tables of Thermal Properties of Gases," National Bureau of Standards Circular 564, November 1955.

13. Reece, J.W., "Test Section Conditions Generated in the Supersonic Expansion of Real Air," Reader's Forum, Journal of Aerospace Sciences, Vol. 29, No. 5, May 1962, pp. 617-618.

14. Neel, C.A. and Lewis, Clark H., "Interpolations of Imperfect Air Thermodynamic Data, II, at Constant Pressure," AEDC-TDR-64-184, September 1964.

15. Hirschfelder, J.O., Curtis, C.F., and Bird, R.G., Molecular Theory of Gases and Liquids, J. Wiley and Sons, 1954.

16. Hansen, C.F., "Approximations for Thermodynamic and Transport Properties of High-Temperature Air," NACA TN-4150, March 1958 (Revised NASA TR-50, 1959).

17. Holloway, Paul F. and Sterrett, James R., "Effect of Controlled Surface Roughness on Boundary Layer Transition and Heat Transfer at Mach Numbers of 4.8 and 6.0," NASA TN D-2054, April 1964.

18. Eckert, E.R.G., "Engineering Relations for Friction and Heat Transfer to Surfaces in High Velocity Flow," Journal of the Aeronautical Sciences, pp. 585-587, August 1965.

19. Topping, J., "Errors of Observation and their Treatment," Unwin Brothers Ltd., Wokin and Londen, 1955.

Table I

RUN SCHEDULE AND TEST CONDITIONS FOR THE TWO-DIMENSIONAL MODEL TESTS

RUN NO.	1	2	3	4	5	6	7	8
α	0.0	0.0	0.0	0.0	0.0	0.0	0.0	0.0
ψ	0.0	0.0	0.0	0.0	0.0	0.0	0.0	0.0
ϕ	0.0	0.0	0.0	0.0	0.0	0.0	0.0	0.0
M_1	3.110E 00	3.227E 00	3.383E 00	4.046E 00	4.021E 00	2.631E 00	2.583E 00	2.557E 00
P_o	9.770E 03	1.526E 04	2.152E 04	1.343E 04	1.822E 04	2.643E 03	2.512E 03	4.827E 03
H_o	1.634E 07	1.685E 07	1.850E 07	3.616E 07	3.616E 07	1.193E 07	1.166E 07	1.149E 07
T_o	2.561E 03	2.654E 03	2.866E 03	5.026E 03	5.033E 03	1.889E 03	1.845E 03	1.828E 03
M_∞	1.104E 01	1.118E 01	1.127E 01	9.454E 00	9.544E 00	7.883E 00	7.883E 00	7.882E 00
U_∞	5.609E 03	5.695E 03	5.876E 03	8.265E 03	8.269E 03	4.712E 03	4.649E 03	4.619E 03
T_∞	1.073E 02	1.088E 02	1.167E 02	3.178E 02	3.122E 02	1.489E 02	1.443E 02	1.389E 02
P_∞	1.201E-01	1.948E-01	2.561E-01	3.138E-01	4.156E-01	3.057E-01	2.913E-01	5.405E-01
q_∞	1.102E 01	1.705E 01	2.278E 01	1.065E 01	2.653E 01	1.334E 01	1.272E 01	2.419E 01
ρ_∞	1.009E-04	1.514E-04	1.941E-04	8.296E-05	1.117E-04	1.731E-04	1.695E-04	3.266E-04
μ_∞	9.028E-08	9.081E-08	9.815E-08	2.537E-07	2.439E-07	1.243E-07	1.210E-07	1.166E-07
Re/FT	6.268E 06	9.497E 06	1.129E 07	2.609E 06	3.633E 06	6.561E 06	6.509E 06	1.294E 07
P'_o	2.030E 01	3.157E 01	4.223E 01	3.602E 01	4.933E 01	2.459E 01	2.343E 01	4.456E 01
T'^o	9.344E 02	9.479E 02	9.950E 02	1.530E 03	1.530E 03	7.012E 02	6.990E 02	6.978E 02
μ'	5.297E-07	5.356E-07	5.604E-07	7.838E-07	7.837E-07	4.684E-07	4.630E-07	4.595E-07
$\sqrt{C'}$	9.697E-01	9.665E-01	9.577E-01	8.030E-01	8.021E-01	8.926E-01	8.944E-01	8.954E-01
H_w	3.234E 06	3.201E 06	3.210E 06	3.195E 06	3.213E 06	3.195E 06	3.198E 06	3.201E 06
T_w	5.385E 02	5.333E 02	5.360E 02	5.330E 02	5.359E 02	5.329E 02	5.325E 02	5.330E 02
P_{ts}	9.670E-05	5.802E-05	9.670E-05	5.802E-05	5.802E-05	1.934E-04	2.901E-04	1.934E-05

Table I (CONTINUED)

RUN NO.	9	10	11	12	13	14	15	16
α	0.0	0.0	0.0	0.0	0.0	8.000E 00	8.000E 00	8.000E 00
ψ	0.0	0.0	0.0	0.0	0.0	0.0	0.0	0.0
ϕ	0.0	0.0	0.0	0.0	0.0	0.0	0.0	0.0
M_i	2.459E 00	4.834E 00	4.918E 00	4.883E 00	4.947E 00	4.859E 00	4.921E 00	4.937E 00
P_o	9.112E 03	3.937E 03	9.332E 03	8.267E 03	1.291E 04	3.873E 03	8.346E 03	1.267E 04
H_o	1.074E 07	3.453E 07	3.566E 07	3.558E 07	3.666E 07	3.521E 07	3.608E 07	3.633E 07
T_o	1.767E 03	4.824E 03	4.963E 03	4.958E 03	5.090E 03	4.909E 03	5.017E 03	5.049E 03
M_∞	8.127E 00	6.805E 00	6.868E 00	6.870E 00	6.955E 00	6.709E 00	6.868E 00	6.956E 00
U_∞	4.471E 03	7.894E 03	8.039E 03	8.021E 03	8.151E 03	7.971E 03	8.076E 03	8.114E 03
T_∞	1.258E 02	5.602E 02	5.698E 02	5.661E 02	5.718E 02	5.725E 02	5.753E 02	5.666E 02
P_∞	1.040E 00	7.312E-01	1.532E 00	1.507E 00	2.199E 00	7.327E-01	1.521E 00	2.178E 00
q_∞	4.815E 01	2.370E 01	5.059E 01	4.992E 01	7.410E 01	2.370E 01	5.021E 01	7.374E 01
ρ_∞	6.937E-04	1.005E-04	2.260E-04	2.234E-04	3.212E-04	1.074E-04	2.217E-04	3.226E-04
μ_∞	1.058E-07	3.967E-07	4.014E-07	3.998E-07	4.029E-07	4.032E-07	4.050E-07	4.001E-07
Re/FT	2.932E 07	2.180E 06	4.520E 06	4.483E 06	6.499E 06	2.173E 06	4.421E 06	6.542E 06
P'_o	8.961E 01	4.408E 01	9.606E 01	9.479E 01	1.408E 02	4.499E 01	9.539E 01	1.401E 02
T'	5.550E 02	1.539E 03	1.576E 03	1.574E 03	1.609E 03	1.564E 03	1.591E 03	1.597E 03
$\frac{M'}{\sqrt{C'}}$	4.458E-07	7.886E-07	8.002E-07	7.996E-07	8.104E-07	7.966E-07	8.051E-07	8.067E-07
	8.999E-01	8.509E-01	8.485E-01	8.482E-01	8.456E-01	8.503E-01	8.481E-01	8.459E-01
H_w	3.207E 06	3.183E 06	3.180E 06	3.207E 06	3.219E 06	3.201E 06	3.207E 06	3.210E 06
T_w	5.340E 02	5.300E 02	5.310E 02	5.340E 02	5.360E 02	5.333E 02	5.340E 02	5.345E 02
P_{ts}	3.969E-05	1.934E-05	1.934E-05	1.934E-05	1.934E-05	1.934E-05	1.934E-05	1.934E-05

Table I (CONCLUDED)

RUN NO.	17
α	4.0000E 00
ψ	0.0
ϕ	0.0
M_i	4.0111E 00
P_o	8.2535E 03
H_o	3.4232E 07
T_o	5.0365E 03
M_∞	6.8685E 00
U_∞	8.0025E 03
T_∞	5.7705E 02
P_∞	1.4305E 00
q_∞	4.0445E 01
ρ_∞	2.1756E-04
μ_∞	4.0415E-07
Re/FT	4.2325E 06
P'_o	8.3035E 01
T^*	1.5075E 03
μ^*	8.0695E-07
$\sqrt{C^*}$	8.4705E-01
H_w	3.2105E 06
T_w	5.3605E 02
P_{ts}	1.0345E-05

Table II

TWO-DIMENSIONAL MODEL SKIN FRICTION DATA

RUN	GAGE	M_∞	τ
1	1	1.104E 01	3.372E-03
1	2	1.104E 01	4.958E-03
1	3	1.104E 01	5.772E-03
1	4	1.104E 01	1.175E-02
1	5	1.104E 01	3.726E-03
1	7	1.104E 01	4.501E-03
1	8	1.104E 01	4.741E-03
1	9	1.104E 01	4.538E-03
1	10	1.104E 01	5.765E-03
1	11	1.104E 01	6.481E-03
1	12	1.104E 01	7.140E-03
1	13	1.104E 01	7.381E-03
1	14	1.104E 01	1.034E-01
1	15	1.104E 01	1.056E-01
2	1	1.118E 01	5.307E-03
2	2	1.118E 01	7.027E-03
2	3	1.118E 01	1.150E-02
2	4	1.118E 01	2.300E-02
2	5	1.118E 01	4.658E-03
2	7	1.118E 01	5.686E-03
2	8	1.118E 01	6.404E-03
2	9	1.118E 01	6.630E-03
2	10	1.118E 01	8.066E-03
2	11	1.118E 01	9.562E-03
2	12	1.118E 01	9.263E-03
2	13	1.118E 01	1.143E-01
2	14	1.118E 01	1.461E-01
2	15	1.118E 01	1.396E-01
3	1	1.127E 01	5.692E-03
3	2	1.127E 01	8.620E-03
3	3	1.127E 01	2.026E-02
3	4	1.127E 01	3.369E-02
3	5	1.127E 01	6.332E-03
3	7	1.127E 01	7.431E-03
3	8	1.127E 01	8.461E-03
3	9	1.127E 01	8.824E-03
3	10	1.127E 01	1.139E-01
3	11	1.127E 01	1.331E-01
3	12	1.127E 01	1.178E-01
3	13	1.127E 01	1.515E-01
3	14	1.127E 01	2.055E-01
3	15	1.127E 01	1.913E-01

Table II (CONTINUED)

RUN	GAGE	M_∞	τ
4	1	9.454E 00	3.773E-03
4	2	9.454E 00	3.393E-03
4	3	9.454E 00	3.305E-03
4	4	9.454E 00	5.554E-03
4	5	9.454E 00	4.005E-03
4	7	9.454E 00	3.986E-03
4	8	9.454E 00	1.113E-01
4	9	9.454E 00	1.034E-01
4	10	9.454E 00	1.115E-01
4	11	9.454E 00	1.313E-01
4	12	9.454E 00	1.134E-01
4	13	9.454E 00	1.444E-01
4	14	9.454E 00	1.342E-01
4	15	9.454E 00	1.417E-01
5	1	9.544E 00	8.364E-03
5	2	9.544E 00	1.196E-02
5	3	9.544E 00	4.100E-03
5	4	9.544E 00	7.439E-03
5	6	9.544E 00	9.609E-03
5	7	9.544E 00	1.215E-01
5	8	9.544E 00	1.409E-01
5	9	9.544E 00	1.104E-01
5	10	9.544E 00	1.536E-01
5	11	9.544E 00	1.356E-01
5	12	9.544E 00	1.477E-01
5	13	9.544E 00	2.020E-01
5	14	9.544E 00	2.444E-01
5	15	9.544E 00	2.340E-01
6	3	7.893E 00	3.115E-03
6	4	7.893E 00	2.903E-03
6	6	7.893E 00	3.776E-03
6	7	7.893E 00	4.941E-03
6	8	7.893E 00	4.440E-03
6	9	7.893E 00	4.568E-03
6	10	7.893E 00	5.350E-03
6	11	7.893E 00	4.304E-03
6	12	7.893E 00	5.963E-03
6	13	7.893E 00	4.145E-03
6	14	7.893E 00	8.921E-03
6	15	7.893E 00	6.573E-03

Table II (CONTINUED)

RUN	GAGE	M_∞	τ
7	1	7.893E 00	1.242E-02
7	2	7.893E 00	3.288E-02
7	3	7.893E 00	3.749E-02
7	4	7.893E 00	3.749E-02
7	5	7.893E 00	3.776E-02
7	7	7.893E 00	4.174E-02
7	8	7.893E 00	4.449E-02
7	9	7.893E 00	4.526E-02
7	10	7.893E 00	5.329E-02
7	11	7.893E 00	5.222E-02
7	12	7.893E 00	5.059E-02
7	13	7.893E 00	5.082E-02
7	14	7.893E 00	8.309E-02
7	15	7.893E 00	8.449E-02
8	1	7.892E 00	3.469E-02
8	2	7.892E 00	4.915E-02
8	3	7.892E 00	4.775E-02
8	4	7.892E 00	4.434E-02
8	5	7.892E 00	4.432E-02
8	7	7.892E 00	4.791E-02
8	8	7.892E 00	7.587E-02
8	9	7.892E 00	7.550E-02
8	10	7.892E 00	8.281E-02
8	11	7.892E 00	1.088E-01
8	12	7.892E 00	1.072E-01
8	13	7.892E 00	1.103E-01
8	14	7.892E 00	1.543E-01
8	15	7.892E 00	1.516E-01
9	1	8.127E 00	5.479E-02
9	2	8.127E 00	7.722E-02
9	3	8.127E 00	8.110E-02
9	4	8.127E 00	7.438E-02
9	6	8.127E 00	1.146E-01
9	7	8.127E 00	1.231E-01
9	8	8.127E 00	1.371E-01
9	9	8.127E 00	1.366E-01
9	10	8.127E 00	1.479E-01
9	11	8.127E 00	1.939E-01
9	12	8.127E 00	1.810E-01
9	13	8.127E 00	2.165E-01
9	14	8.127E 00	2.452E-01
9	15	8.127E 00	2.754E-01

Table II (CONTINUED)

RUN	GAGE	M_∞	τ
10	2	6.805E 00	1.453E-02
10	3	6.805E 00	2.379E-02
10	4	6.805E 00	3.352E-02
10	5	6.805E 00	8.029E-02
10	7	6.805E 00	8.515E-02
10	8	6.805E 00	1.032E-01
10	9	6.805E 00	2.857E-02
10	10	6.805E 00	1.144E-01
10	11	6.805E 00	1.368E-01
10	12	6.805E 00	1.136E-01
10	13	6.805E 00	1.444E-01
10	14	6.805E 00	1.351E-01
10	15	6.805E 00	1.540E-01
11	1	6.848E 00	2.550E-02
11	6	6.848E 00	1.533E-01
11	7	6.848E 00	1.498E-01
11	8	6.848E 00	1.800E-01
11	12	6.848E 00	2.280E-01
12	1	6.870E 00	2.405E-02
12	2	6.870E 00	1.169E-01
12	3	6.870E 00	1.314E-01
12	4	6.870E 00	1.140E-01
12	5	6.870E 00	1.582E-01
12	7	6.870E 00	1.494E-01
12	9	6.870E 00	1.838E-01
12	9	6.870E 00	1.908E-01
12	10	6.870E 00	2.283E-01
12	11	6.870E 00	2.401E-01
12	12	6.870E 00	2.311E-01
12	15	6.870E 00	3.101E-01
13	1	6.955E 00	1.700E-01
13	3	6.955E 00	1.830E-01
13	4	6.955E 00	1.629E-01
13	5	6.955E 00	2.266E-01
13	8	6.955E 00	2.681E-01
13	9	6.955E 00	2.753E-01
13	10	6.955E 00	3.242E-01
13	11	6.955E 00	3.961E-01
13	12	6.955E 00	3.328E-01
13	13	6.955E 00	4.212E-01
13	14	6.955E 00	5.214E-01
13	15	6.955E 00	4.405E-01

Table II (CONTINUED)

RUN	GAGE	M_∞	τ
14	1	6.798E 00	1.938E-01
14	2	6.798E 00	1.475E-01
14	3	6.798E 00	1.838E-01
14	4	6.798E 00	2.170E-01
14	7	6.798E 00	2.112E-01
14	8	6.798E 00	2.238E-01
14	9	6.798E 00	2.019E-01
14	10	6.798E 00	2.344E-01
14	11	6.798E 00	2.401E-01
14	12	6.798E 00	2.260E-01
14	13	6.798E 00	2.680E-01
14	14	6.798E 00	2.887E-01
14	15	6.798E 00	2.821E-01
15	1	6.868E 00	1.727E-01
15	2	6.868E 00	2.524E-01
15	3	6.868E 00	2.781E-01
15	4	6.868E 00	2.674E-01
15	6	6.868E 00	3.650E-01
15	7	6.868E 00	3.725E-01
15	8	6.868E 00	3.977E-01
15	9	6.868E 00	3.802E-01
15	10	6.868E 00	4.327E-01
15	11	6.868E 00	4.459E-01
15	12	6.868E 00	4.194E-01
15	13	6.868E 00	4.882E-01
15	14	6.868E 00	5.440E-01
15	15	6.868E 00	5.850E-01
16	1	6.956E 00	2.743E-01
16	2	6.956E 00	3.500E-01
16	3	6.956E 00	3.746E-01
16	4	6.956E 00	3.517E-01
16	6	6.956E 00	5.143E-01
16	7	6.956E 00	5.413E-01
16	8	6.956E 00	5.983E-01
16	9	6.956E 00	5.494E-01
16	11	6.956E 00	6.240E-01
16	12	6.956E 00	5.978E-01
16	13	6.956E 00	7.702E-01
16	14	6.956E 00	7.971E-01
16	15	6.956E 00	8.213E-01

Table II (CONCLUDED)

RUN	GAGE	M_∞	τ
17	1	6.86[illegible]E 00	1.583E-01
17	2	6.86[illegible]E 00	1.913E-01
17	3	6.86[illegible]E 00	2.058E-01
17	4	6.86[illegible]E 00	1.990E-01
17	5	6.86[illegible]E 00	2.712E-01
17	7	6.86[illegible]E 00	2.740E-01
17	9	6.86[illegible]E 00	2.926E-01
17	9	6.86[illegible]E 00	2.947E-01
17	10	6.86[illegible]E 00	3.573E-01
17	11	6.86[illegible]E 00	3.606E-01
17	12	6.86[illegible]E 00	3.415E-01
17	13	6.86[illegible]E 00	4.110E-01
17	14	6.86[illegible]E 00	4.590E-01
17	15	6.86[illegible]E 00	4.710E-01

Table III

TWO-DIMENSIONAL MODEL HEAT TRANSFER DATA

RUN	GAGE	$\dot{q}_{av}$
1	1	2.178E 00
1	2	2.766E 00
1	3	1.268E 01
1	4	1.930E 01
1	5	2.510E 01
1	6	3.561E 01
1	7	3.420E 01
1	8	3.883E 01
1	9	3.930E 01
1	10	5.454E 01
2	1	2.646E 00
2	2	3.570E 00
2	3	1.884E 01
2	4	2.043E 01
2	5	3.051E 01
2	6	5.642E 01
2	7	5.341E 01
2	8	6.118E 01
2	9	6.883E 01
2	10	8.815E 01
3	1	3.402E 00
3	2	4.861E 00
3	3	2.589E 01
3	4	4.022E 01
3	5	5.538E 01
3	6	8.786E 01
3	7	8.217E 01
3	8	8.759E 01
3	9	8.578E 01
3	10	1.230E 02
4	1	1.121E 01
4	2	1.252E 01
4	3	3.422E 01
4	4	8.302E 01
4	5	1.361E 02
4	6	1.624E 02
4	7	1.658E 02
4	8	1.838E 02
4	9	1.691E 02
4	10	2.446E 02
5	1	1.120E 01
5	2	1.448E 01
5	3	5.633E 01
5	4	1.147E 02
5	5	1.454E 02
5	6	1.326E 02
5	7	1.916E 02
5	8	2.226E 02
5	9	2.016E 02
5	10	3.133E 02
6	1	2.446E 00
6	2	1.142E 01
6	3	1.140E 01
6	4	1.730E 01
6	5	1.000E 01
6	6	2.744E 01
6	7	2.793E 01
6	8	2.951E 01
6	9	3.040E 01
6	10	3.940E 01
7	1	2.155E 00
7	2	1.051E 01
7	3	1.107E 01
7	4	1.567E 01
7	5	1.015E 01
7	6	2.508E 01
7	8	2.711E 01
7	9	2.734E 01
7	10	3.491E 01
8	1	8.367E 00
8	2	1.531E 01
8	3	1.617E 01
8	4	2.351E 01
8	5	2.929E 01
8	6	4.004E 01
8	7	3.820E 01
8	8	4.247E 01
8	9	4.660E 01
8	10	5.881E 01
9	1	2.337E 01
9	2	2.111E 01
9	3	2.062E 01
9	4	4.102E 01
9	5	5.542E 01
9	6	6.861E 01
9	7	7.000E 01
9	8	7.449E 01
9	9	7.578E 01
9	10	8.815E 01
10	1	1.114E 01
10	2	1.827E 01
10	3	6.120E 01
10	4	8.470E 01
10	5	9.530E 01
10	6	1.302E 02
10	7	1.400E 02
10	8	1.553E 02
10	9	1.364E 02
11	1	1.706E 01
11	2	1.104E 02
11	3	1.131E 02
11	4	1.538E 02
11	5	2.011E 02
11	6	2.675E 02
11	7	2.471E 02
11	8	2.917E 02
11	9	2.657E 02
11	10	2.888E 02
12	1	1.911E 01
12	2	1.914E 02
12	3	1.976E 02
12	4	1.451E 02
12	5	1.837E 02
12	6	2.541E 02
12	7	2.283E 02
12	8	2.438E 02
12	9	2.505E 02
12	10	2.945E 02

Table III (CONCLUDED)

RUN	GAGE	$\dot{q}_{av}$
13	1	2.933E 01
13	2	1.306E 02
13	3	1.539E 02
13	4	2.073E 02
13	5	2.662E 02
13	6	3.594E 02
13	7	3.913E 02
13	8	3.670E 02
13	9	3.787E 02
13	10	4.180E 02
14	1	2.444E 01
14	2	1.165E 02
14	3	1.233E 02
14	4	1.603E 02
14	5	1.960E 02
14	6	2.133E 02
14	7	2.400E 02
14	8	1.974E 02
14	9	2.058E 02
14	10	2.442E 02
15	1	2.007E 02
15	2	2.017E 02
15	3	2.067E 02
15	4	2.640E 02
15	5	3.331E 02
15	6	4.122E 02
15	7	4.038E 02
15	8	4.325E 02
15	9	3.878E 02
15	10	4.024E 02
16	1	3.024E 02
16	2	2.856E 02
16	3	2.936E 02
16	4	3.785E 02
16	5	4.458E 02
16	6	5.440E 02
16	7	5.231E 02
16	8	5.376E 02
16	9	5.113E 02
16	10	5.655E 02

RUN	GAGE	$\dot{q}_{av}$
17	1	7.112E 01
17	2	1.423E 02
17	3	1.550E 02
17	4	1.994E 02
17	5	2.577E 02
17	6	3.268E 02
17	7	3.075E 02
17	8	3.342E 02
17	9	3.247E 02
17	10	3.474E 02

Table IV

TWO-DIMENSIONAL MODEL PRESSURE DATA

RUN	GAGE	M_∞	P	P/P_∞
1	1	1.104E 01	2.966E-01	2.221E 00
1	2	1.104E 01	2.691E-01	2.085E 00
1	3	1.104E 01	2.922E-01	2.264E 00
1	4	1.104E 01	3.897E-01	3.019E 00
1	5	1.104E 01	5.912E-01	4.581E 00
1	6	1.104E 01	8.391E-01	6.502E 00
1	7	1.104E 01	1.077E 00	8.342E 00
1	8	1.104E 01	1.320E 00	1.023E 01
1	9	1.104E 01	1.656E 00	1.283E 01
1	10	1.104E 01	2.219E 00	1.720E 01
1	11	1.104E 01	2.391E 00	1.845E 01
1	12	1.104E 01	2.733E 00	2.118E 01
1	13	1.104E 01	3.003E 00	2.327E 01
1	14	1.104E 01	3.356E 00	2.601E 01
2	1	1.118E 01	3.993E-01	2.050E 00
2	2	1.118E 01	3.624E-01	1.860E 00
2	3	1.118E 01	3.760E-01	1.946E 00
2	4	1.118E 01	5.148E-01	2.643E 00
2	5	1.118E 01	7.922E-01	4.066E 00
2	6	1.118E 01	1.197E 00	6.142E 00
2	7	1.118E 01	1.612E 00	8.273E 00
2	8	1.118E 01	1.989E 00	1.021E 01
2	9	1.118E 01	2.579E 00	1.324E 01
2	10	1.118E 01	3.422E 00	1.757E 01
2	11	1.118E 01	3.646E 00	1.872E 01
2	12	1.118E 01	4.261E 00	2.187E 01
2	13	1.118E 01	4.530E 00	2.330E 01
2	14	1.118E 01	4.890E 00	2.510E 01
3	4	1.127E 01	6.661E-01	3.401E 00
3	5	1.127E 01	1.021E 00	5.089E 00
3	6	1.127E 01	1.526E 00	5.959E 00
3	7	1.127E 01	2.062E 00	8.053E 00
3	8	1.127E 01	2.562E 00	1.000E 01
3	9	1.127E 01	3.388E 00	1.323E 01
3	10	1.127E 01	4.514E 00	1.763E 01
3	11	1.127E 01	5.046E 00	1.971E 01
3	13	1.127E 01	6.336E 00	2.474E 01
3	14	1.127E 01	6.637E 00	2.592E 01

Table IV (CONTINUED)

RUN	GAGE	M_∞	P	P/P_∞
4	2	9.454E 00	6.906E-01	1.914E 00
4	3	9.454E 00	6.916E-01	1.917E 00
4	4	9.454E 00	7.678E-01	2.447E 00
4	5	9.454E 00	1.106E 00	3.524E 00
4	6	9.454E 00	1.544E 00	4.922E 00
4	7	9.454E 00	1.959E 00	6.243E 00
4	8	9.454E 00	2.400E 00	7.679E 00
4	9	9.454E 00	2.837E 00	9.679E 00
4	10	9.454E 00	3.933E 00	1.253E 01
4	11	9.454E 00	4.381E 00	1.396E 01
4	12	9.454E 00	5.014E 00	1.598E 01
4	13	9.454E 00	5.545E 00	1.767E 01
4	14	9.454E 00	5.782E 00	1.843E 01
5	2	9.544E 00	7.046E-01	1.695E 00
5	3	9.544E 00	7.530E-01	1.812E 00
5	4	9.544E 00	9.699E-01	2.334E 00
5	5	9.544E 00	1.433E 00	3.449E 00
5	6	9.544E 00	2.052E 00	4.937E 00
5	7	9.544E 00	2.641E 00	6.353E 00
5	8	9.544E 00	3.187E 00	7.668E 00
5	9	9.544E 00	4.012E 00	9.654E 00
5	10	9.544E 00	5.228E 00	1.258E 01
5	11	9.544E 00	5.774E 00	1.389E 01
5	12	9.544E 00	6.641E 00	1.598E 01
5	13	9.544E 00	7.244E 00	1.743E 01
5	14	9.544E 00	7.547E 00	1.816E 01
6	2	7.892E 00	6.007E-01	1.965E 00
6	3	7.892E 00	6.226E-01	2.037E 00
6	4	7.892E 00	8.000E-01	2.617E 00
6	5	7.892E 00	1.030E 00	3.398E 00
6	6	7.892E 00	1.368E 00	4.475E 00
6	7	7.892E 00	1.707E 00	5.583E 00
6	8	7.892E 00	2.002E 00	6.548E 00
6	9	7.892E 00	2.419E 00	7.913E 00
6	10	7.892E 00	3.028E 00	9.904E 00
6	11	7.892E 00	3.296E 00	1.078E 01
6	13	7.892E 00	4.047E 00	1.324E 01
6	14	7.892E 00	4.141E 00	1.361E 01

Table IV (CONTINUED)

RUN	GAGE	M_∞	P	P/P_∞
7	1	7.893E 00	5.786E-01	1.086E 00
7	2	7.893E 00	5.714E-01	1.061E 00
7	3	7.893E 00	6.104E-01	2.095E 00
7	4	7.893E 00	7.689E-01	2.636E 00
7	5	7.893E 00	1.019E 00	3.465E 00
7	6	7.893E 00	1.327E 00	4.556E 00
7	7	7.893E 00	1.650E 00	5.665E 00
7	8	7.893E 00	1.939E 00	6.655E 00
7	9	7.893E 00	2.306E 00	7.914E 00
7	10	7.893E 00	2.901E 00	9.959E 00
7	11	7.893E 00	3.094E 00	1.062E 01
7	12	7.893E 00	3.540E 00	1.215E 01
7	13	7.893E 00	3.906E 00	1.340E 01
7	14	7.893E 00	4.101E 00	1.408E 01
8	1	7.892E 00	1.073E 00	1.085E 00
8	2	7.892E 00	1.030E 00	1.005E 00
8	3	7.892E 00	1.065E 00	1.071E 00
8	4	7.892E 00	1.419E 00	2.624E 00
8	5	7.892E 00	1.898E 00	3.513E 00
8	6	7.892E 00	2.517E 00	4.657E 00
8	7	7.892E 00	3.124E 00	5.780E 00
8	8	7.892E 00	3.655E 00	6.762E 00
8	9	7.892E 00	4.337E 00	8.025E 00
8	10	7.892E 00	5.461E 00	1.010E 01
8	11	7.892E 00	5.810E 00	1.075E 01
8	12	7.892E 00	6.979E 00	1.291E 01
8	13	7.892E 00	7.244E 00	1.340E 01
8	14	7.892E 00	7.673E 00	1.420E 01
9	1	8.127E 00	2.206E 00	2.121E 00
9	2	8.127E 00	2.051E 00	1.971E 00
9	3	8.127E 00	2.104E 00	2.022E 00
9	4	8.127E 00	2.570E 00	2.471E 00
9	5	8.127E 00	3.744E 00	3.601E 00
9	6	8.127E 00	4.852E 00	4.664E 00
9	7	8.127E 00	5.909E 00	5.680E 00
9	8	8.127E 00	7.036E 00	6.763E 00
9	9	8.127E 00	8.350E 00	8.026E 00
9	10	8.127E 00	1.060E 01	1.019E 01
9	11	8.127E 00	1.161E 01	1.116E 01
9	12	8.127E 00	1.321E 01	1.269E 01
9	13	8.127E 00	1.459E 01	1.403E 01
9	14	8.127E 00	1.554E 01	1.494E 01
10	1	6.805E 00	1.209E 00	1.653E 00
10	2	6.805E 00	1.112E 00	1.521E 00
10	3	6.805E 00	1.168E 00	1.597E 00

Table IV (CONTINUED)

RUN	GAGE	M_∞	P	P/P_∞
10	4	6.8056E 00	1.453E 00	1.987E 00
10	5	6.8056E 00	1.939E 00	2.640E 00
10	6	6.8056E 00	2.593E 00	3.532E 00
10	7	6.8056E 00	3.244E 00	4.465E 00
10	8	6.8056E 00	3.698E 00	5.058E 00
10	9	6.8056E 00	4.399E 00	6.016E 00
10	10	6.8056E 00	5.450E 00	7.454E 00
10	11	6.8056E 00	6.187E 00	8.461E 00
10	12	6.8056E 00	6.545E 00	8.951E 00
10	13	6.8056E 00	7.325E 00	1.002E 01
10	14	6.8056E 00	7.205E 00	9.853E 00
11	2	6.8688E 00	2.432E 00	1.587E 00
11	4	6.8688E 00	3.089E 00	2.016E 00
11	6	6.8688E 00	5.494E 00	3.716E 00
11	8	6.8688E 00	7.647E 00	4.991E 00
11	12	6.8688E 00	1.438E 01	9.385E 00
11	14	6.8688E 00	1.574E 01	1.027E 01
12	1	6.8790E 00	2.574E 00	1.709E 00
12	2	6.8790E 00	2.368E 00	1.571E 00
12	3	6.8790E 00	2.573E 00	1.707E 00
12	4	6.8790E 00	2.948E 00	1.956E 00
12	5	6.8790E 00	4.155E 00	.757E 00
12	6	6.8790E 00	5.576E 00	3.699E 00
12	7	6.8790E 00	6.725E 00	4.462E 00
12	8	6.8790E 00	7.603E 00	5.045E 00
12	9	6.8790E 00	9.260E 00	6.144E 00
12	10	6.8790E 00	1.120E 01	7.430E 00
12	11	6.8790E 00	1.253E 01	8.316E 00
12	12	6.8790E 00	1.410E 01	9.412E 00
12	13	6.8790E 00	1.506E 01	9.990E 00
12	14	6.8790E 00	1.505E 01	1.058E 01
13	1	6.9556E 00	3.902E 00	1.737E 00
13	2	6.9556E 00	3.646E 00	1.666E 00
13	3	6.9556E 00	3.947E 00	1.758E 00
13	4	6.9556E 00	4.544E 00	2.076E 00
13	5	6.9556E 00	6.232E 00	2.849E 00
13	6	6.9556E 00	8.305E 00	3.795E 00
13	7	6.9556E 00	9.955E 00	4.503E 00
13	8	6.9556E 00	1.147E 01	5.239E 00
13	9	6.9556E 00	1.382E 01	6.316E 00
13	10	6.9556E 00	1.595E 01	7.439E 00
13	11	6.9556E 00	1.943E 01	8.423E 00
13	12	6.9556E 00	2.090E 01	9.552E 00
13	13	6.9556E 00	2.239E 01	1.023E 01
13	14	6.9556E 00	2.403E 01	1.098E 01

Table IV (CONTINUED)

RUN	GAGE	M_∞	P	P/P_∞
14	1	6.798E 00	4.257E 00	5.809E 00
14	2	6.798E 00	3.749E 00	5.116E 00
14	3	6.798E 00	3.963E 00	5.409E 00
14	4	6.798E 00	4.519E 00	6.167E 00
14	5	6.798E 00	5.750E 00	7.847E 00
14	6	6.798E 00	7.434E 00	1.015E 01
14	7	6.798E 00	8.471E 00	1.156E 01
14	8	6.798E 00	9.100E 00	1.242E 01
14	9	6.798E 00	1.104E 01	1.507E 01
14	10	6.798E 00	1.261E 01	1.721E 01
14	11	6.798E 00	1.353E 01	1.846E 01
14	12	6.798E 00	1.482E 01	2.023E 01
14	13	6.798E 00	1.520E 01	2.074E 01
14	14	6.798E 00	1.592E 01	2.173E 01
15	1	6.868E 00	2.691E 00	3.370E 00
15	2	6.868E 00	2.785E 00	5.315E 00
15	3	6.868E 00	2.592E 00	5.646E 00
15	4	6.868E 00	2.399E 00	6.178E 00
15	5	6.868E 00	1.156E 01	7.530E 00
15	6	6.868E 00	1.449E 01	9.527E 00
15	7	6.868E 00	1.719E 01	1.129E 01
15	8	6.868E 00	1.836E 01	1.207E 01
15	9	6.868E 00	2.146E 01	1.411E 01
15	10	6.868E 00	2.400E 01	1.543E 01
15	11	6.868E 00	2.734E 01	1.799E 01
15	12	6.868E 00	2.996E 01	1.970E 01
15	13	6.868E 00	3.095E 01	2.036E 01
15	14	6.868E 00	3.302E 01	2.171E 01
16	2	6.956E 00	1.275E 01	5.853E 00
16	3	6.956E 00	1.250E 01	5.742E 00
16	4	6.956E 00	1.411E 01	6.479E 00
16	5	6.956E 00	1.761E 01	8.085E 00
16	6	6.956E 00	2.217E 01	1.018E 01
16	7	6.956E 00	2.612E 01	1.199E 01
16	8	6.956E 00	2.714E 01	1.246E 01
16	9	6.956E 00	3.284E 01	1.509E 01
16	10	6.956E 00	3.815E 01	1.752E 01
16	11	6.956E 00	4.077E 01	1.872E 01
16	12	6.956E 00	4.530E 01	2.080E 01
16	13	6.956E 00	4.642E 01	2.132E 01
16	14	6.956E 00	4.800E 01	2.204E 01

Table IV (CONCLUDED)

RUN	GAGE	M_∞	P	P/P_∞
17	1	6.9685E 00	4.617E 00	3.083E 00
17	2	6.9685E 00	4.587E 00	3.063E 00
17	3	6.9685E 00	4.943E 00	3.234E 00
17	4	6.9685E 00	5.424E 00	3.622E 00
17	5	6.9685E 00	7.586E 00	5.066E 00
17	6	6.9685E 00	8.968E 00	5.989E 00
17	7	6.9685E 00	1.031E 01	6.885E 00
17	8	6.9685E 00	1.191E 01	7.954E 00
17	9	6.9685E 00	1.427E 01	9.529E 00
17	10	6.9685E 00	1.682E 01	1.123E 01
17	11	6.9685E 00	1.923E 01	1.284E 01
17	12	6.9685E 00	2.117E 01	1.414E 01
17	13	6.9685E 00	2.333E 01	1.558E 01
17	14	6.9685E 00	2.366E 01	1.580E 01

Table V

RUN SCHEDULE AND TEST CONDITIONS FOR THE AXISYMMETRIC MODEL TESTS

RUN NO.	19	20	21	22	23	24	25	26
α	0.0	0.0	0.0	0.0	0.0	0.0	0.0	0.0
ψ	0.0	0.0	0.0	0.0	0.0	0.0	0.0	0.0
ϕ	0.0	0.0	0.0	0.0	0.0	0.0	0.0	0.0
M_i	3.124E 00	3.152E 00	4.355E 00	5.134E 00	3.220E 00	3.390E 00	2.631E 00	2.491E 00
P_o	9.427E 03	9.502E 03	1.258E 04	9.875E 03	1.437E 04	2.063E 04	1.293E 03	2.096E 03
H_o	1.643E 07	1.662E 07	3.719E 07	3.912E 07	1.714E 07	1.870E 07	1.199E 07	1.101E 07
T_o	2.571E 03	2.598E 03	5.152E 03	5.364E 03	2.681E 03	2.928E 03	1.895E 03	1.741E 03
M_∞	1.113E 01	1.112E 01	9.752E 00	9.568E 00	1.127E 01	1.137E 01	7.777E 00	7.887E 00
U_∞	5.623E 03	5.655E 03	8.409E 03	8.617E 03	5.728E 03	6.004E 03	4.709E 03	4.516E 03
T_∞	1.062E 02	1.075E 02	3.091E 02	3.373E 02	1.075E 02	1.156E 02	1.525E 02	1.363E 02
P_∞	1.171E-01	1.181E-01	2.357E-01	1.978E-01	1.775E-01	2.409E-01	1.584E-01	2.447E-01
q_∞	1.016E 01	1.024E 01	1.571E 01	1.269E 01	1.579E 01	2.183E 01	6.711E 00	1.067E 01
ρ_∞	3.257E-05	3.221E-05	6.309E-05	4.922E-05	1.395E-04	1.744E-04	8.716E-05	1.506E-04
μ_∞	3.932E-08	3.946E-08	2.477E-07	2.670E-07	9.040E-08	9.750E-08	1.278E-07	1.145E-07
Re/FT	5.838E 06	5.765E 06	2.172E 06	1.598E 06	8.783E 06	1.074E 07	3.212E 06	5.943E 06
P'_o	1.880E 01	1.895E 01	2.952E 01	2.388E 01	2.924E 01	4.047E 01	1.237E 01	1.964E 01
T'_o	8.368E 02	8.427E 02	1.556E 03	1.620E 03	8.554E 02	9.132E 02	7.029E 02	6.658E 02
$\frac{\mu^*}{\sqrt{C^*}}$	5.397E-07	5.333E-07	7.940E-07	8.139E-07	5.389E-07	5.635E-07	4.692E-07	4.512E-07
	8.683E-01	8.674E-01	7.380E-01	7.966E-01	8.654E-01	8.566E-01	8.925E-01	8.983E-01
H_w	3.237E 06	3.231E 06	3.237E 06	3.213E 06	3.219E 06	3.231E 06	3.195E 06	3.195E 06
T_w	5.390E 02	5.382E 02	5.390E 02	5.350E 02	5.360E 02	5.380E 02	5.320E 02	5.320E 02
P_{ts}	1.934E-05	1.934E-05	1.934E-05	1.934E-05	1.934E-05	1.934E-05	3.869E-05	1.934E-05
NOSE	SHARP LEADING EDGE HOLLOW CYLINDER ⟶							

Table V (CONCLUDED)

RUN NO.	27	29	29	30	31	32	33
α	0.0	0.0	0.0	0.0	0.0	0.0	0.0
ψ	0.0	0.0	0.0	0.0	0.0	0.0	0.0
ϕ	0.0	0.0	0.0	0.0	0.0	0.0	0.0
M_i	2.564E 00	4.874E 00	4.990E 00	2.310E 00	4.842E 00	4.744E 00	4.912E 00
P_o	4.430E 03	1.038E 03	4.121E 03	1.122E 03	2.016E 03	1.857E 03	4.231E 03
H_o	1.133E 07	3.551E 07	3.564E 07	9.886E 06	3.481E 07	3.366E 07	3.593E 07
T_o	1.833E 03	4.937E 03	4.955E 03	1.552E 03	4.854E 03	4.723E 03	4.992E 03
M_∞	7.200E 00	4.743E 00	6.792E 00	7.813E 00	6.756E 00	6.785E 00	6.786E 00
U_∞	4.5[illegible]E 03	7.997E 03	8.018E 03	4.277E 03	7.931E 03	7.793E 03	8.059E 03
T_∞	1.[illegible]E 03	5.859E 02	5.904E 02	1.244E 02	5.722E 02	5.493E 02	5.859E 02
P_∞	5.[illegible]E-01	3.769E-01	7.785E-01	1.392E-01	3.930E-01	3.593E-01	7.991E-01
q_∞	2.[illegible]E 01	1.196E 01	2.513E 01	5.913E 00	1.252E 01	1.159E 01	2.575E 01
ρ_∞	3.091E-04	5.386E-05	1.126E-04	9.308E-05	5.749E-05	5.430E-05	1.145E-04
μ_∞	1.153E-07	4.104E-07	4.074E-07	1.047E-07	4.031E-07	3.907E-07	4.104E-07
Re/FT	1.230E 07	1.049E 06	2.215E 06	3.801E 06	1.139E 06	1.095E 06	2.245E 06
P'_o	4.158E 01	2.271E 01	4.772E 01	1.087E 01	2.377E 01	2.155E 01	4.891E 01
T'_o	6.762E 02	1.576E 03	1.579E 03	6.268E 02	1.551E 03	1.511E 03	1.589E 03
M'	4.563E-07	8.004E-07	8.012E-07	4.316E-07	7.925E-07	7.797E-07	8.044E-07
$\sqrt{C'}$	9.965E-01	9.515E-01	9.502E-01	9.951E-01	9.517E-01	9.519E-01	9.501E-01
H_w	3.199E 06	3.201E 06	3.201E 06	3.207E 06	3.199E 06	3.195E 06	3.201E 06
T_w	5.310E 02	5.330E 02	5.330E 02	5.340E 02	5.310E 02	5.320E 02	5.330E 02
P_{ts}	1.934E-05	1.934E-05	1.934E-05	1.934E-05	1.934E-05	1.934E-05	1.934E-05
NOSE	SHARP LEADING EDGE HOLLOW CYLINDER ⟶				BLUNT ⟶		

Table VI

AXISYMMETRIC MODEL SKIN FRICTION DATA

RUN	GAGE	M_∞	τ
19	1	1.113E 01	6.774E-03
19	16	1.113E 01	9.455E-03
19	3	1.113E 01	1.463E-02
19	4	1.113E 01	1.787E-02
19	5	1.113E 01	2.341E-02
19	6	1.113E 01	3.120E-02
19	7	1.113E 01	3.788E-02
19	8	1.113E 01	4.878E-02
19	9	1.113E 01	7.581E-02
19	12	1.113E 01	1.523E-01
19	13	1.113E 01	2.829E-01
20	1	1.112E 01	7.135E-03
20	16	1.112E 01	9.411E-03
20	3	1.112E 01	1.473E-02
20	4	1.112E 01	1.733E-02
20	5	1.112E 01	2.344E-02
20	6	1.112E 01	3.214E-02
20	7	1.112E 01	3.912E-02
20	8	1.112E 01	4.988E-02
20	9	1.112E 01	7.944E-02
20	11	1.112E 01	1.178E-01
20	12	1.112E 01	1.493E-01
20	13	1.112E 01	2.339E-01
20	15	1.112E 01	5.085E-01
21	1	9.752E 00	4.445E-03
21	16	9.752E 00	5.927E-03
21	3	9.752E 00	9.116E-03
21	4	9.752E 00	1.091E-02
21	5	9.752E 00	1.488E-02
21	7	9.752E 00	2.482E-02
21	8	9.752E 00	1.115E-01
21	9	9.752E 00	1.809E-01
21	11	9.752E 00	1.867E-01
21	12	9.752E 00	2.794E-01
21	13	9.752E 00	4.783E-01

Table VI (CONTINUED)

RUN	GAGE	M_∞	τ
22	1	9.568E 00	3.204E-03
22	14	9.568E 00	1.433E-01
22	3	9.568E 00	2.193E-02
22	4	9.568E 00	3.004E-02
22	5	9.568E 00	4.712E-02
22	6	9.568E 00	8.043E-02
22	7	9.568E 00	5.835E-02
22	8	9.568E 00	7.425E-02
22	9	9.568E 00	1.210E-01
22	11	9.568E 00	1.787E-01
22	12	9.568E 00	2.268E-01
22	13	9.568E 00	5.042E-01
23	1	1.127E 01	7.785E-03
23	14	1.127E 01	1.332E-01
23	3	1.127E 01	1.660E-02
23	4	1.127E 01	2.174E-02
23	5	1.127E 01	3.210E-02
23	6	1.127E 01	4.820E-02
23	7	1.127E 01	5.035E-02
23	8	1.127E 01	7.078E-02
23	9	1.127E 01	1.118E-01
23	11	1.127E 01	1.613E-01
23	12	1.127E 01	2.138E-01
23	13	1.127E 01	3.965E-01
23	15	1.127E 01	1.120E 00
24	1	1.137E 01	1.435E-02
24	14	1.137E 01	1.941E-01
24	3	1.137E 01	1.984E-02
24	4	1.137E 01	2.417E-02
24	5	1.137E 01	4.144E-02
24	6	1.137E 01	6.991E-02
24	7	1.137E 01	6.065E-02
24	8	1.137E 01	8.537E-02
24	9	1.137E 01	1.309E-01

Table VI (CONTINUED)

RUN	GAGE	M_∞	τ
25	1	7.777E 00	7.413E-03
25	16	7.777E 00	4.050E-02
25	3	7.777E 00	9.279E-03
25	4	7.777E 00	1.027E-02
25	5	7.777E 00	1.253E-02
25	6	7.777E 00	1.904E-02
25	7	7.777E 00	2.243E-02
25	8	7.777E 00	2.636E-02
25	9	7.777E 00	4.112E-02
25	11	7.777E 00	5.276E-02
25	12	7.777E 00	5.768E-02
25	13	7.777E 00	8.048E-02
25	14	7.777E 00	4.491E-01
26	1	7.887E 00	1.045E-02
26	16	7.887E 00	7.253E-02
26	3	7.887E 00	1.324E-02
26	4	7.887E 00	1.529E-02
26	5	7.887E 00	2.066E-02
26	6	7.887E 00	2.602E-02
26	7	7.887E 00	3.384E-02
26	8	7.887E 00	4.103E-02
26	9	7.887E 00	4.005E-02
26	11	7.887E 00	8.067E-02
26	12	7.887E 00	9.582E-02
26	13	7.887E 00	1.547E-01
26	14	7.887E 00	1.211E 00
26	15	7.887E 00	1.469E 00
27	1	7.990E 00	1.458E-02
27	16	7.990E 00	1.543E-01
27	3	7.990E 00	2.110E-02
27	4	7.990E 00	2.363E-02
27	5	7.990E 00	3.534E-02
27	6	7.990E 00	4.660E-02
27	7	7.990E 00	6.384E-02
27	8	7.990E 00	8.130E-02
27	9	7.990E 00	1.257E-01
27	11	7.990E 00	1.434E-01
27	12	7.990E 00	1.959E-01
27	13	7.990E 00	3.444E-01
27	14	7.990E 00	3.076E 00
27	15	7.990E 00	3.419E 00

Table VI (CONCLUDED)

RUN	GAGE	M_∞	τ
28	1	6.742E 00	1.595E-02
28	14	6.742E 00	1.005E-01
28	3	6.742E 00	2.473E-02
28	4	6.742E 00	2.624E-02
28	5	6.742E 00	2.906E-02
28	6	6.742E 00	4.860E-02
28	7	6.742E 00	5.307E-02
28	8	6.742E 00	5.811E-02
28	9	6.742E 00	8.910E-02
28	11	6.742E 00	1.335E-01
28	12	6.742E 00	1.413E-01
28	13	6.742E 00	2.629E-01
29	1	6.792E 00	3.336E-02
29	14	6.792E 00	1.730E-01
29	3	6.792E 00	3.548E-02
29	4	6.792E 00	3.663E-02
29	5	6.792E 00	4.154E-02
29	6	6.792E 00	6.414E-02
29	7	6.792E 00	7.974E-02
29	8	6.792E 00	8.110E-02
29	9	6.792E 00	1.449E-01
29	11	6.792E 00	2.274E-01
29	12	6.792E 00	2.719E-01
29	13	6.792E 00	4.706E-01
29	14	6.792E 00	2.868E 00
29	15	6.792E 00	3.140E 00
30	1	7.813E 00	6.116E-03
30	14	7.813E 00	3.785E-02
30	3	7.813E 00	8.430E-03
30	4	7.813E 00	9.273E-03
30	5	7.813E 00	1.208E-02
30	6	7.813E 00	1.225E-02
30	7	7.813E 00	1.820E-02
30	8	7.813E 00	2.095E-02
30	9	7.813E 00	3.049E-02
30	11	7.813E 00	4.423E-02
30	12	7.813E 00	4.512E-02
30	14	7.813E 00	4.452E-01
30	15	7.813E 00	6.042E-01

Table VII

AXISYMMETRIC MODEL HEAT TRANSFER DATA

RUN	GAGE	$\dot{q}_{av}$	RUN	GAGE	$\dot{q}_{av}$
19	1	3.989E	23	1	5.190E 00
19	2	9.151E	23	2	1.150E 01
19	3	1.147E	23	3	1.531E 01
19	4	2.381E	23	4	3.421E 01
19	5	3.853E	23	5	4.424E 01
19	6	6.788E	23	6	1.040E 02
19	7	1.033E	23	7	1.350E 02
			23	8	2.151E 02
			23	9	3.145E 02
			23	10	3.442E 02
20	1	4.394E	24	1	7.676E 00
20	2	9.583E	24	2	1.747E 01
20	3	1.228E	24	3	2.910E 01
20	4	2.504E	24	4	4.933E 01
20	5	4.198E	24	5	9.288E 01
20	6	6.733E	24	6	1.487E 02
20	7	1.060E	24	7	2.230E 02
20	8	1.600E	24	8	3.511E 02
20	9	2.290E	24	9	4.283E 02
20	10	2.772E	24	10	4.302E 02
21	1	4.186E	25	1	2.416E 00
21	2	3.477E	25	2	5.151E 00
21	3	4.730E	25	3	5.710E 00
21	4	8.856E	25	4	1.028E 01
21	5	1.530E	25	5	1.647E 01
21	6	2.424E	25	6	2.414E 01
21	7	3.815E	25	7	3.231E 01
21	8	6.088E	25	8	4.824E 01
21	9	8.417E	25	9	6.802E 01
21	10	1.006E	25	10	8.730E 01
22	1	3.434E	26	1	3.130E 00
22	2	3.146E	26	2	6.491E 00
22	3	3.596E	26	3	8.170E 00
22	4	6.556E	26	4	1.412E 01
22	5	1.114E	26	5	2.015E 01
22	6	1.657E	26	6	3.067E 01
22	7	2.578E	26	7	4.330E 01
22	8	4.325E	26	8	6.935E 01
22	9	6.640E	26	9	9.039E 01
22	10	8.572E	26	10	1.071E 02

Table VII (CONCLUDED)

RUN	GAGE	$\dot{q}_{av}$
27	1	5.017E 00
27	2	1.255E 01
27	3	1.687E 01
27	4	2.962E 01
27	5	4.548E 01
27	6	6.534E 01
27	7	8.737E 01
27	8	1.275E 02
27	9	1.680E 02
27	10	2.036E 02
28	1	1.763E 01
28	2	2.930E 01
28	3	3.202E 01
28	4	5.761E 01
28	5	7.607E 01
28	6	1.235E 02
28	7	1.798E 02
28	8	2.693E 02
28	9	3.456E 02
28	10	4.841E 02
29	1	2.771E 01
29	2	4.708E 01
29	3	5.571E 01
29	4	9.502E 01
29	5	1.416E 02
29	6	2.114E 02
29	7	3.020E 02
29	8	4.337E 02
29	9	5.801E 02
29	10	7.363E 02
30	1	1.763E 00
30	2	3.437E 00
30	3	4.150E 00
30	4	7.607E 00
30	5	1.035E 01
30	6	1.695E 01
30	7	2.417E 01
30	8	3.443E 01
30	9	4.619E 01
30	10	6.015E 01
31	1	3.594E 00
31	2	6.165E 00
31	3	1.365E 01
31	4	2.234E 01
31	5	2.965E 01
31	6	4.541E 01
31	7	5.244E 01
31	8	7.711E 01
31	9	9.542E 01
31	10	1.439E 02
32	1	3.055E 00
32	2	6.414E 00
32	3	1.001E 01
32	4	1.892E 01
32	5	2.994E 01
32	6	4.214E 01
32	7	4.942E 01
32	8	6.585E 01
32	9	8.870E 01
32	10	1.358E 02
33	1	2.101E 01
33	2	2.434E 01
33	3	2.213E 01
33	4	4.434E 01
33	5	4.356E 01
33	6	1.192E 02
33	7	1.344E 02
33	8	2.017E 02
33	9	2.088E 02
33	10	4.191E 02

Table VIII

AXISYMMETRIC MODEL PRESSURE DATA

RUN	GAGE	M_∞	P	P/P_∞
19	1	1.113E 01	1.493E-01	1.275E 00
19	15	1.113E 01	2.080E 00	1.759E 01
19	3	1.113E 01	2.564E-01	2.189E 00
19	4	1.113E 01	3.511E-01	2.998E 00
19	8	1.113E 01	1.070E 00	9.133E 00
19	14	1.113E 01	2.167E 01	1.851E 02
20	1	1.112E 01	1.533E-01	1.307E 00
20	15	1.112E 01	2.068E 00	1.750E 01
20	3	1.112E 01	2.541E-01	2.151E 00
20	4	1.112E 01	3.564E-01	3.017E 00
20	5	1.112E 01	5.036E-01	4.263E 00
20	6	1.112E 01	6.234E-01	5.277E 00
20	7	1.112E 01	8.250E-01	6.989E 00
20	8	1.112E 01	1.077E 00	9.119E 00
20	9	1.112E 01	1.981E 00	1.677E 01
20	10	1.112E 01	3.820E 00	3.233E 01
20	11	1.112E 01	7.267E 00	6.151E 01
20	12	1.112E 01	1.188E 01	1.006E 02
20	13	1.112E 01	2.073E 01	1.755E 02
20	14	1.112E 01	2.208E 01	1.869E 02
21	1	9.752E 00	2.687E-01	1.149E 00
21	15	9.752E 00	3.627E 00	1.539E 01
21	3	9.752E 00	4.962E-01	2.105E 00
21	4	9.752E 00	6.585E-01	2.794E 00
21	5	9.752E 00	9.081E-01	3.853E 00
21	6	9.752E 00	1.095E 00	4.648E 00
21	7	9.752E 00	1.439E 00	6.104E 00
21	8	9.752E 00	1.915E 00	8.124E 00
21	9	9.752E 00	3.159E 00	1.357E 01
21	10	9.752E 00	6.698E 00	2.842E 01
21	11	9.752E 00	1.166E 01	4.949E 01
21	12	9.752E 00	2.041E 01	8.661E 01
21	13	9.752E 00	3.401E 01	1.443E 02
21	14	9.752E 00	4.279E 01	1.816E 02

Table VIII (CONTINUED)

RUN	GAGE	M_∞	P	P/P_∞
22	1	9.568E 00	2.144E-01	1.085E 00
22	15	9.568E 00	2.832E 00	1.432E 01
22	3	9.568E 00	4.048E-01	2.046E 00
22	4	9.568E 00	5.452E-01	2.756E 00
22	5	9.568E 00	7.682E-01	3.883E 00
22	6	9.568E 00	9.202E-01	4.651E 00
22	7	9.568E 00	1.193E 00	6.030E 00
22	9	9.568E 00	1.507E 00	7.616E 00
22	9	9.568E 00	2.696E 00	1.363E 01
22	10	9.568E 00	5.093E 00	2.574E 01
22	11	9.568E 00	8.838E 00	4.467E 01
22	12	9.568E 00	1.454E 01	7.351E 01
22	13	9.568E 00	2.605E 01	1.317E 02
22	14	9.568E 00	3.428E 01	1.733E 02
23	1	1.127E 01	1.939E-01	1.036E 00
23	15	1.127E 01	3.114E 00	1.754E 01
23	3	1.127E 01	3.456E-01	1.947E 00
23	4	1.127E 01	4.447E-01	2.505E 00
23	5	1.127E 01	6.906E-01	3.891E 00
23	6	1.127E 01	8.724E-01	4.915E 00
23	7	1.127E 01	1.195E 00	6.731E 00
23	9	1.127E 01	1.557E 00	8.771E 00
23	9	1.127E 01	2.783E 00	1.568E 01
23	10	1.127E 01	5.996E 00	3.378E 01
23	11	1.127E 01	9.706E 00	5.468E 01
23	12	1.127E 01	1.653E 01	9.314E 01
23	13	1.127E 01	2.716E 01	1.530E 02
23	14	1.127E 01	2.885E 01	1.625E 02

Table VIII (CONTINUED)

RUN	GAGE	M_∞	P	P/P_∞
24	1	1.137E 01	2.587E-01	1.074E 00
24	15	1.137E 01	4.460E 00	1.851E 01
24	3	1.137E 01	4.621E-01	1.919E 00
24	4	1.137E 01	5.992E-01	2.487E 00
24	5	1.137E 01	9.081E-01	3.769E 00
24	6	1.137E 01	1.215E 00	5.043E 00
24	7	1.137E 01	1.612E 00	6.690E 00
24	8	1.137E 01	2.185E 00	9.068E 00
24	9	1.137E 01	3.908E 00	1.591E 01
24	10	1.137E 01	8.354E 00	3.467E 01
24	11	1.137E 01	1.379E 01	5.725E 01
24	12	1.137E 01	2.391E 01	9.924E 01
24	13	1.137E 01	3.737E 01	1.551E 02
24	14	1.137E 01	3.900E 01	1.619E 02
25	15	7.777E 00	1.569E 00	9.997E 00
25	3	7.777E 00	2.726E-01	1.721E 00
25	4	7.777E 00	3.634E-01	2.294E 00
25	5	7.777E 00	4.971E-01	3.076E 00
25	6	7.777E 00	5.550E-01	3.505E 00
25	7	7.777E 00	6.952E-01	4.391E 00
25	8	7.777E 00	8.237E-01	5.264E 00
25	9	7.777E 00	1.394E 00	8.804E 00
25	10	7.777E 00	2.312E 00	1.460E 01
25	11	7.777E 00	3.691E 00	2.331E 01
25	12	7.777E 00	5.513E 00	3.481E 01
25	13	7.777E 00	9.656E 00	6.097E 01
25	14	7.777E 00	1.642E 01	1.037E 02
26	1	7.987E 00	2.585E-01	1.220E 00
26	15	7.987E 00	2.522E 00	1.031E 01
26	3	7.987E 00	4.411E-01	1.803E 00
26	4	7.987E 00	5.519E-01	2.256E 00
26	5	7.987E 00	7.764E-01	3.173E 00
26	6	7.987E 00	8.982E-01	3.671E 00
26	7	7.987E 00	1.125E 00	4.596E 00
26	8	7.987E 00	1.375E 00	5.618E 00
26	9	7.987E 00	2.214E 00	9.050E 00
26	10	7.987E 00	3.688E 00	1.507E 01
26	11	7.987E 00	6.284E 00	2.569E 01
26	12	7.987E 00	9.214E 00	3.766E 01
26	13	7.987E 00	1.568E 01	6.409E 01
26	14	7.987E 00	2.573E 01	1.052E 02

Table VIII (CONTINUED)

RUN	GAGE	M_∞	P	P/P_∞
27	1	7.980E 00	6.045E-01	1.195E 00
27	15	7.980E 00	5.867E 00	1.140E 01
27	3	7.980E 00	8.649E-01	1.710E 00
27	4	7.980E 00	1.095E 00	2.164E 00
27	5	7.980E 00	1.576E 00	3.115E 00
27	6	7.980E 00	2.000E 00	3.952E 00
27	7	7.980E 00	2.564E 00	5.068E 00
27	8	7.980E 00	3.079E 00	6.086E 00
27	9	7.980E 00	4.989E 00	9.862E 00
27	10	7.980E 00	8.610E 00	1.702E 01
27	11	7.980E 00	1.438E 01	2.842E 01
27	12	7.980E 00	2.121E 01	4.193E 01
27	13	7.980E 00	3.557E 01	7.030E 01
27	14	7.980E 00	5.947E 01	1.176E 02
28	1	6.742E 00	3.993E-01	1.062E 00
28	15	6.742E 00	2.939E 00	7.815E 00
28	3	6.742E 00	5.830E-01	1.551E 00
28	4	6.742E 00	7.135E-01	1.898E 00
28	5	6.742E 00	9.620E-01	2.558E 00
28	6	6.742E 00	1.099E 00	2.924E 00
28	7	6.742E 00	1.371E 00	3.645E 00
28	8	6.742E 00	1.648E 00	4.382E 00
28	9	6.742E 00	2.799E 00	7.443E 00
28	10	6.742E 00	4.568E 00	1.215E 01
28	11	6.742E 00	7.809E 00	2.077E 01
28	12	6.742E 00	1.051E 01	2.902E 01
28	13	6.742E 00	1.931E 01	4.870E 01
28	14	6.742E 00	3.250E 01	8.642E 01
29	1	6.792E 00	7.516E-01	9.655E-01
29	15	6.792E 00	5.770E 00	7.412E 00
29	3	6.792E 00	1.116E 00	1.433E 00
29	4	6.792E 00	1.359E 00	1.746E 00
29	5	6.792E 00	1.819E 00	2.336E 00
29	6	6.792E 00	2.091E 00	2.686E 00
29	7	6.792E 00	2.667E 00	3.426E 00
29	8	6.792E 00	3.258E 00	4.185E 00
29	9	6.792E 00	5.413E 00	6.954E 00
29	10	6.792E 00	8.610E 00	1.106E 01
29	11	6.792E 00	1.354E 01	1.739E 01
29	12	6.792E 00	2.003E 01	2.573E 01
29	13	6.792E 00	3.524E 01	4.527E 01
29	14	6.792E 00	5.769E 01	7.411E 01

Table VIII (CONTINUED)

RUN	GAGE	M_∞	P	P/P_∞
30	1	7.813E 00	1.524E-01	1.103E 00
30	15	7.813E 00	1.224E 00	8.868E 00
30	3	7.813E 00	2.305E-01	1.668E 00
30	4	7.813E 00	3.014E-01	2.181E 00
30	5	7.813E 00	3.924E-01	2.839E 00
30	6	7.813E 00	4.561E-01	3.300E 00
30	7	7.813E 00	5.555E-01	4.019E 00
30	8	7.813E 00	6.505E-01	4.094E 00
30	9	7.813E 00	1.128E 00	8.160E 00
30	10	7.813E 00	1.835E 00	1.328E 01
30	11	7.813E 00	3.004E 00	2.175E 01
30	12	7.813E 00	4.397E 00	3.181E 01
30	13	7.813E 00	7.390E 00	5.347E 01
30	14	7.813E 00	1.278E 01	9.250E 01
31	1	6.756E 00	4.727E-01	1.206E 00
31	15	6.756E 00	1.321E 00	3.371E 00
31	3	6.756E 00	4.817E-01	1.229E 00
31	4	6.756E 00	5.082E-01	1.296E 00
31	5	6.756E 00	6.105E-01	1.557E 00
31	6	6.756E 00	6.393E-01	1.631E 00
31	7	6.756E 00	7.932E-01	2.024E 00
31	8	6.756E 00	8.986E-01	2.292E 00
31	9	6.756E 00	1.394E 00	3.557E 00
31	10	6.756E 00	1.859E 00	4.743E 00
31	11	6.756E 00	2.554E 00	6.516E 00
31	12	6.756E 00	3.415E 00	8.711E 00
31	13	6.756E 00	5.439E 00	1.439E 01
31	14	6.756E 00	8.488E 00	2.165E 01
32	1	6.785E 00	4.329E-01	1.205E 00
32	15	6.785E 00	1.240E 00	3.451E 00
32	3	6.785E 00	4.199E-01	1.169E 00
32	4	6.785E 00	4.648E-01	1.294E 00
32	5	6.785E 00	5.389E-01	1.499E 00
32	6	6.785E 00	5.816E-01	1.619E 00
32	7	6.785E 00	6.913E-01	1.924E 00
32	8	6.785E 00	8.125E-01	2.262E 00
32	9	6.785E 00	1.185E 00	3.299E 00
32	10	6.785E 00	1.691E 00	4.707E 00
32	11	6.785E 00	2.478E 00	6.896E 00
32	12	6.785E 00	3.490E 00	9.602E 00
32	13	6.785E 00	4.919E 00	1.369E 01
32	14	6.785E 00	7.799E 00	2.171E 01

Table VIII (CONCLUDED)

RUN	GAGE	M_∞	P	P/P_∞
33	1	6.786E 00	9.210E-01	1.165E 00
33	15	6.786E 00	2.595E 00	3.248E 00
33	3	6.786E 00	9.519E-01	1.191E 00
33	4	6.786E 00	1.004E 00	1.256E 00
33	5	6.786E 00	1.224E 00	1.531E 00
33	6	6.786E 00	1.267E 00	1.585E 00
33	7	6.786E 00	1.562E 00	1.955E 00
33	8	6.786E 00	1.695E 00	2.121E 00
33	9	6.786E 00	2.768E 00	3.464E 00
33	10	6.786E 00	3.678E 00	4.603E 00
33	11	6.786E 00	5.517E 00	6.904E 00
33	12	6.786E 00	6.410E 00	8.021E 00
33	13	6.786E 00	1.087E 01	1.361E 01
33	14	6.786E 00	1.558E 01	1.950E 01

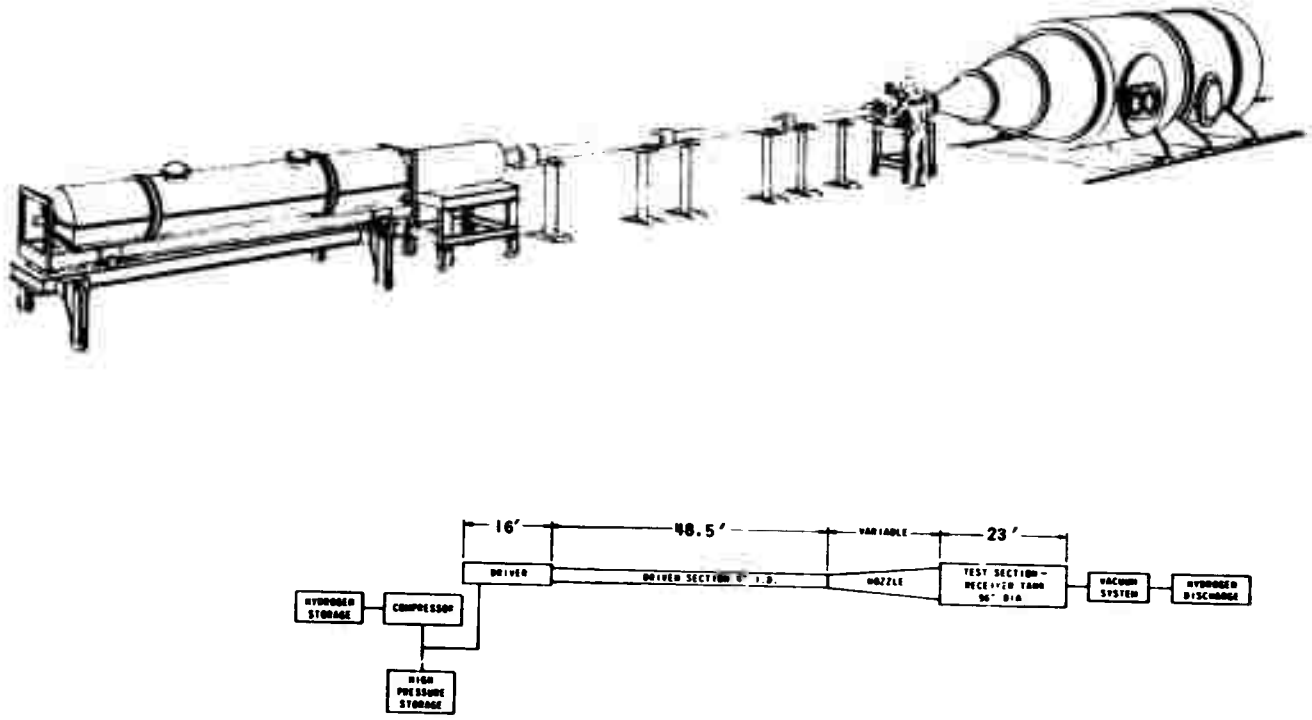

3416

Figure 1. BASIC COMPONENTS OF THE CAL 96" LEG HYPERSONIC SHOCK TUNNEL

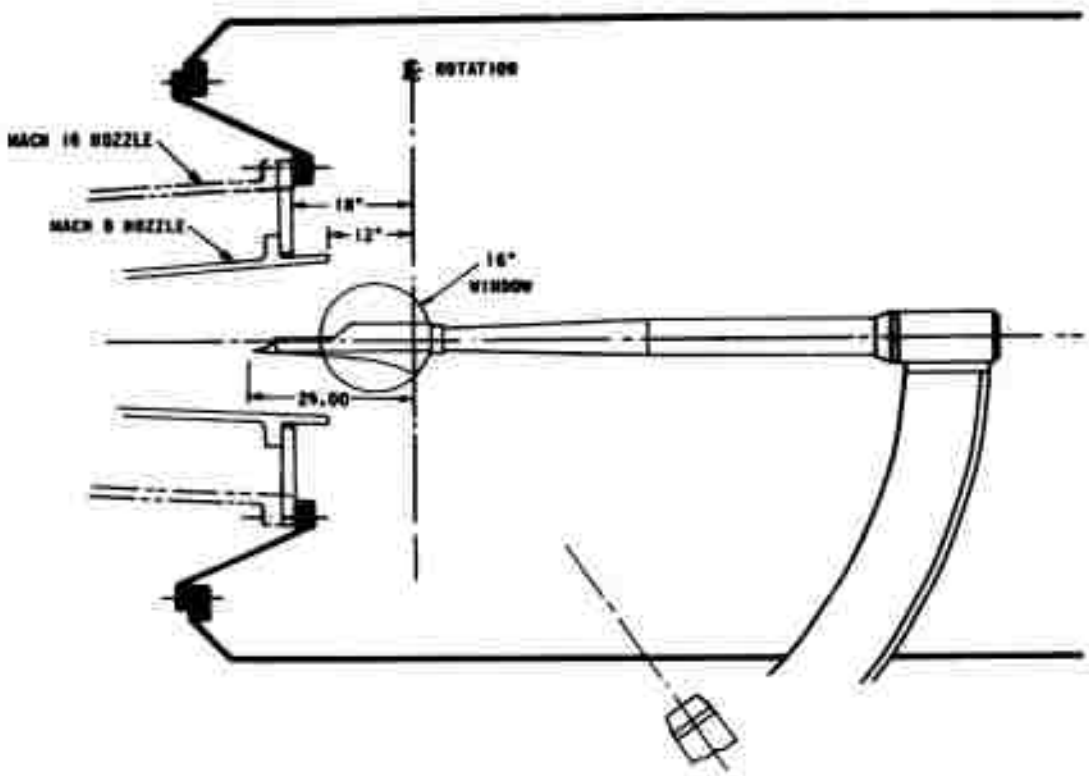

Figure 2 INSTALLATION OF THE TWO-DIMENSIONAL MODEL IN THE CAL 96" LEG HYPERSONIC SHOCK TUNNEL

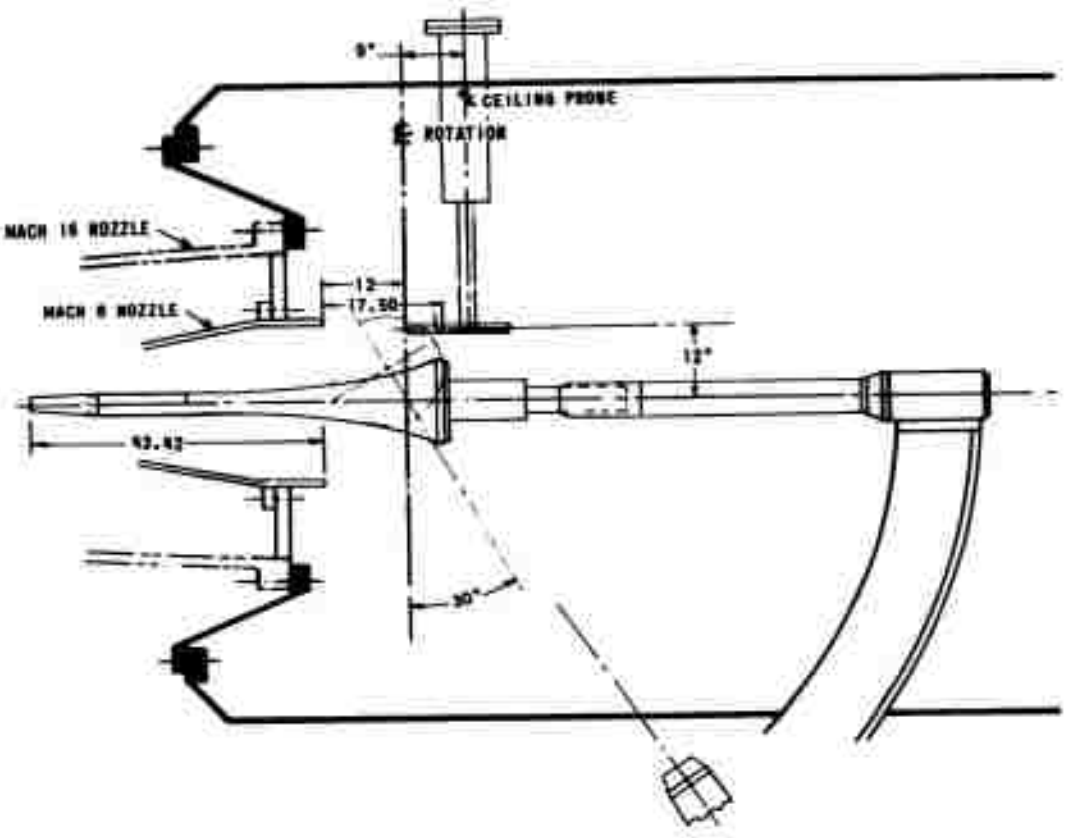

Figure 3 INSTALLATION OF THE AXISYMMETRIC MODEL IN THE CAL 96" LEG HYPERSONIC SHOCK TUNNEL

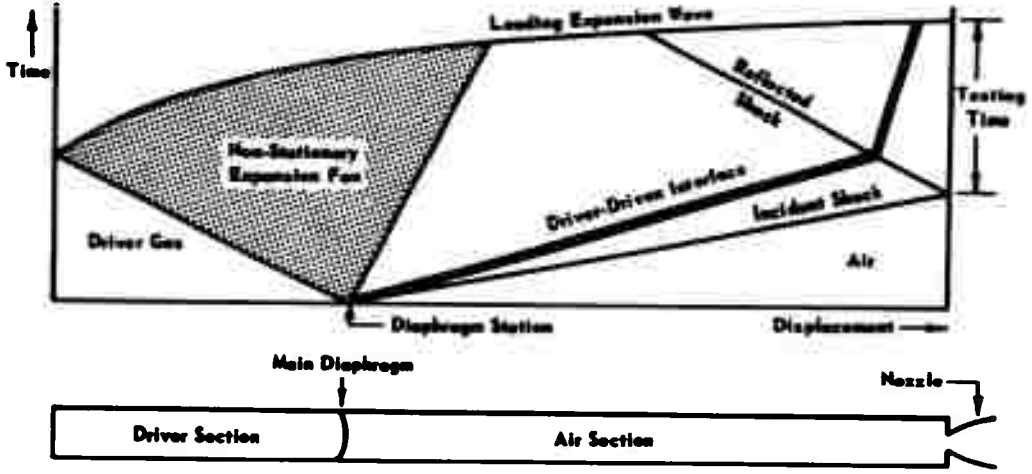

Figure 4 WAVE DIAGRAM FOR TAILORED-INTERFACE SCHOCK TUBE

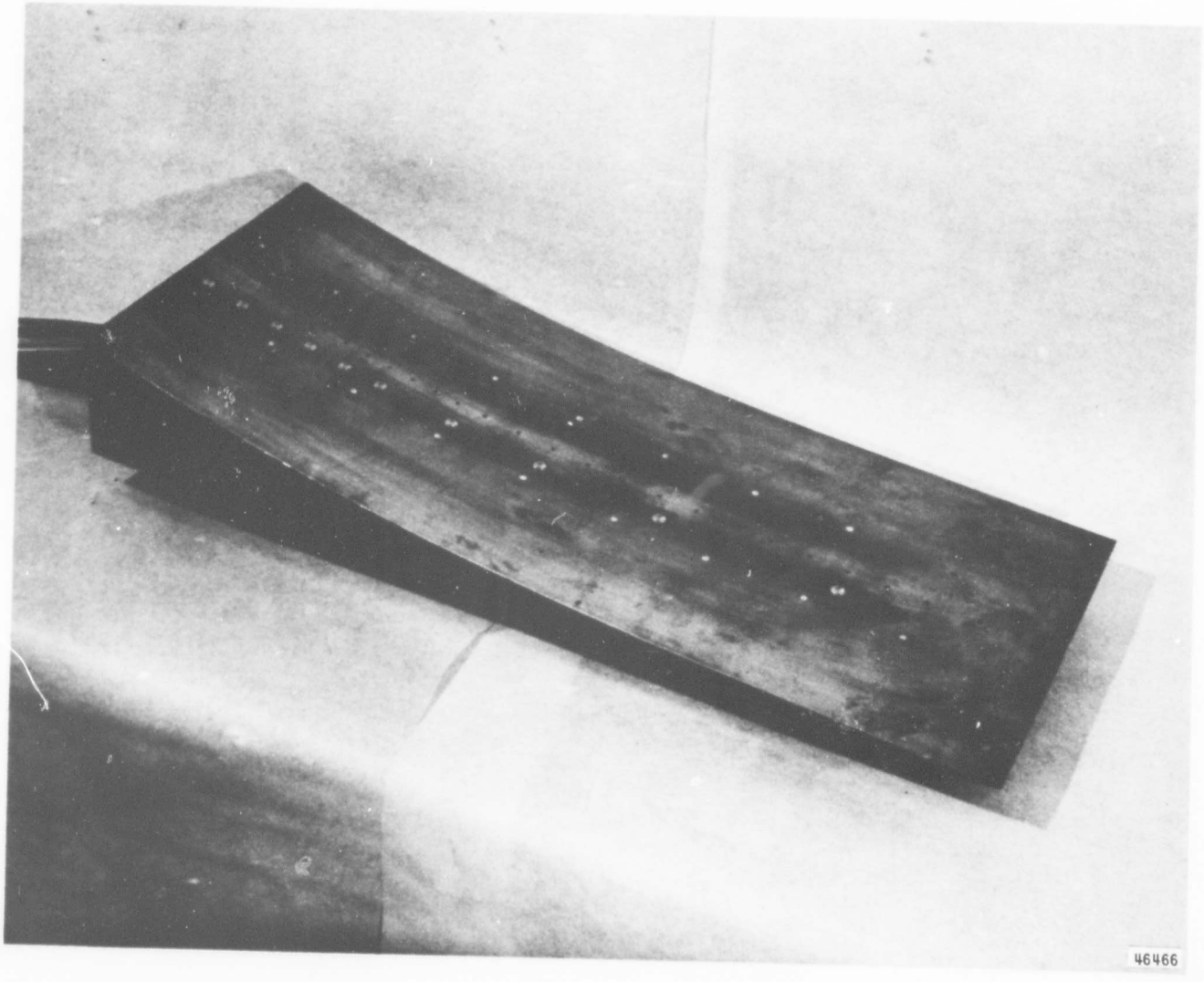

Figure 5 TWO-DIMENSIONAL MODEL, E-2

X	Y	X	Y
5.00	.262	17.00	1.491
5.50	.288	17.50	1.588
6.00	.314	18.00	1.689
6.50	.341	18.50	1.794
7.00	.369	19.00	1.903
7.50	.399	19.50	2.017
8.00	.431	20.00	2.136
8.50	.465	20.50	2.260
9.00	.501	21.00	2.389
9.50	.539	21.50	2.523
10.00	.579	22.00	2.662
10.50	.622	22.50	2.806
11.00	.668	23.00	2.955
11.50	.717	23.50	3.109
12.00	.768	24.00	3.267
12.50	.822		
13.00	.880		
13.50	.942		
14.00	1.008		
14.50	1.078		
15.00	1.152		
15.50	1.230		
16.00	1.312		
16.50	1.399		

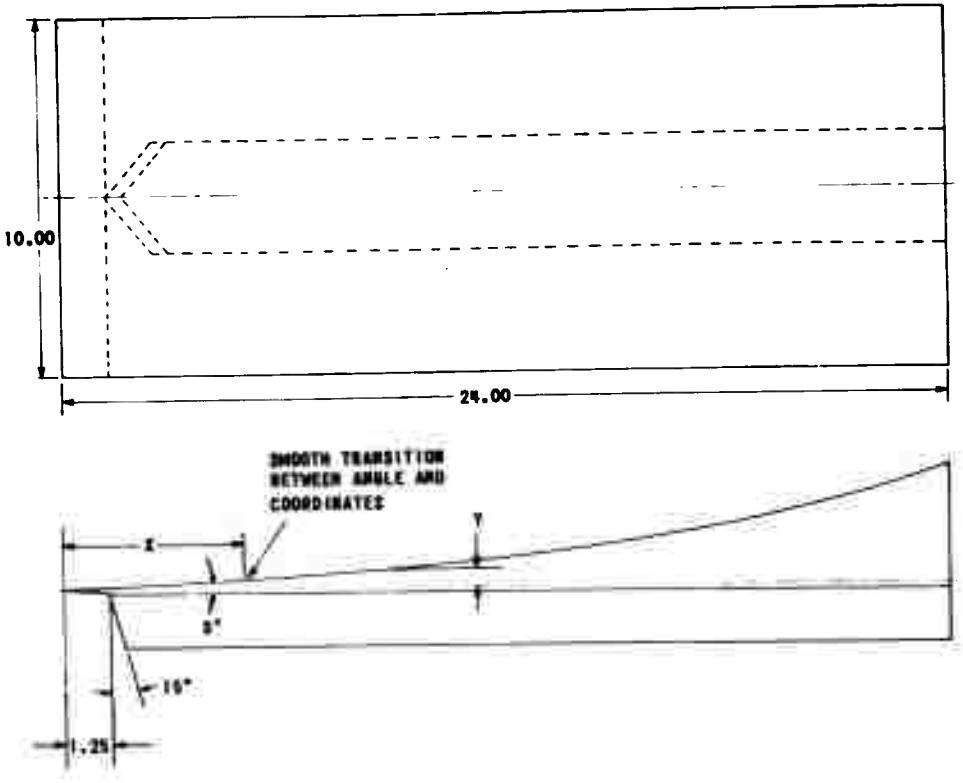

Figure 6 MODEL E-2 DIMENSIONS AND CONTOUR COORDINATES

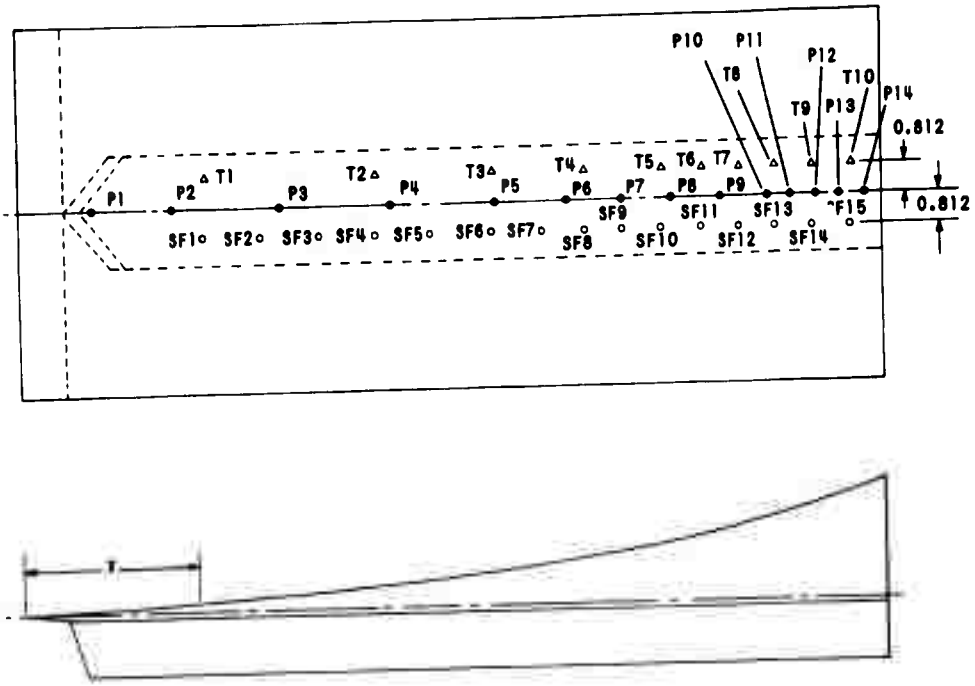

GAGE	X	GAGE	X	GAGE	X
T1	5.25	P1	2.00	SF1	5.25
T2	9.93	P2	4.31	SF2	6.81
T3	13.25	P3	7.31	SF3	8.37
T4	15.80	P4	10.31	SF4	9.93
T5	17.92	P5	13.31	SF5	11.49
T6	18.98	P6	15.30	SF6	13.25
T7	20.04	P7	16.76	SF7	14.69
T8	21.10	P8	18.12	SF8	15.80
T9	22.16	P9	19.48	SF9	16.86
T10	23.22	P10	20.84	SF10	17.92
		P11	21.52	SF11	18.98
		P12	22.20	SF12	20.04
		P13	22.88	SF13	21.10
		P14	23.56	SF14	22.16
				SF15	23.22

Figure 7 MODEL E-2 INSTRUMENTATION LOCATIONS

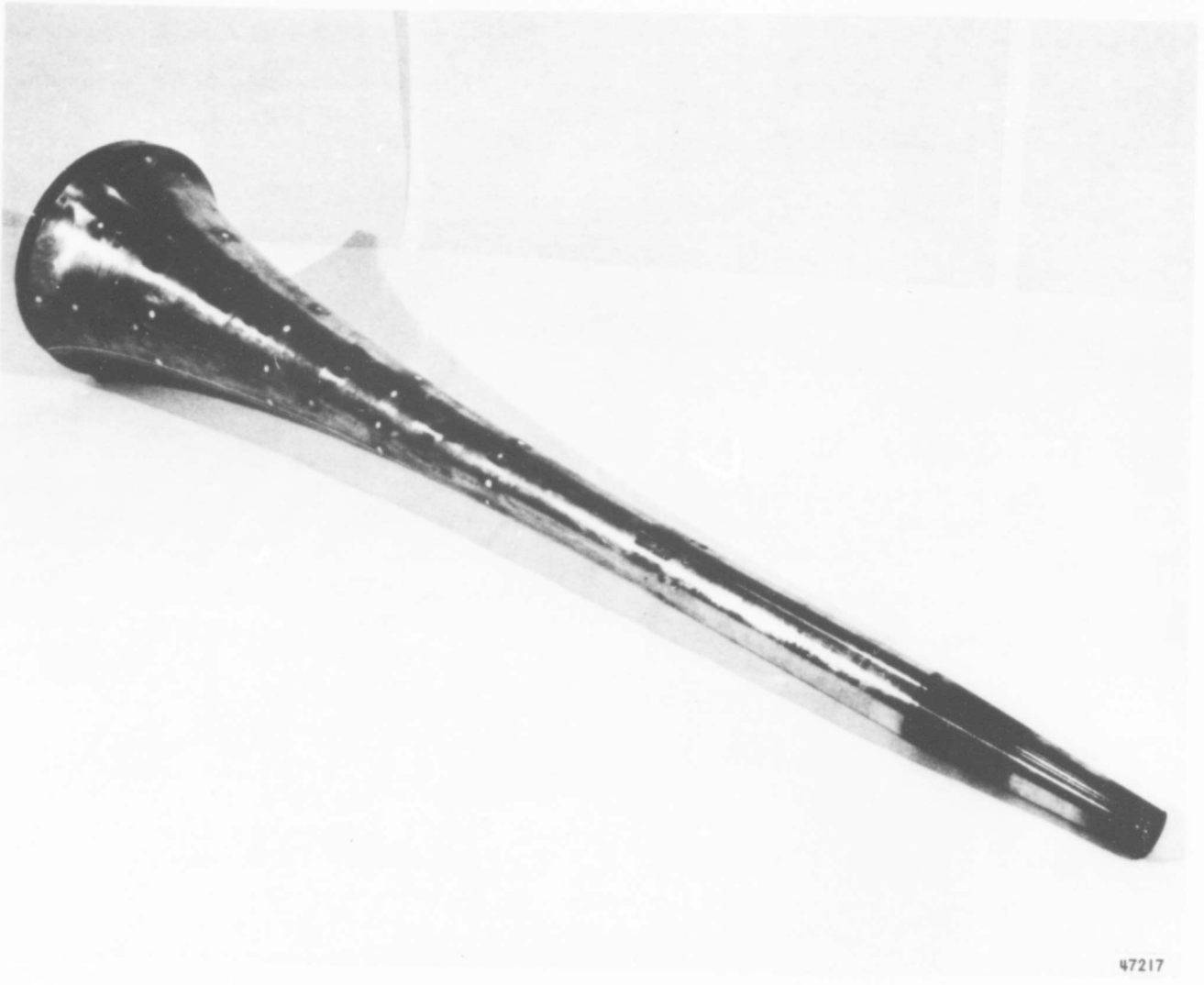

Figure 8 AXISYMMETRIC MODEL

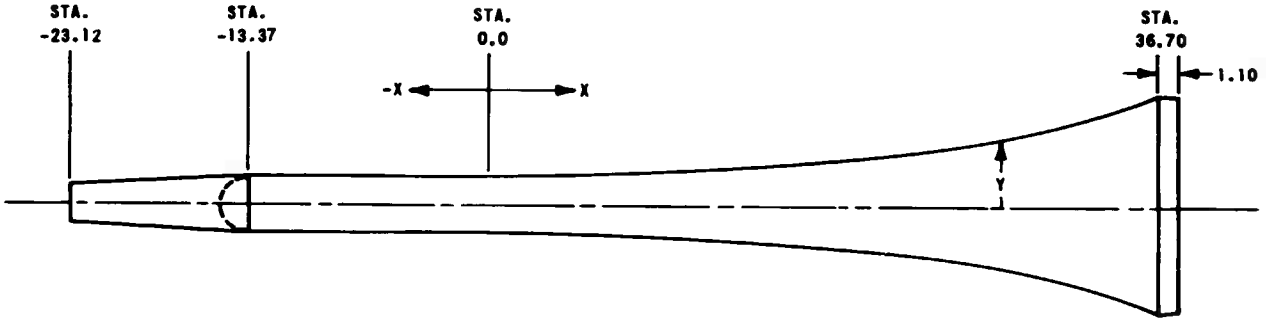

X	Y	X	Y	X	Y	X	Y
-23.12	.949	20.677	2.514	28.188	3.516	32.490	4.411
-13.37	1.500	21.396	2.590	28.510	3.571	33.100	4.576
0.0	1.500	22.072	2.665	29.109	3.679	33.508	4.693
5.709	1.575	23.316	2.810	29.653	3.781	34.012	4.851
10.381	1.737	24.426	2.952	30.148	3.880	34.588	5.050
13.008	1.890	25.420	3.087	30.601	3.973	35.082	5.245
15.307	2.043	26.316	3.217	31.015	4.062	35.560	5.467
17.326	2.200	27.121	3.340	31.570	4.186	36.004	5.724
19.105	2.359	27.495	3.400	32.059	4.303	36.750	6.188

Figure 9 AXISYMMETRIC MODEL COORDINATES

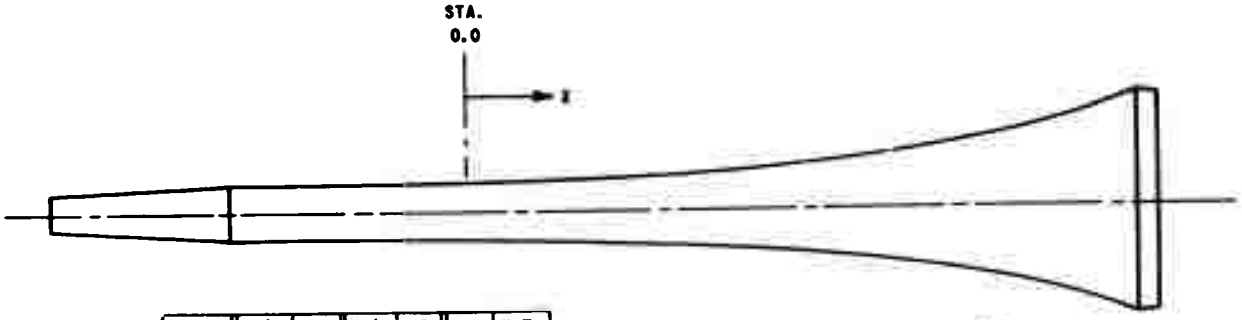

X	ϕ	S.F.	ϕ	P	ϕ	N.T.
0	0	1	-60	1	+60	1
13.0	0	3	-60	3		
19.0	0	4	+60	4		
20.0					-60	2
24.0	0	5	-60	5		
25.0					+60	3
27.0	0	6	+60	6		
29.0	0	7	-60	7		
31.0	0	8	+60	8	-60	4
33.0	0	9	-60	9	+60	5
33.5	-10	16	+50	15		
34.0	0	10				
34.5	-10	11	+60	10	-60	6
35.0	0	12				
35.25			-49	11	+60	7
35.5	-10	13				
35.6			+50	12	-39	8
36.0	0	14	-29	13	+40	9
36.25					-60	10
36.5	-10	15	+60	14		

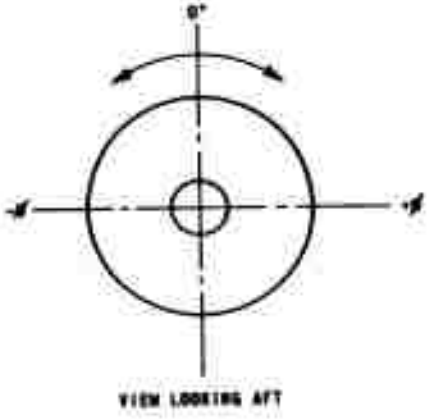

Figure 10 AXISYMMETRIC MODEL INSTRUMENTATION LOCATIONS

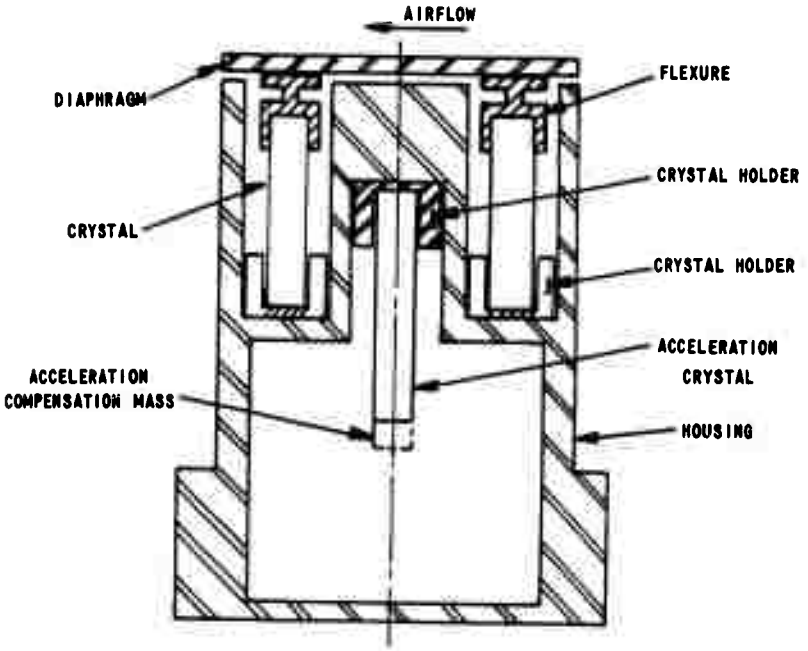

Figure 11 DRAWING OF SKIN FRICTION GAGE 25-38 AC

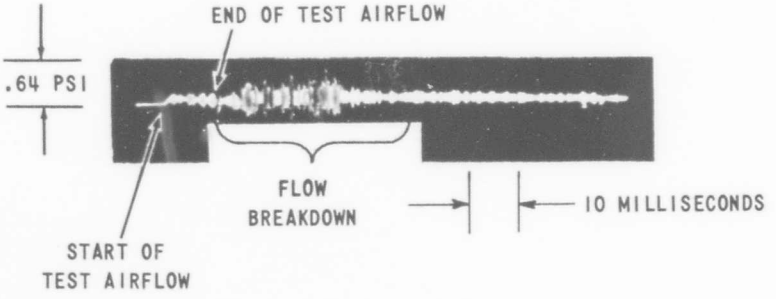

Figure 12 TYPICAL SKIN FRICTION AND HEAT TRANSFER GAGE RESPONSES
(a) TUNNEL FLOW BREAKDOWN - RUN 2

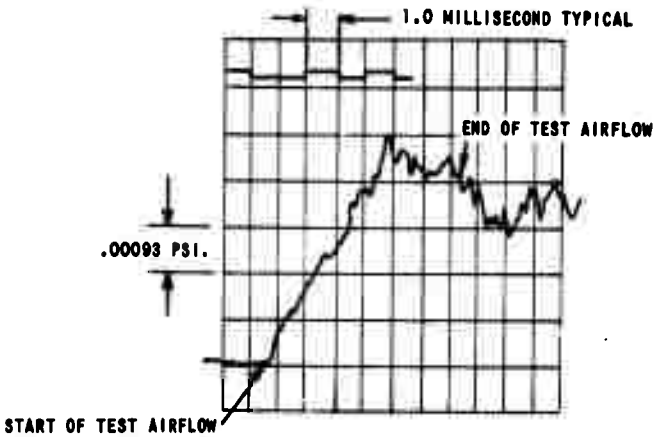

SKIN FRICTION POSITION 1

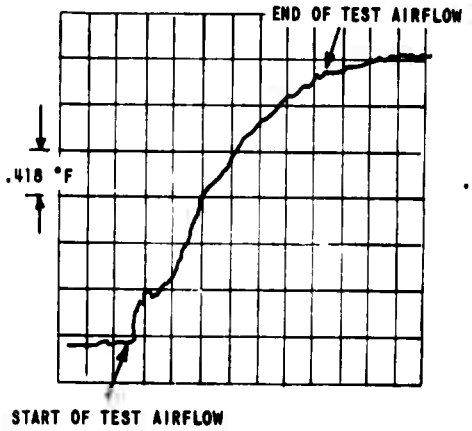

TEMPERATURE HISTORY FOR POSITION 1

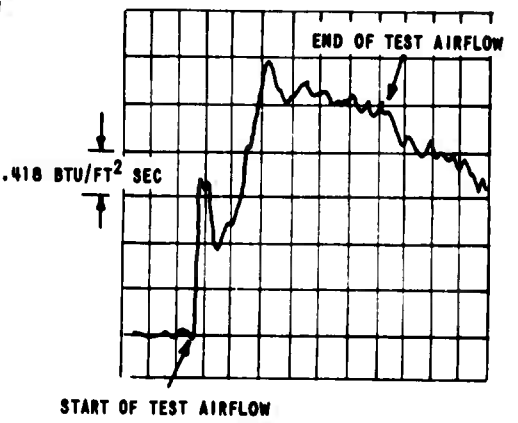

ANALOG CIRCUIT OUTPUT USING TEMPERATURE TRACE ON LEFT AS INPUT

Figure 12 (CONTINUED) (b) LAMINAR BOUNDARY LAYER - RUN 1

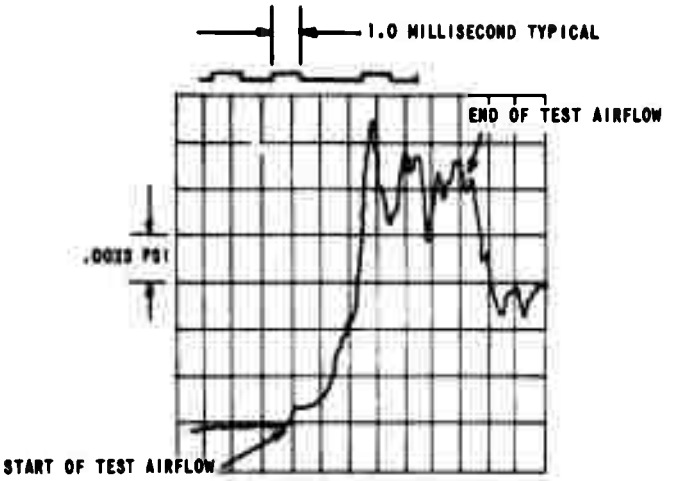

SKIN FRICTION POSITION 4

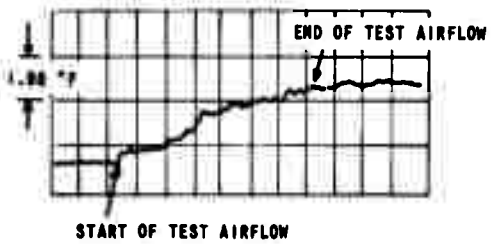

TEMPERATURE HISTORY FOR POSITION 2

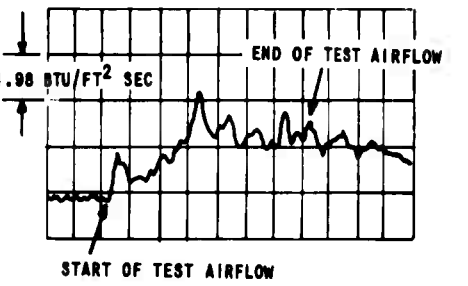

ANALOG CIRCUIT OUTPUT USING TEMPERATURE TRACE ON LEFT AS INPUT

Figure 12 (CONTINUED) (c) TRANSITIONAL BOUNDARY LAYER - RUN 1

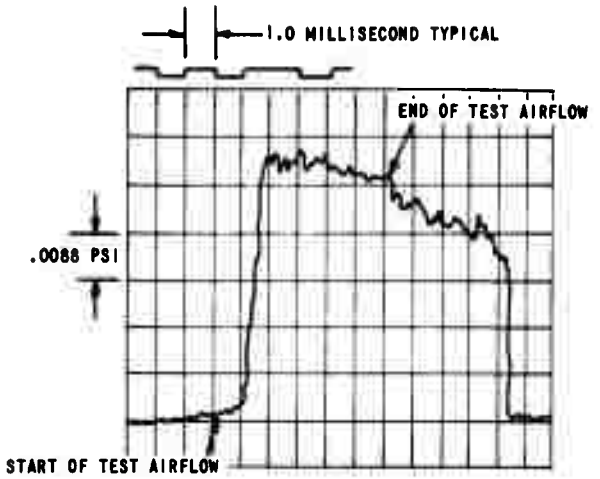

SKIN FRICTION POSITION 8

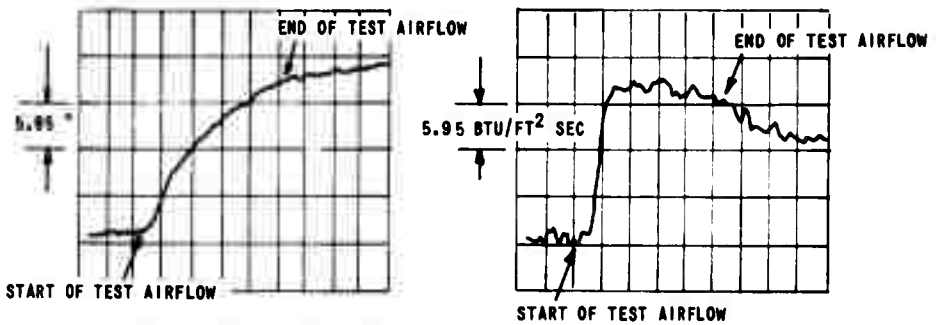

TEMPERATURE HISTORY FOR POSITION 4

ANALOG CIRCUIT OUTPUT USING TEMPERATURE TRACE ON LEFT AS INPUT

Figure 12 (CONCLUDED) (d) TURBULENT BOUNDARY LAYER - RUN 1

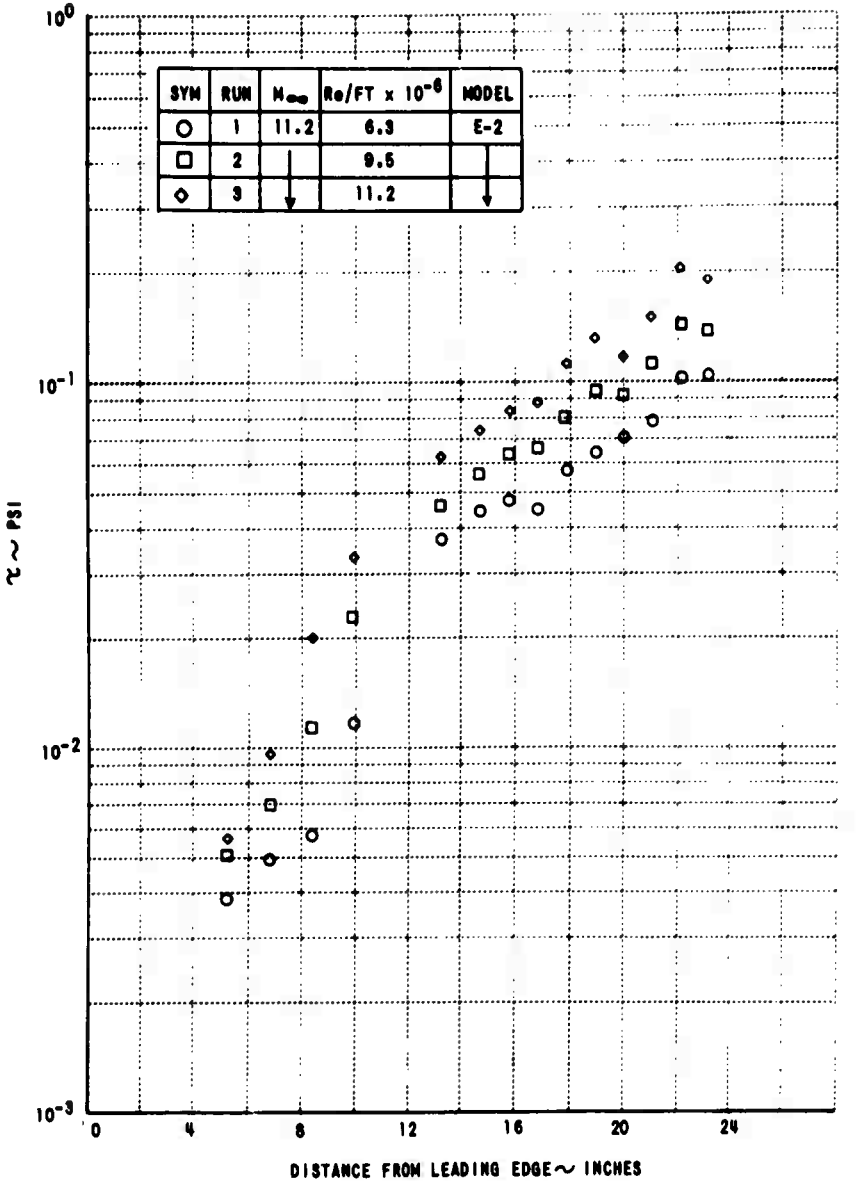

Figure 13 SKIN FRICTION DISTRIBUTIONS ON THE TWO-DIMENSIONAL MODEL
(a) MACH NUMBER 11, ANGLE OF ATTACK = 0°

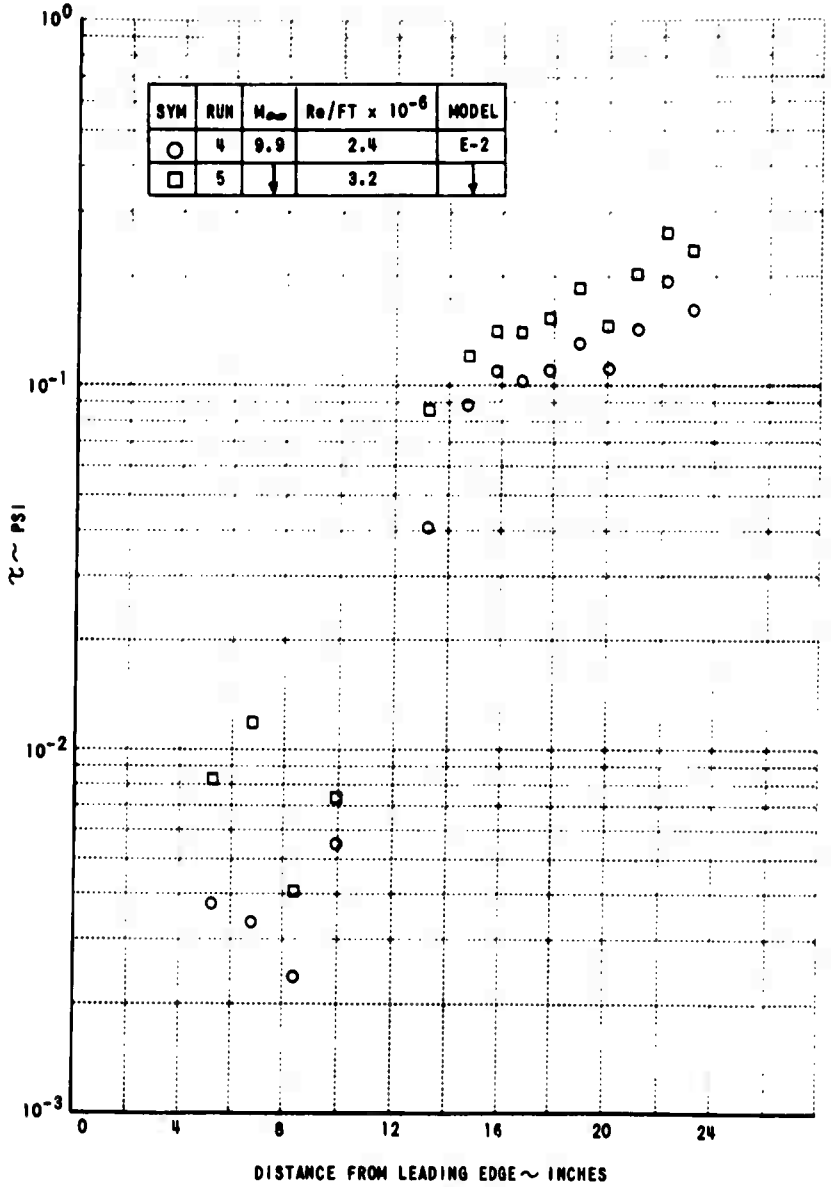

Figure 13 (CONTINUED) (b) MACH NUMBER 10, ANGLE OF ATTACK = 0°

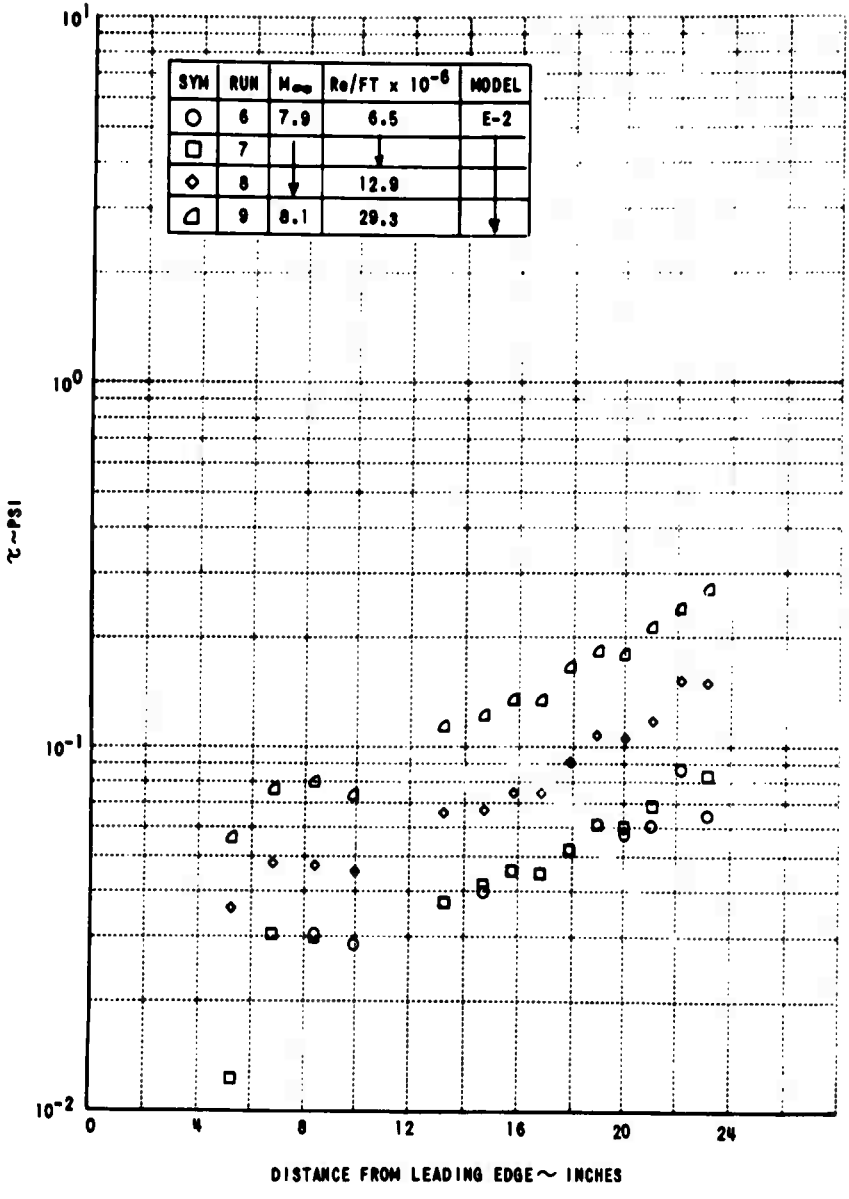

Figure 13 (CONTINUED) (c) MACH NUMBER 8, ANGLE OF ATTACK = 0°

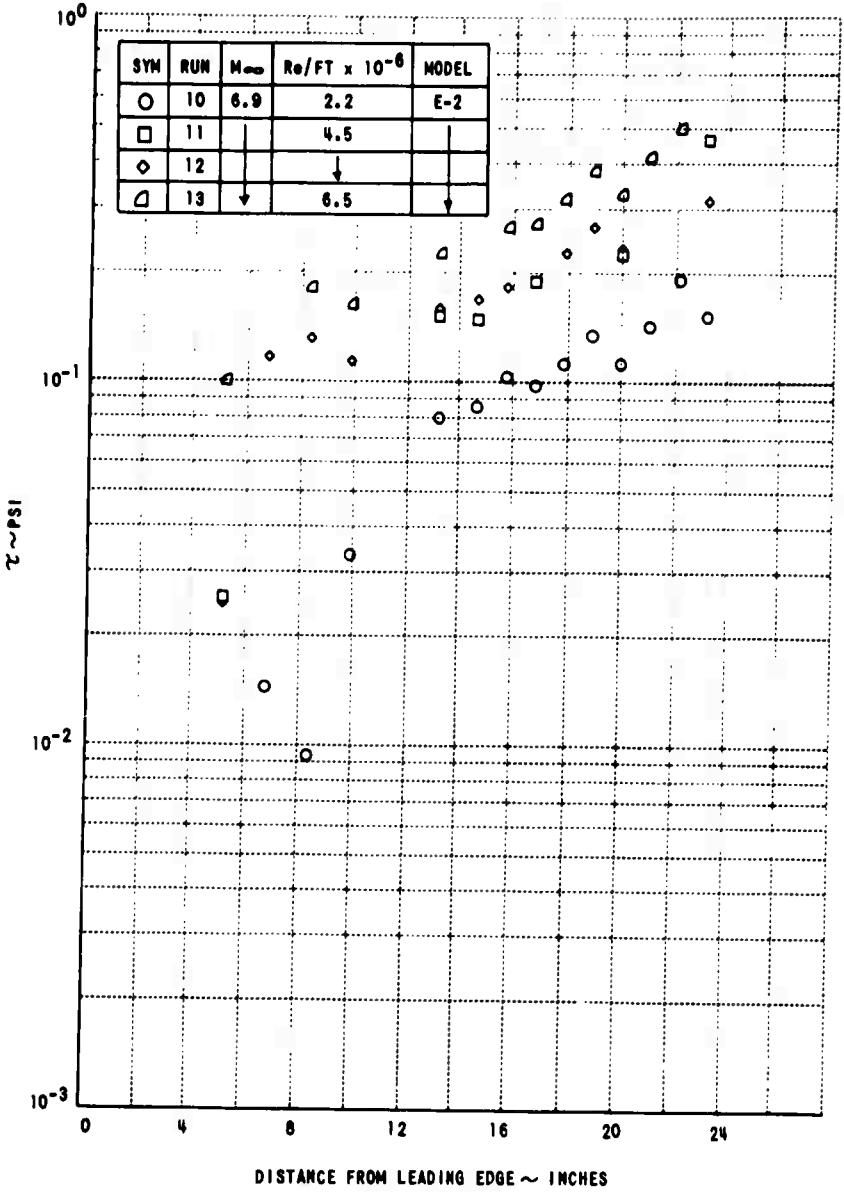

Figure 13 (CONTINUED) (d) MACH NUMBER 7, ANGLE OF ATTACK = 0°

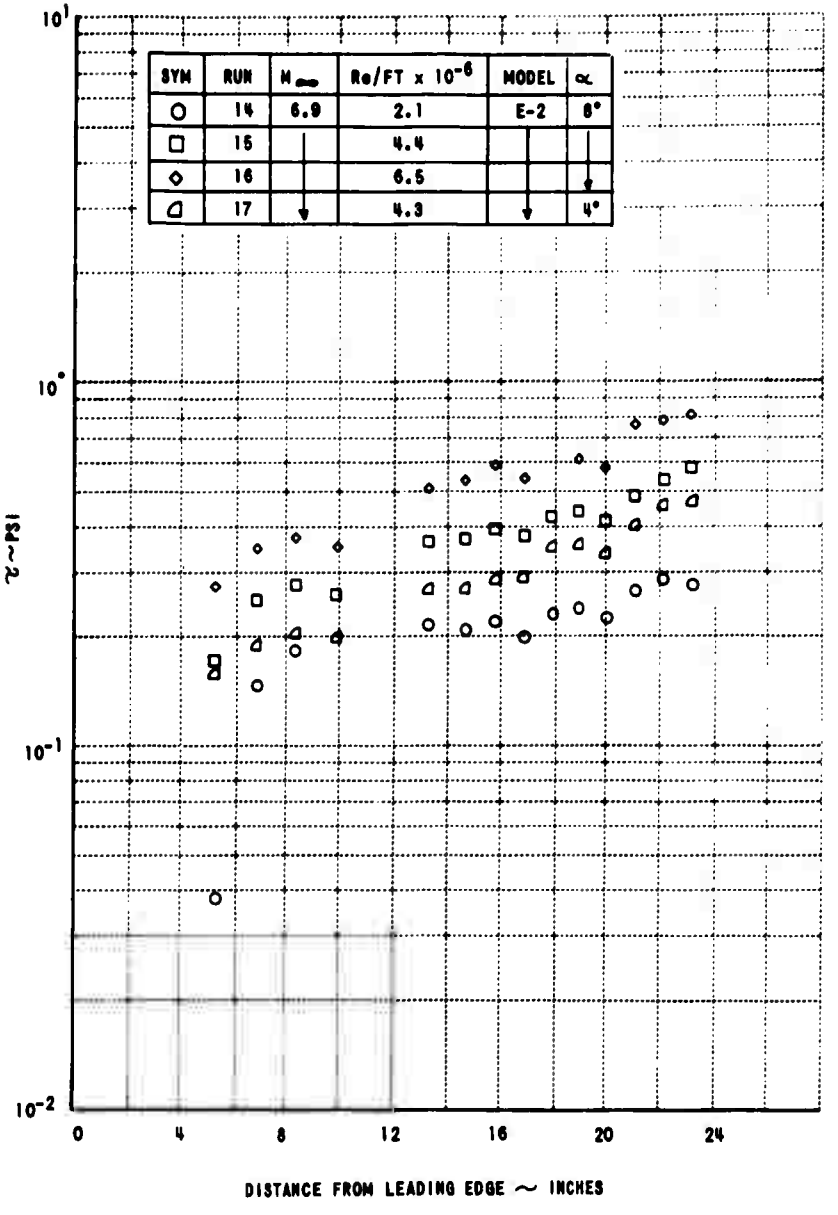

Figure 13 (CONCLUDED) (e) MACH NUMBER 7, ANGLE OF ATTACK = 4°, 8°

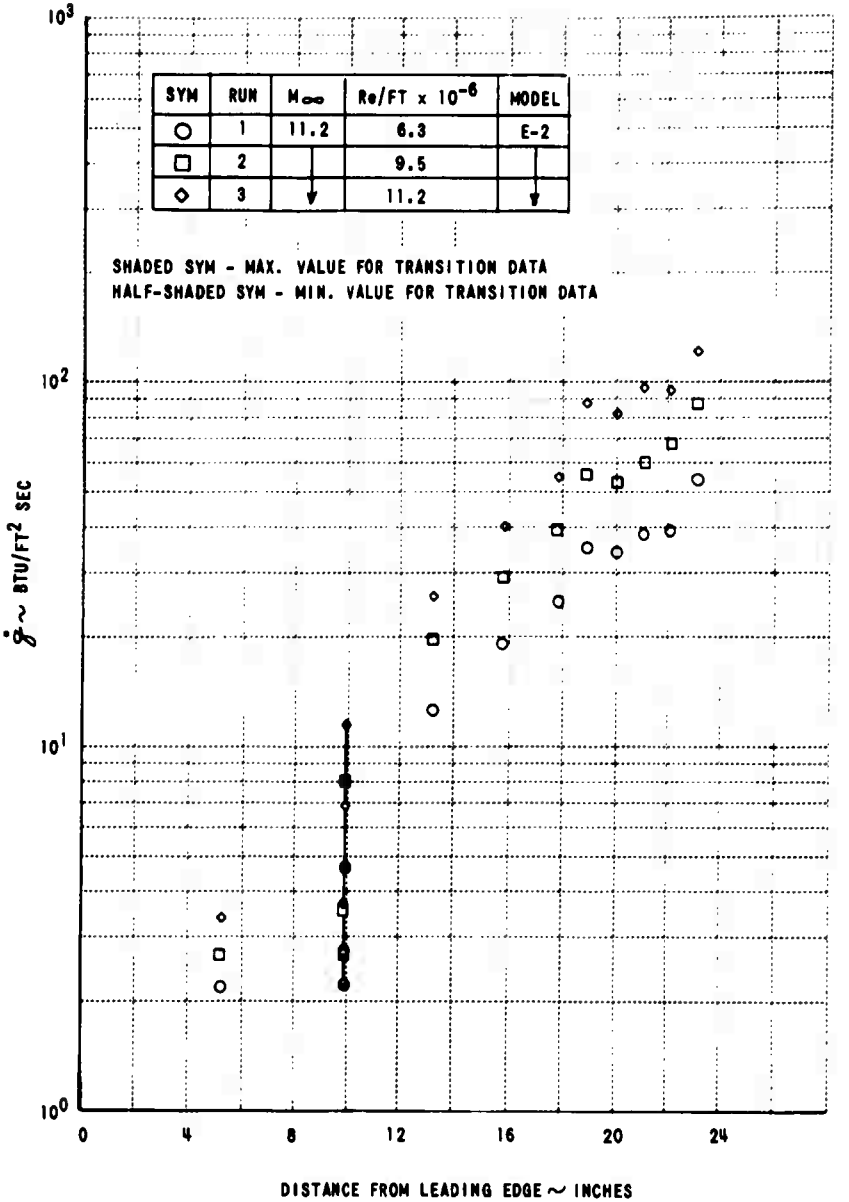

Figure 14 HEAT TRANSFER DISTRIBUTIONS ON THE TWO-DIMENSIONAL MODEL
(a) MACH NUMBER 11, ANGLE OF ATTACK = 0°

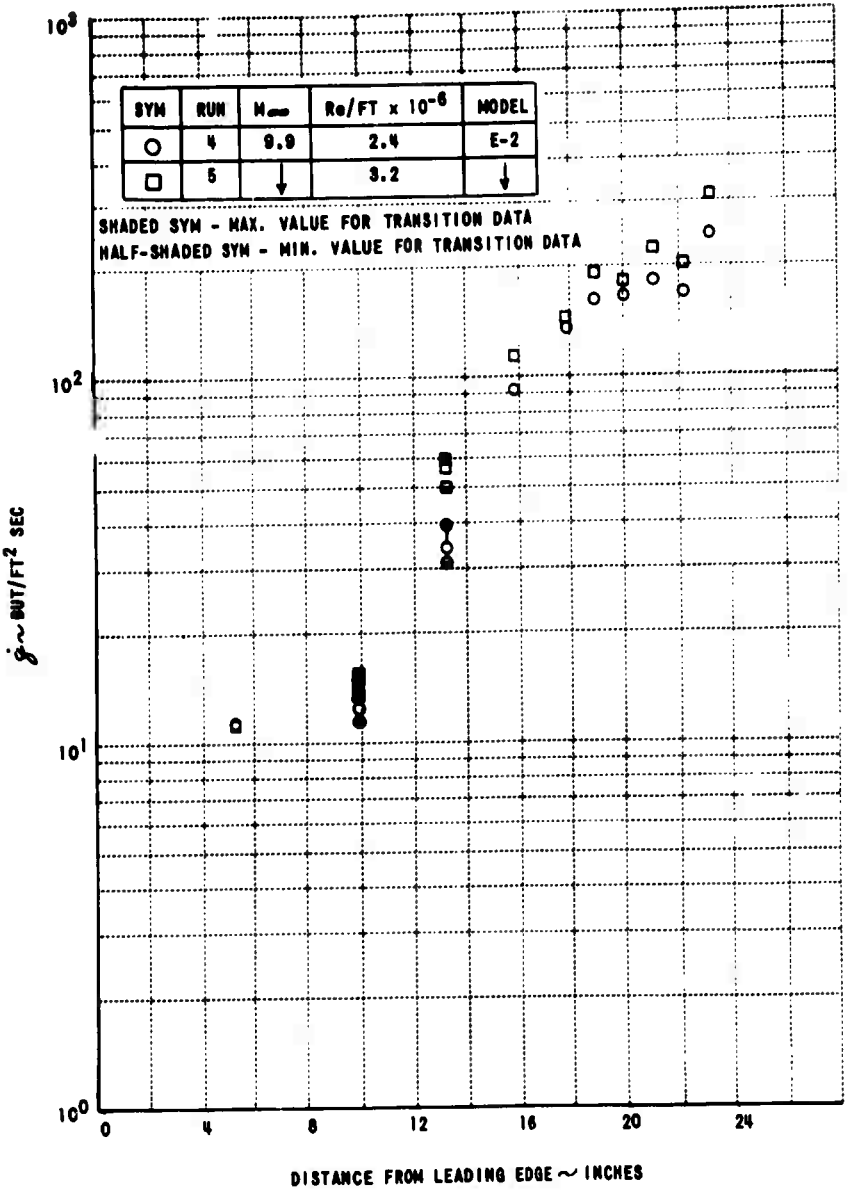

Figure 14 (CONTINUED) (b) MACH NUMBER 10, ANGLE OF ATTACK = 0°

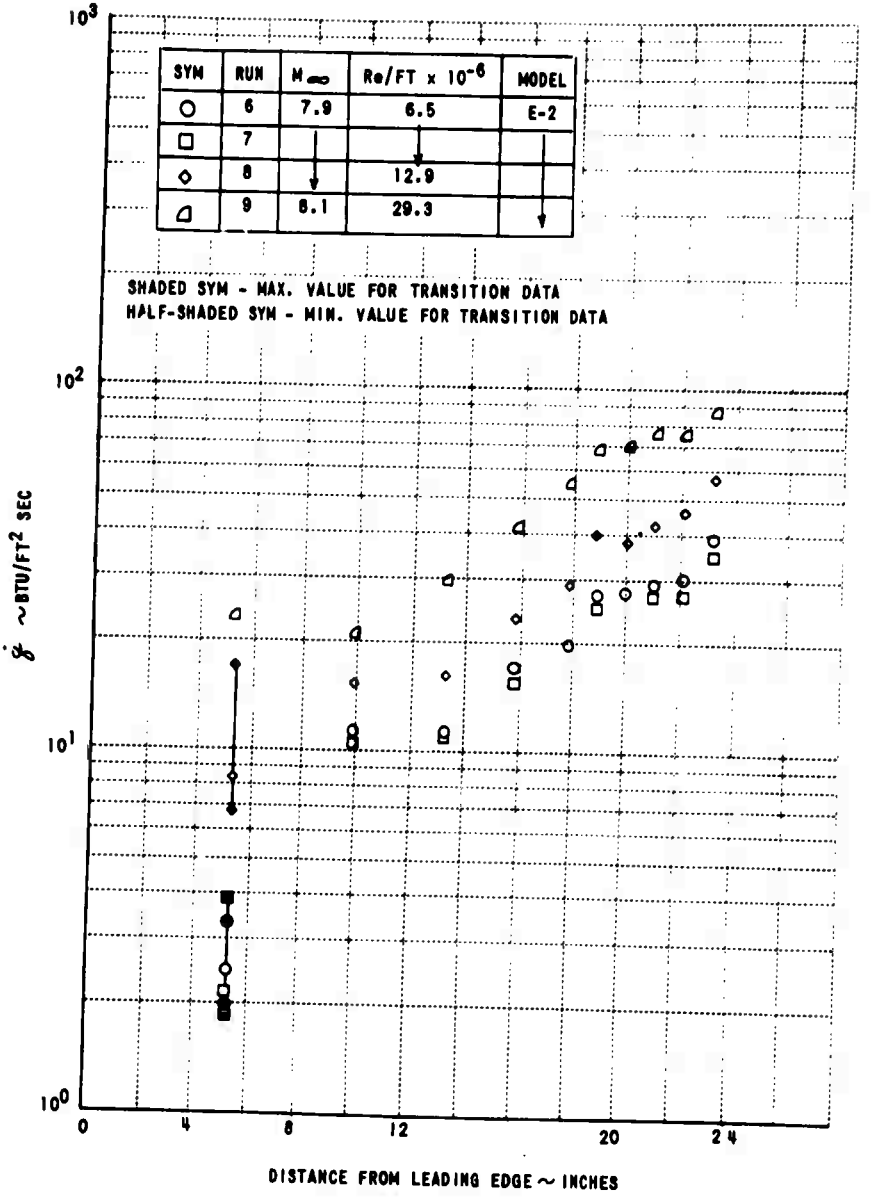

Figure 14 (CONTINUED) (c) MACH NUMBER 8, ANGLE OF ATTACK = 0°

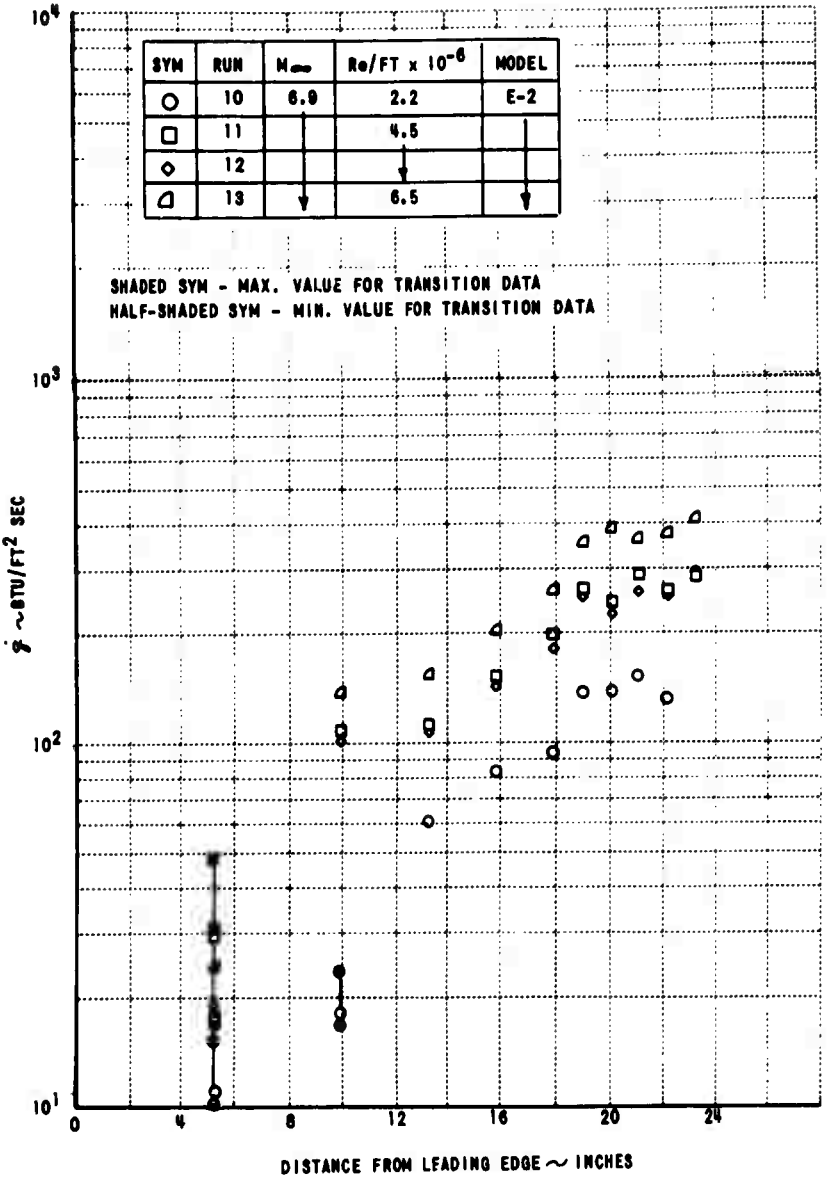

Figure 14 (CONTINUED) (d) MACH NUMBER 7, ANGLE OF ATTACK = 0°

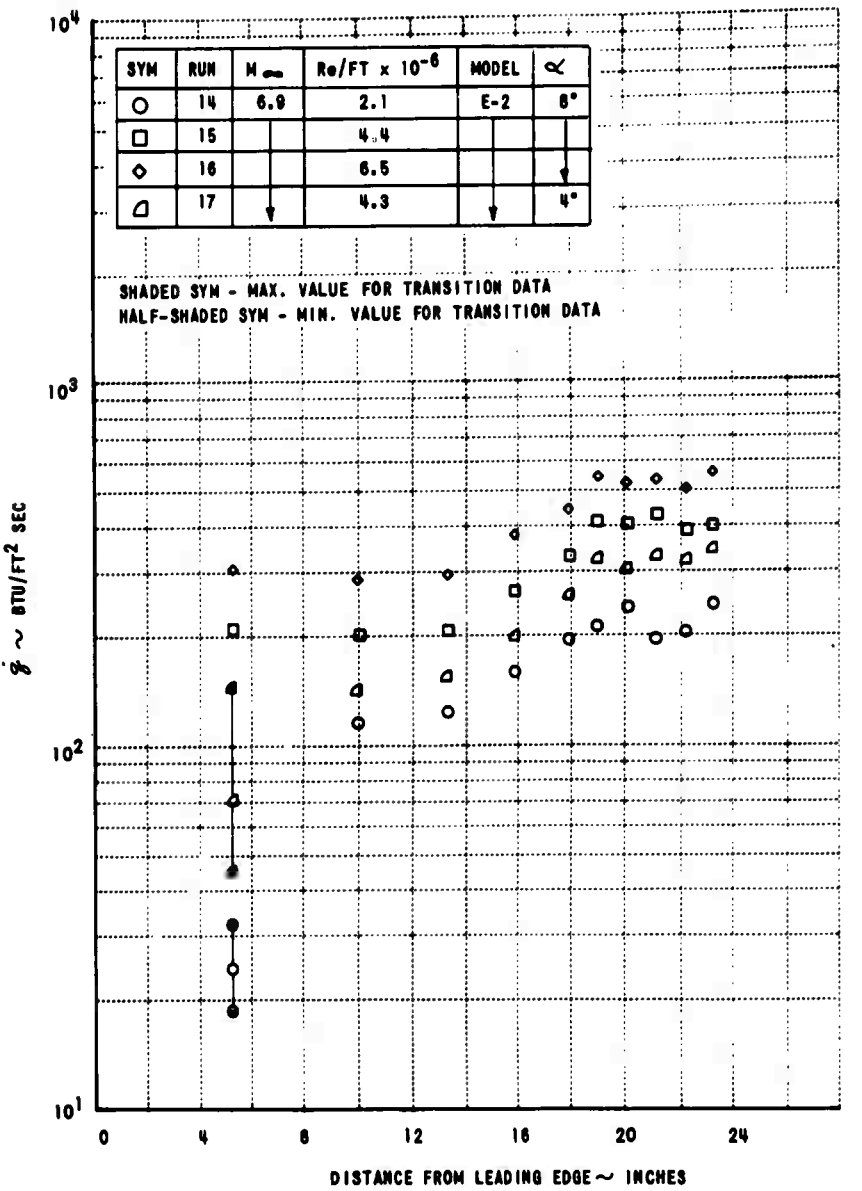

Figure 14 (CONCLUDED) (e) MACH NUMBER 7, ANGLE OF ATTACK = 4°, 8°

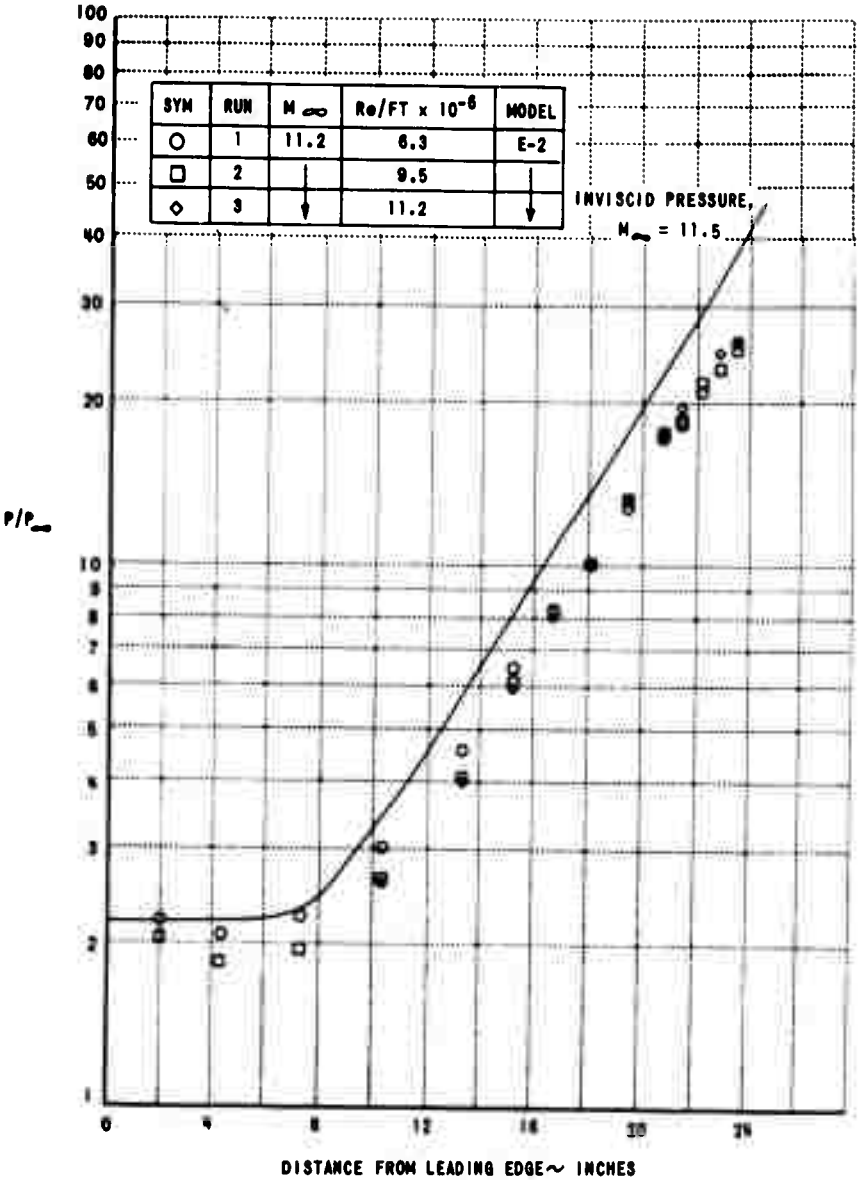

Figure 15 PRESSURE DISTRIBUTIONS ON THE TWO-DIMENSIONAL MODEL
(a) MACH NUMBER 11, ANGLE OF ATTACK = 0°

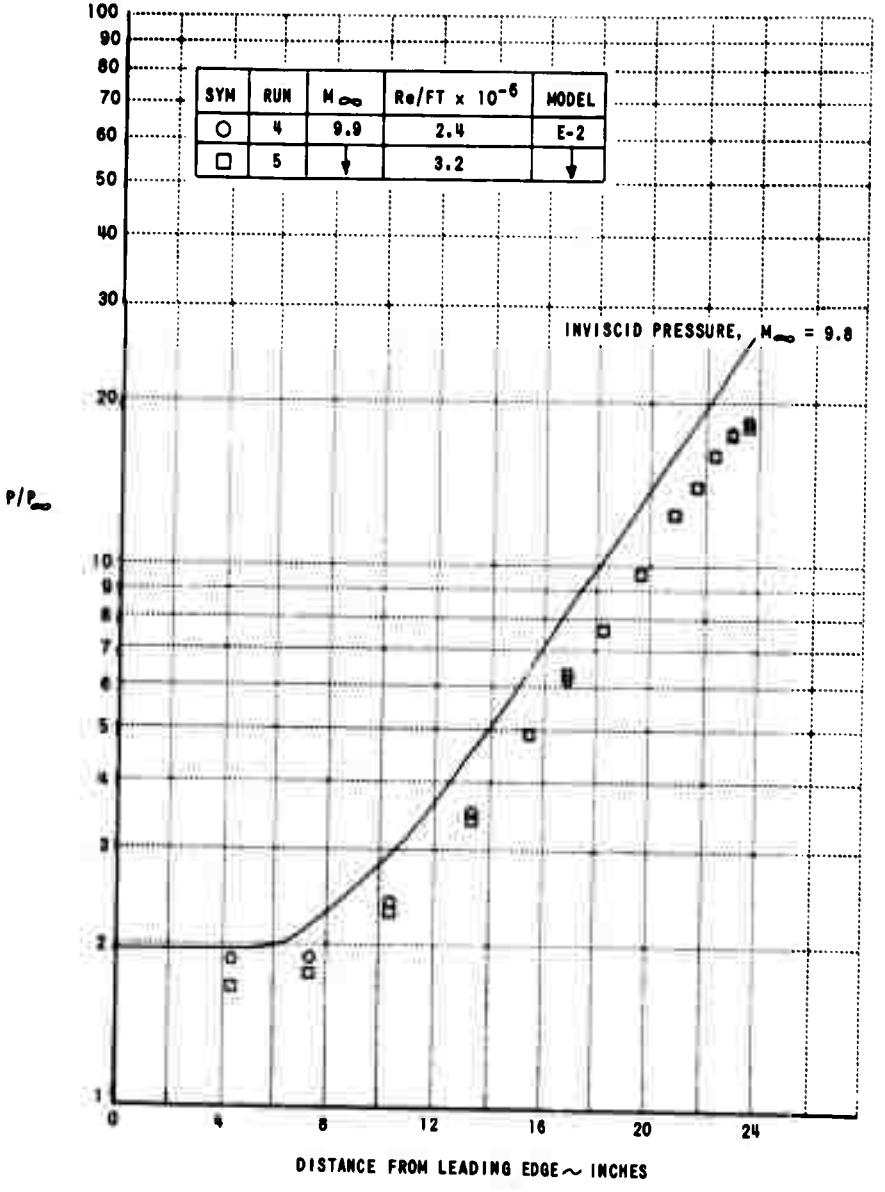

Figure 15 (CONTINUED) (b) MACH NUMBER 10, ANGLE OF ATTACK = 0°

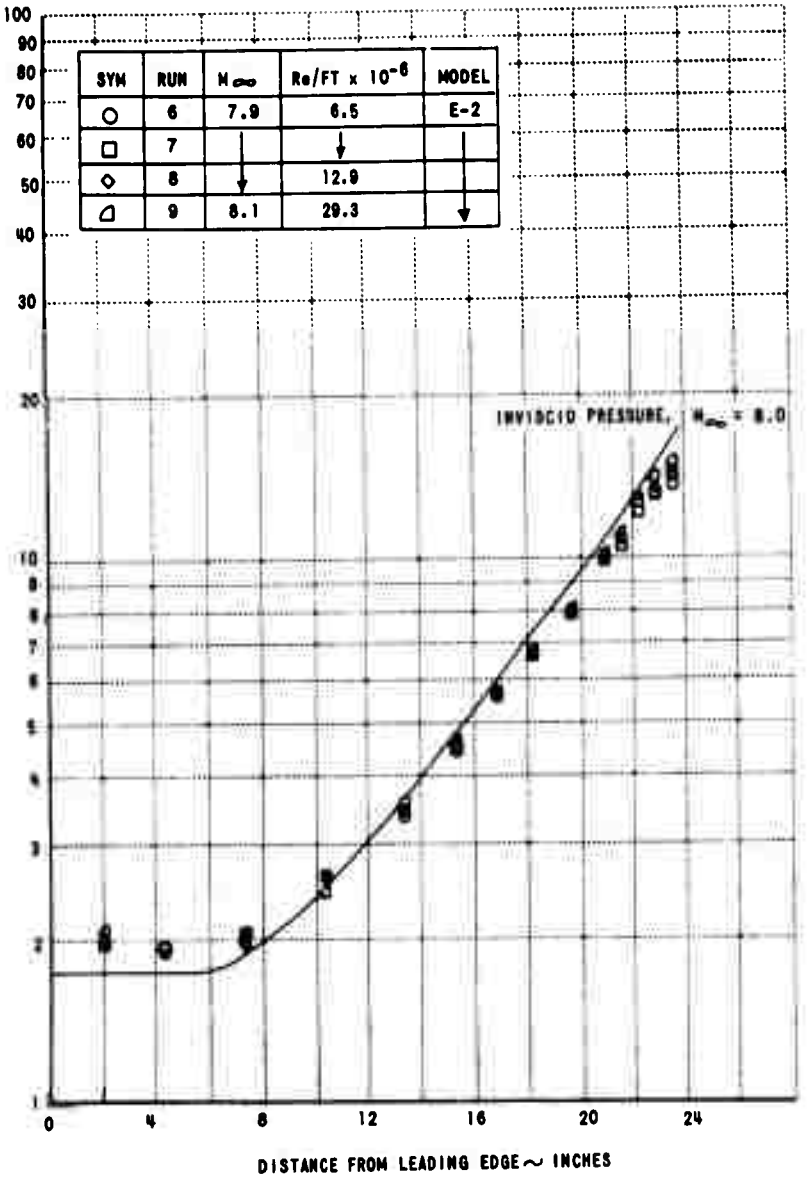

Figure 15 (CONTINUED) (c) MACH NUMBER 8, ANGLE OF ATTACK = 0°

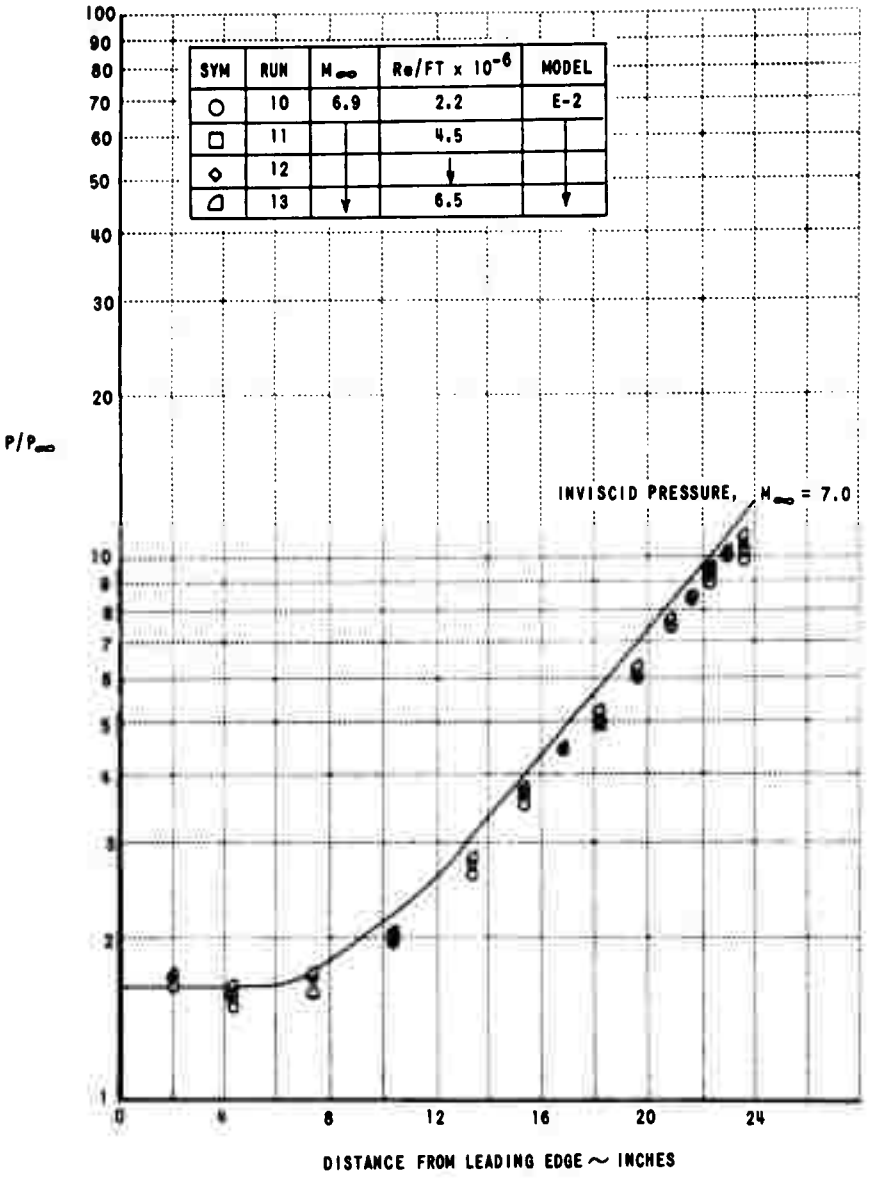

Figure 15 (CONTINUED) (d) MACH NUMBER 7, ANGLE OF ATTACK = 0°

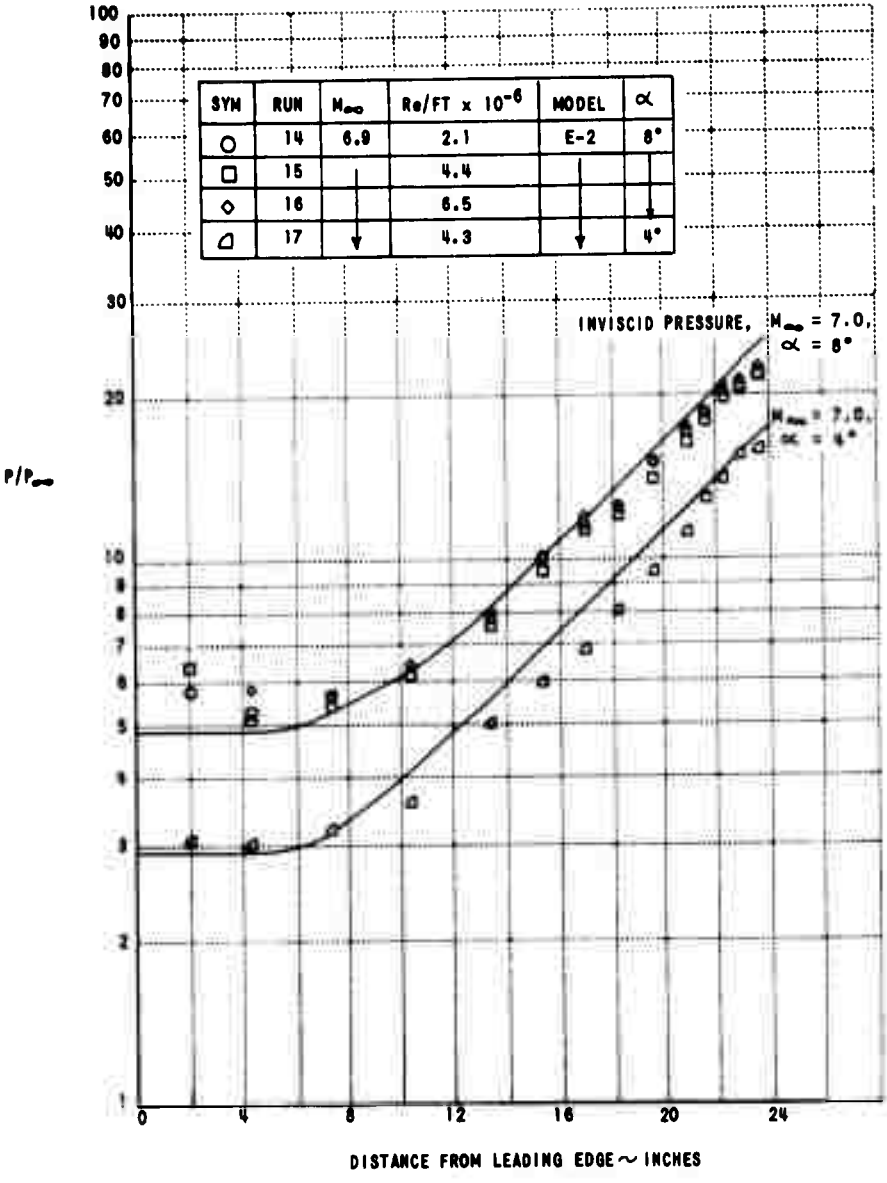

Figure 15 (CONCLUDED) (e) MACH NUMBER 7, ANGLE OF ATTACK = 4°, 8°

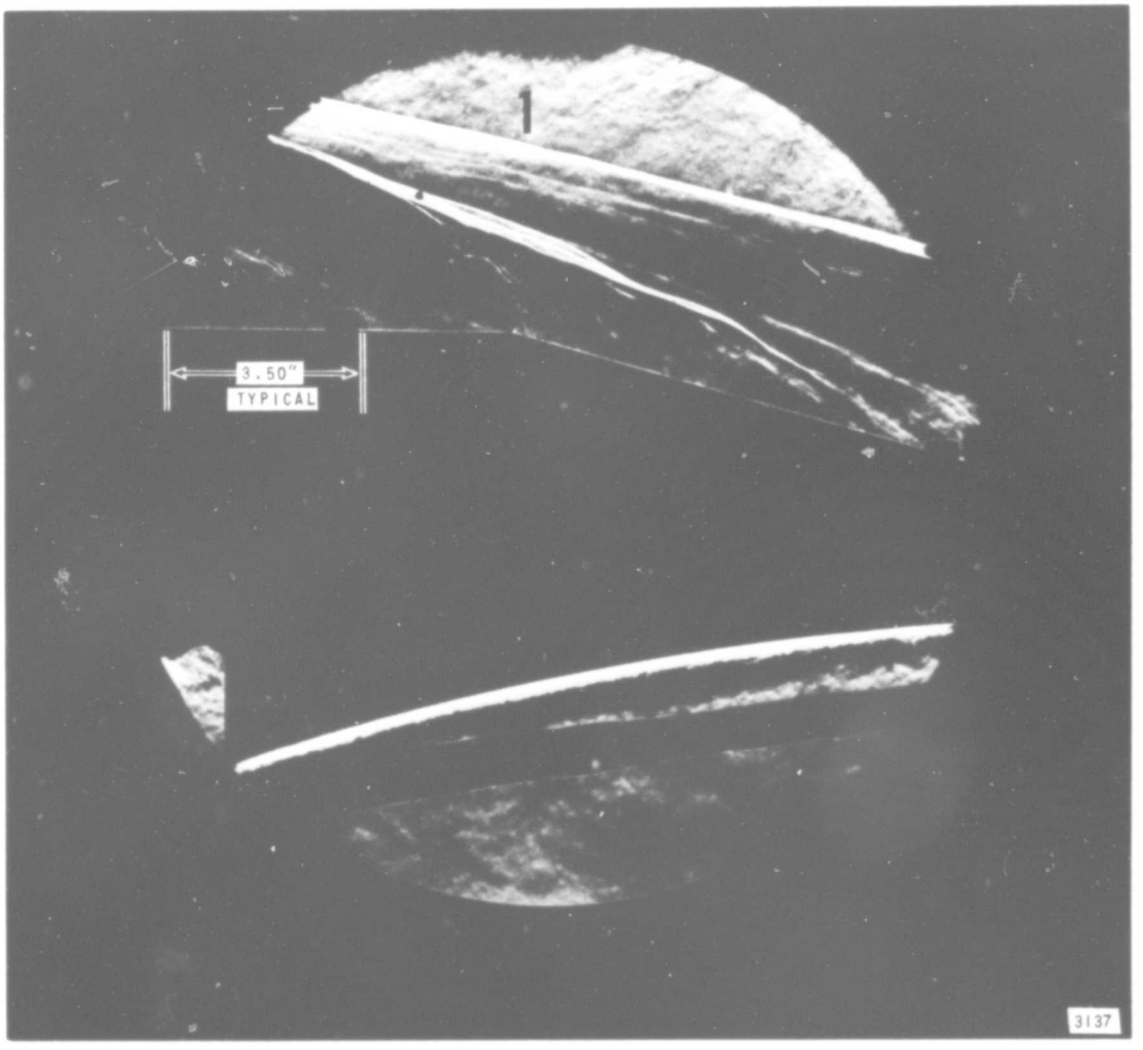

Figure 16 TWO-DIMENSIONAL MODEL FLOW PHOTOGRAPHS
(a) MODEL E-2 SCHLIEREN, RUN 1

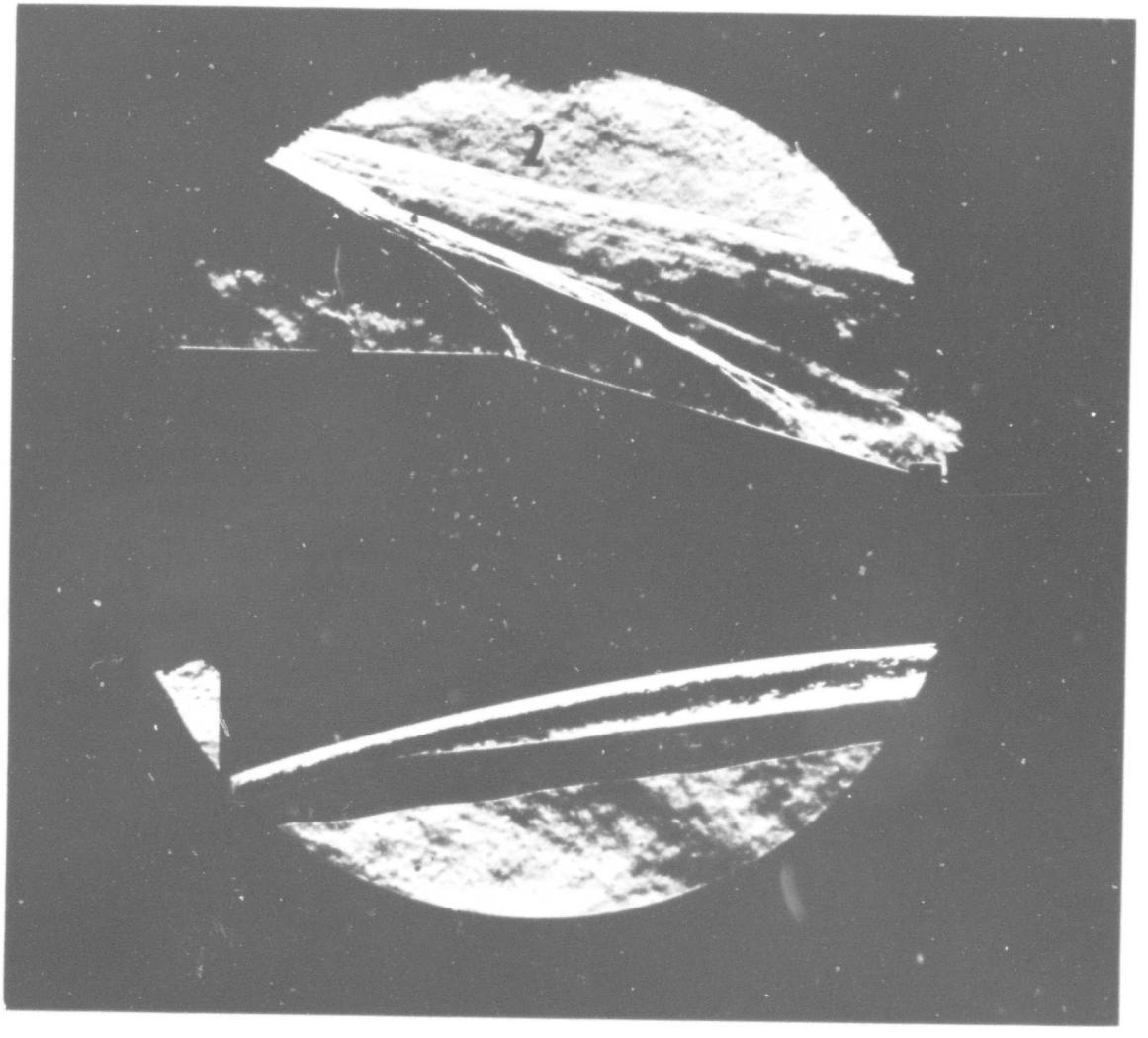

Figure 16 (CONTINUED) (b) MODEL E-2 SCHLIEREN, RUN 2

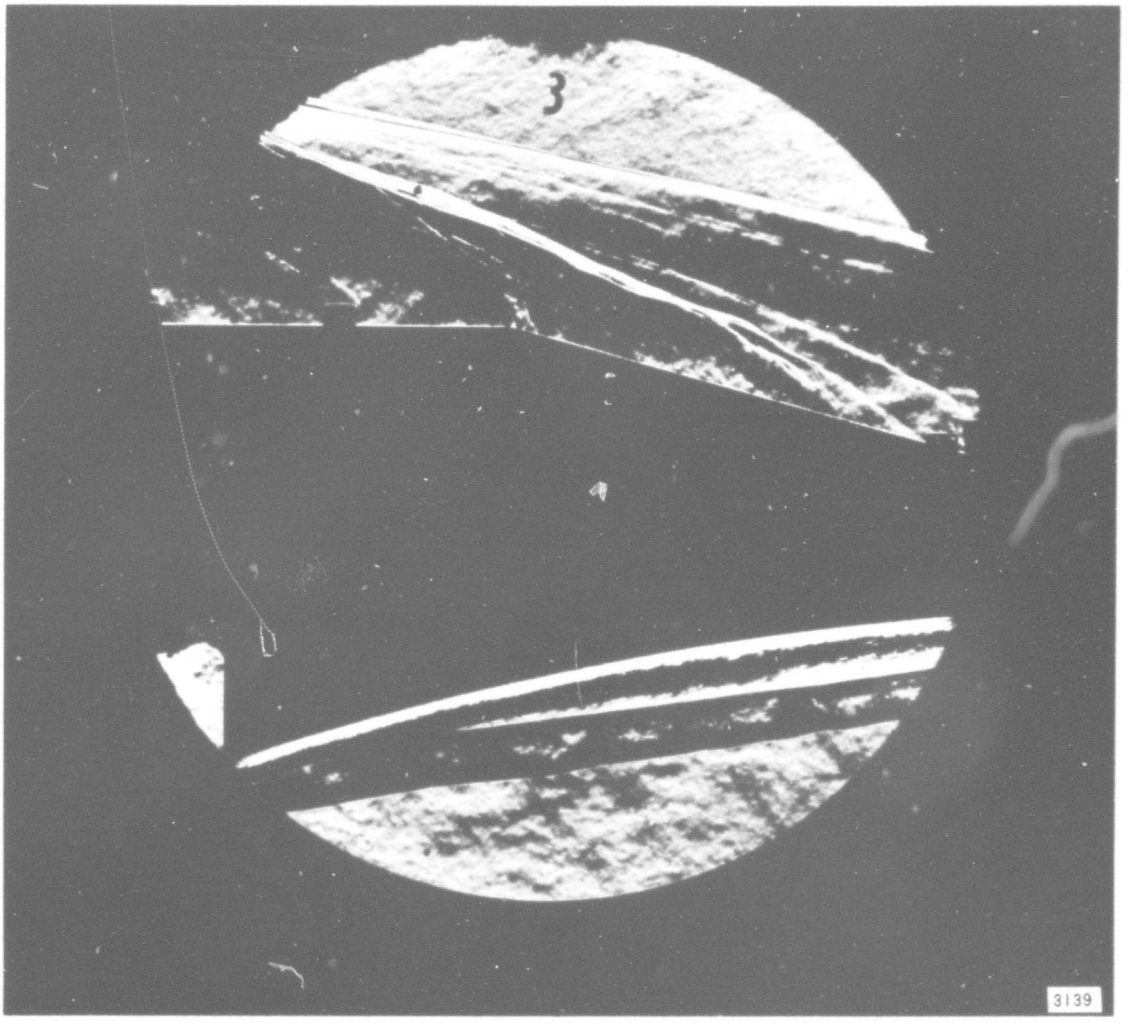

Figure 16 (CONTINUED) (c) MODEL E-2 SCHLIEREN, RUN 3

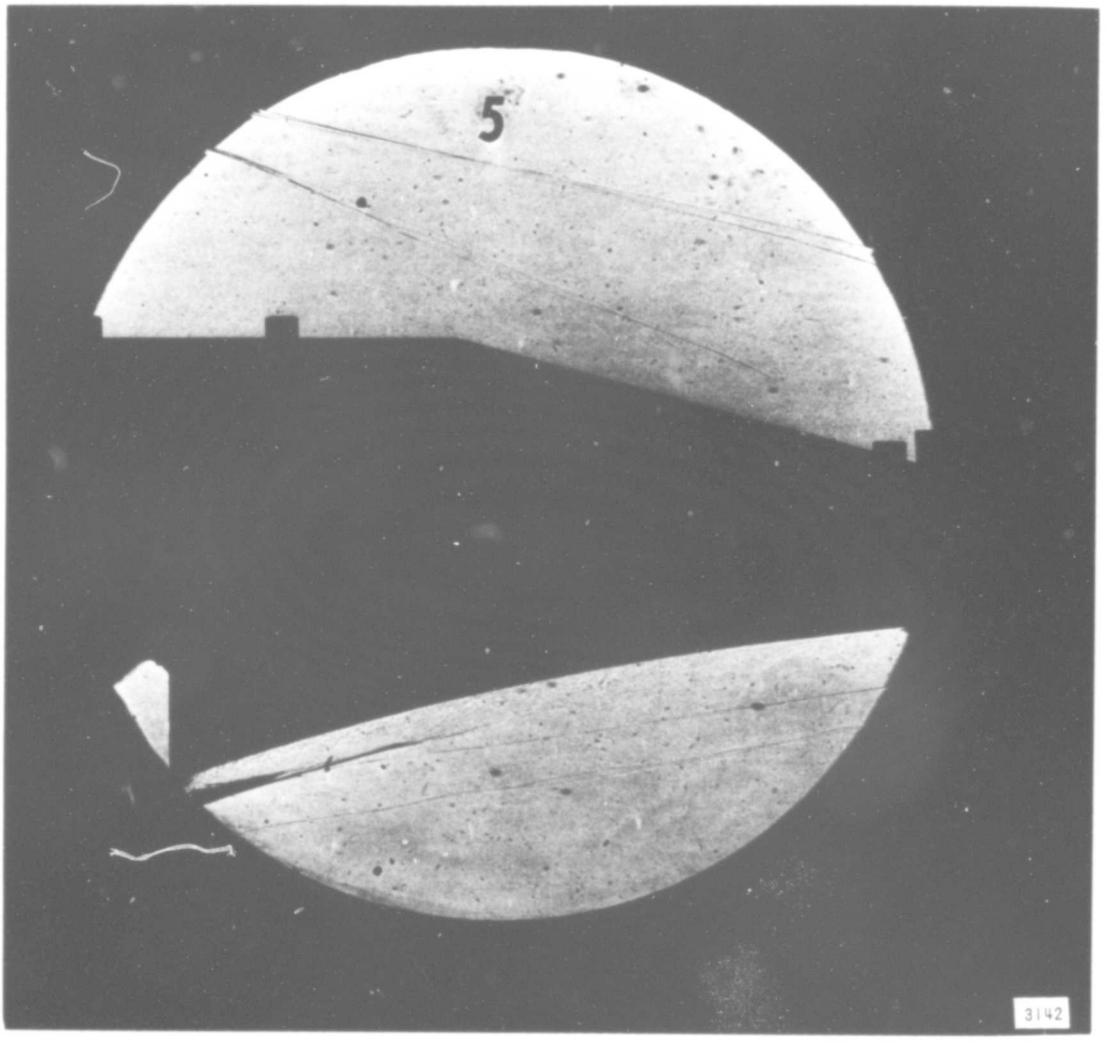

Figure 16 (CONTINUED) (d) MODEL E-2 SHADOWGRAPH, RUN 5

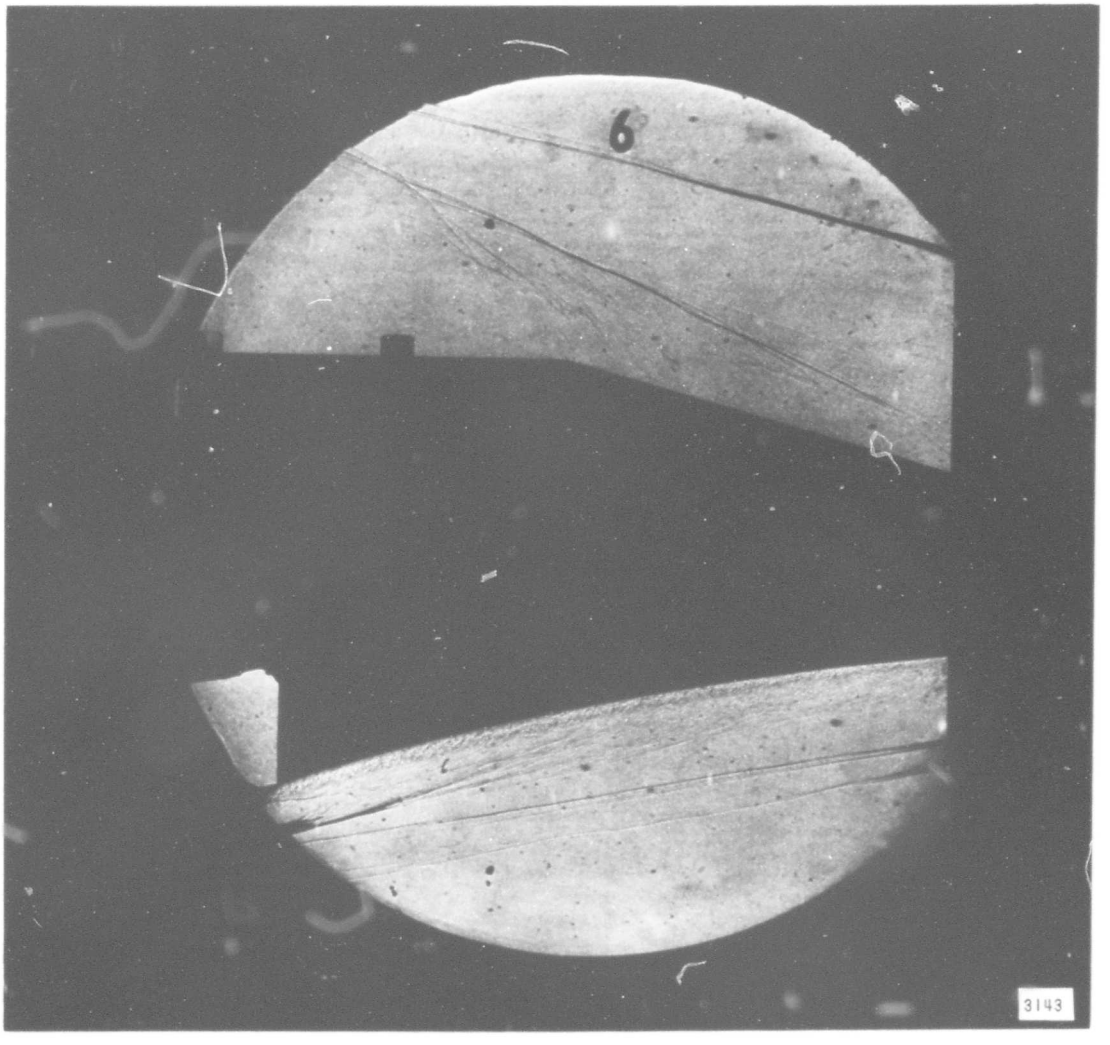

Figure 16 (CONTINUED) (e) MODEL E-2 SHADOWGRAPH, RUN 6

Figure 16 (CONTINUED) (f) MODEL E-2 SHADOWGRAPH, RUN 7

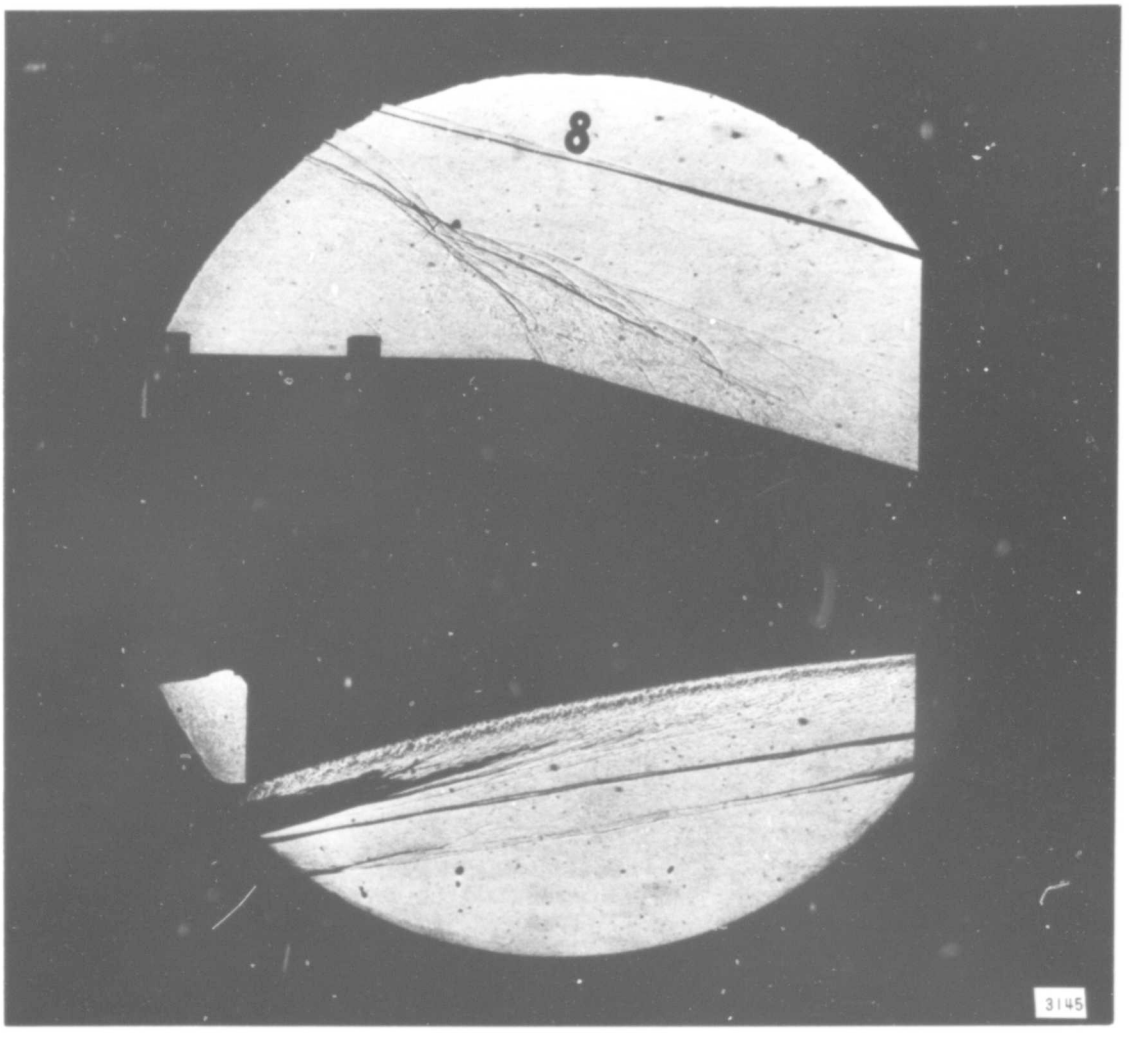

Figure 16 (CONTINUED) (g) MODEL E-2 SHADOWGRAPH, RUN 8

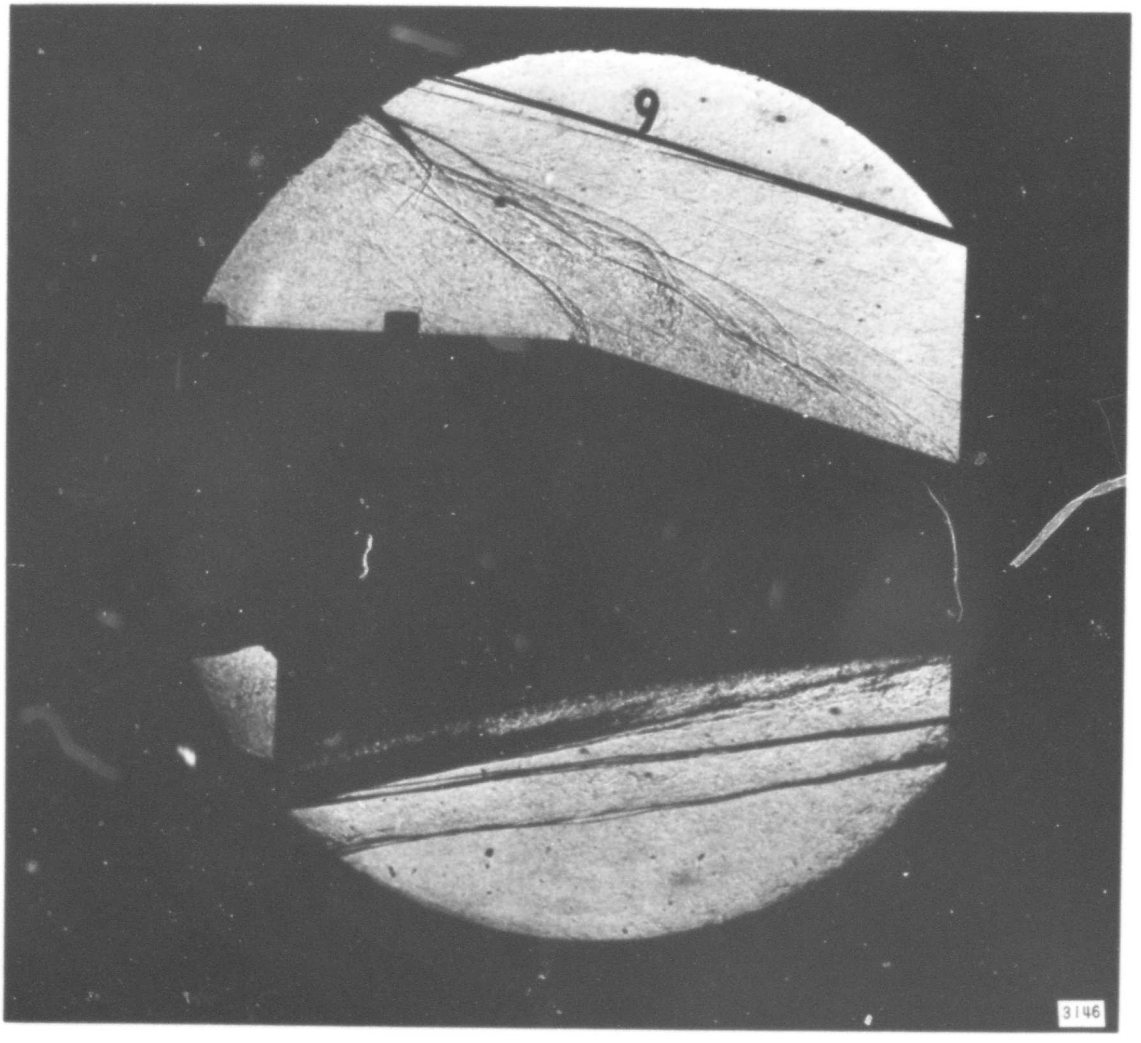

Figure 16 (CONTINUED) (h) MODEL E-2 SHADOWGRAPH, RUN 9

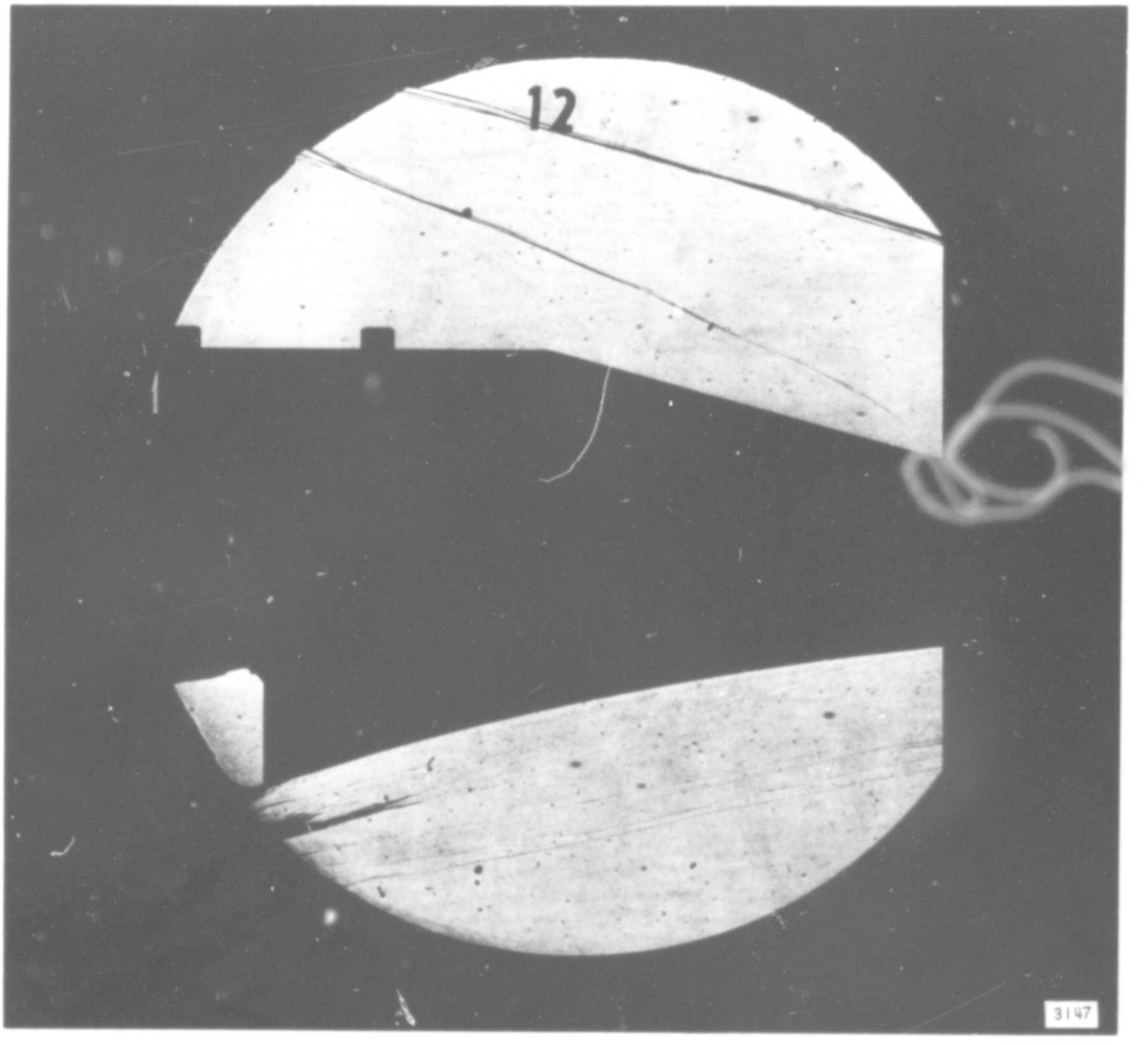

Figure 16 (CONTINUED) (i) MODEL E-2 SHADOWGRAPH, RUN 12

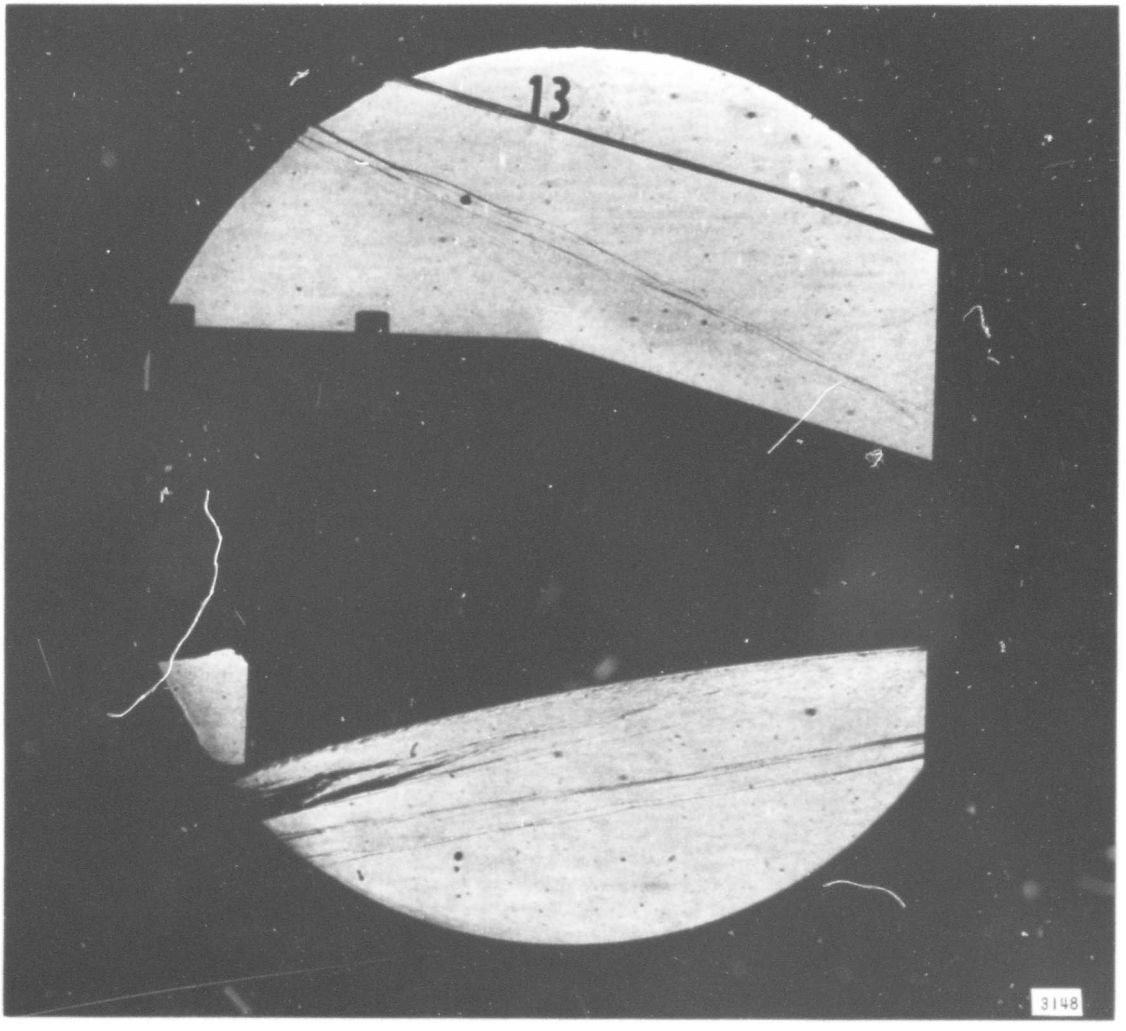

Figure 16 (CONTINUED) (j) MODEL E-2 SHADOWGRAPH, RUN 13

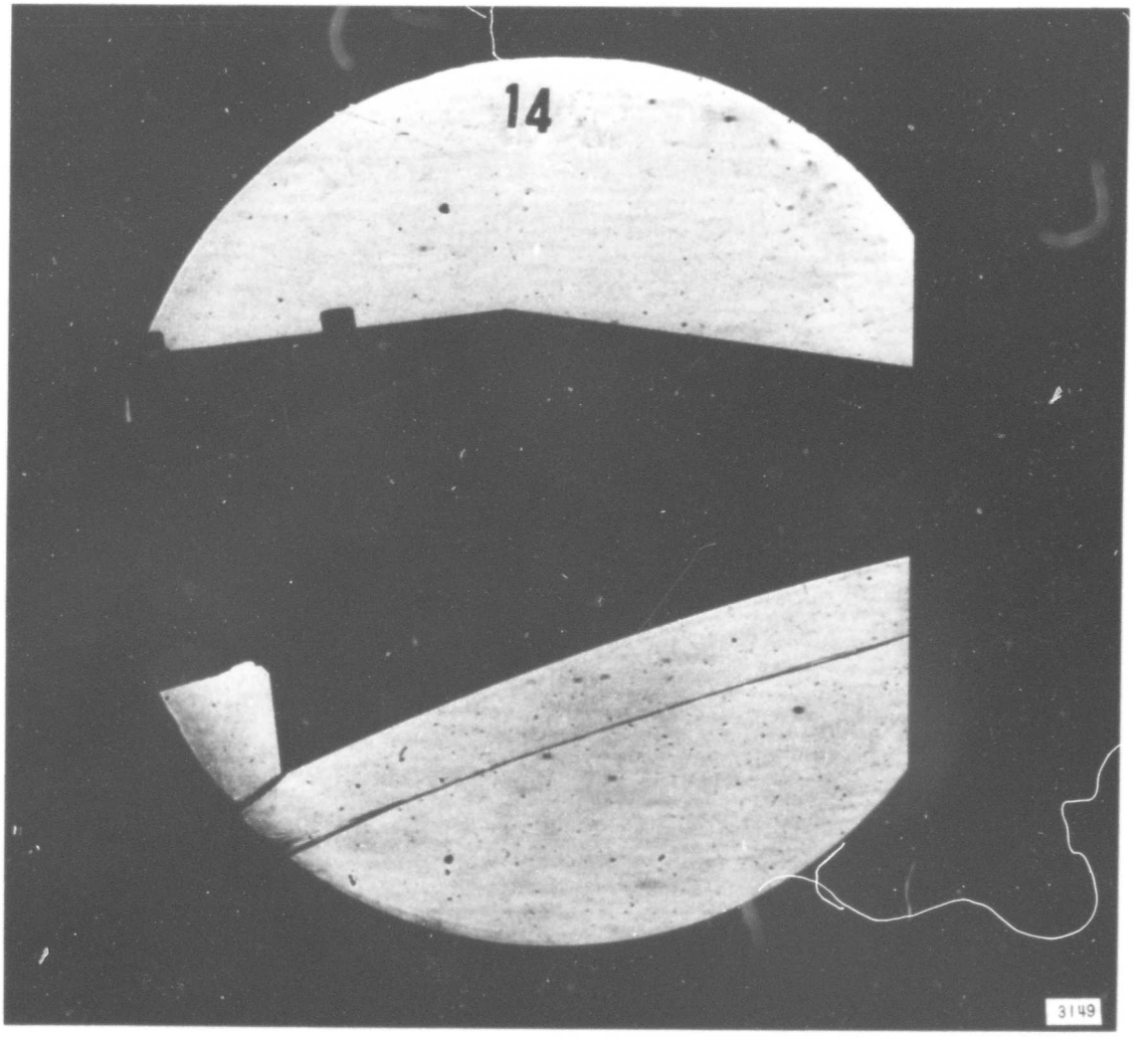

Figure 16 (CONTINUED) (k) MODEL E-2 SHADOWGRAPH, RUN 14

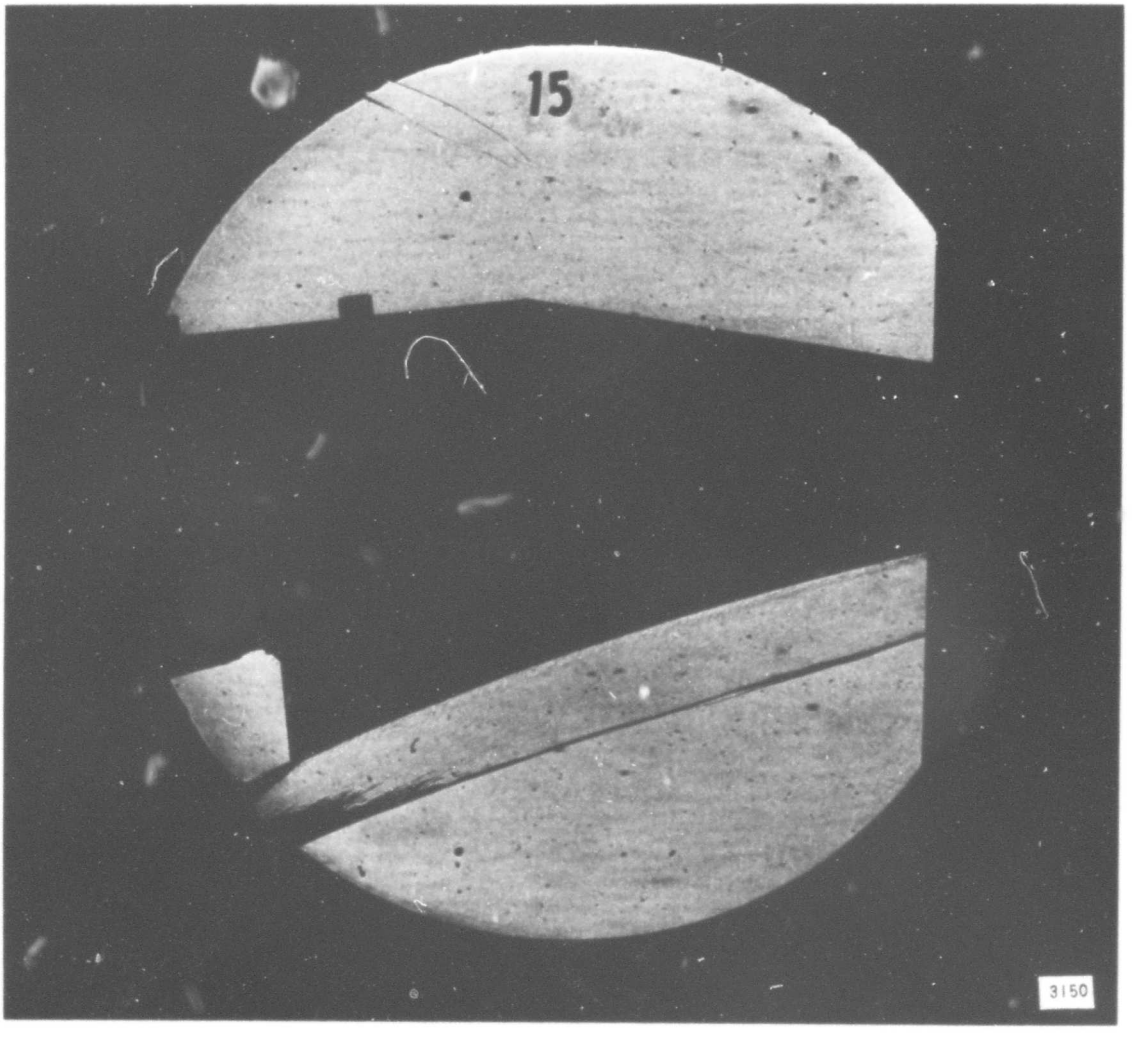

Figure 16 (CONTINUED) (ℓ) MODEL E-2 SHADOWGRAPH, RUN 15

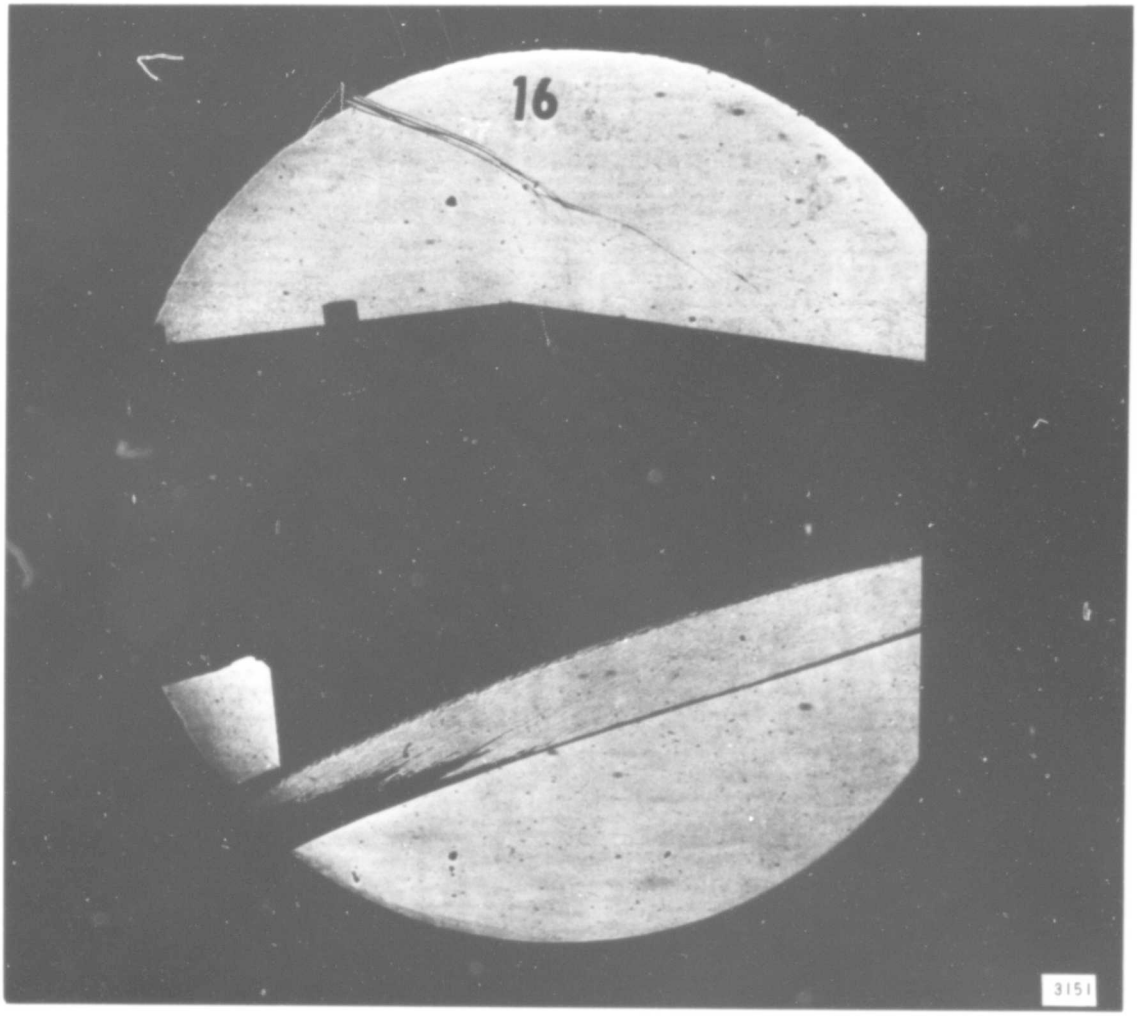

Figure 16 (CONTINUED) (m) MODEL E-2 SHADOWGRAPH, RUN 16

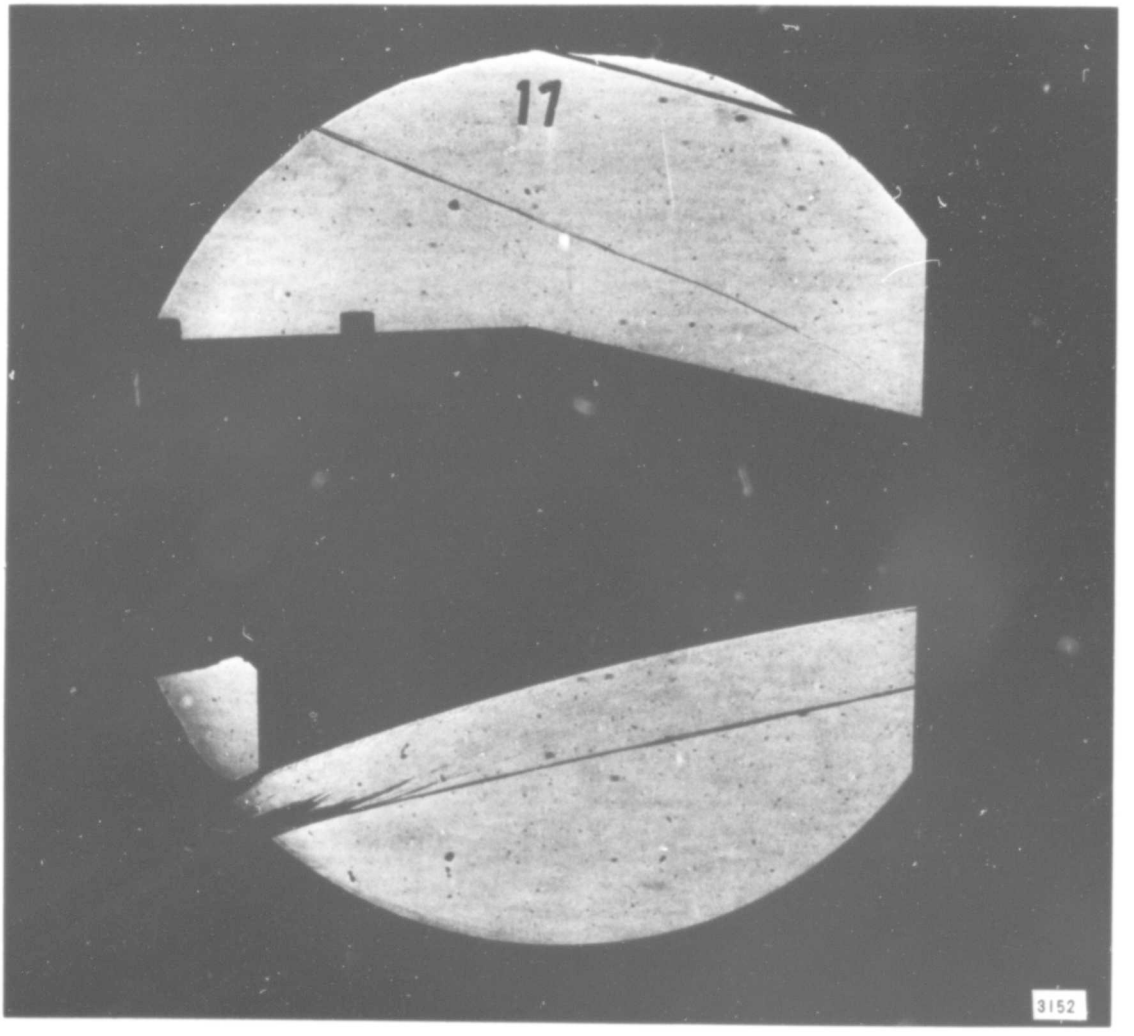

Figure 16 (CONCLUDED) (n) MODEL E-2 SHADOWGRAPH, RUN 17

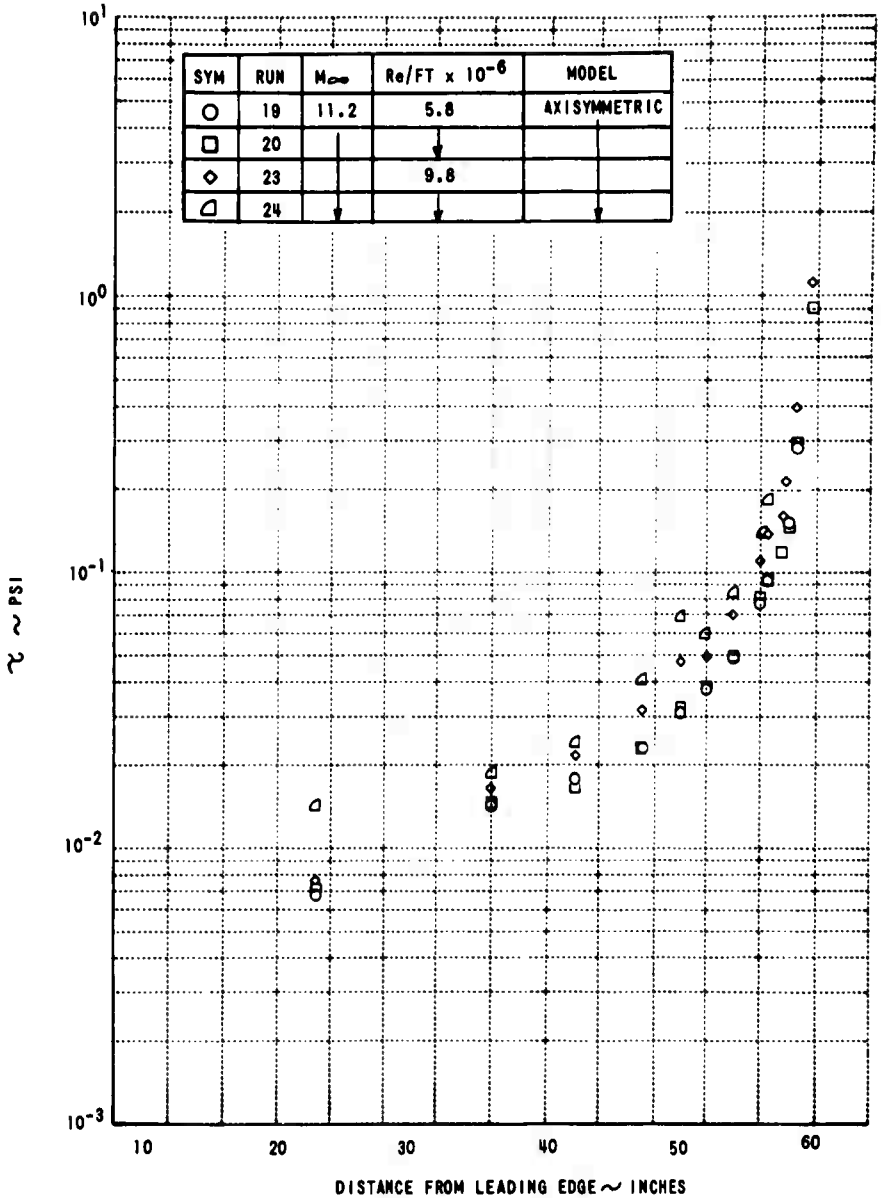

Figure 17 SKIN FRICTION DISTRIBUTIONS ON THE AXISYMMETRIC MODEL
(a) MACH NUMBER 11, SHARP NOSE

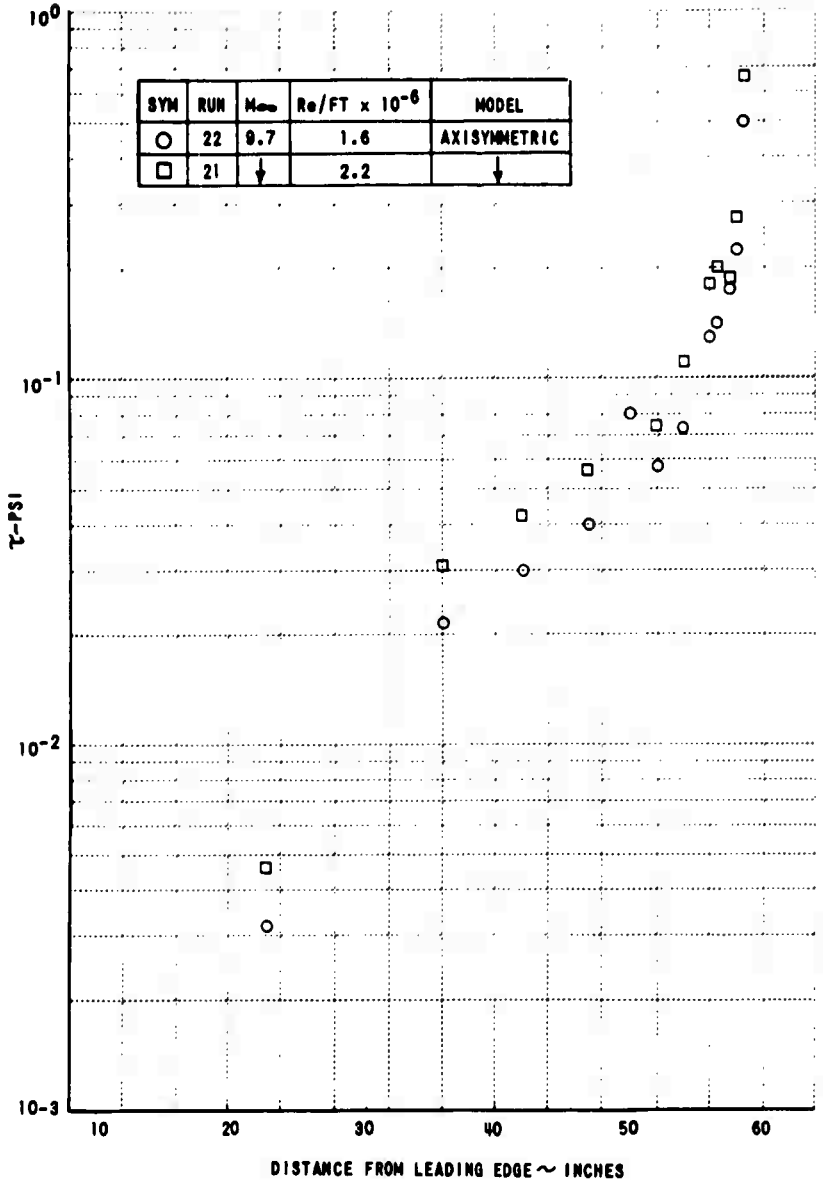

Figure 17 (CONTINUED) (b) MACH NUMBER 10, SHARP NOSE

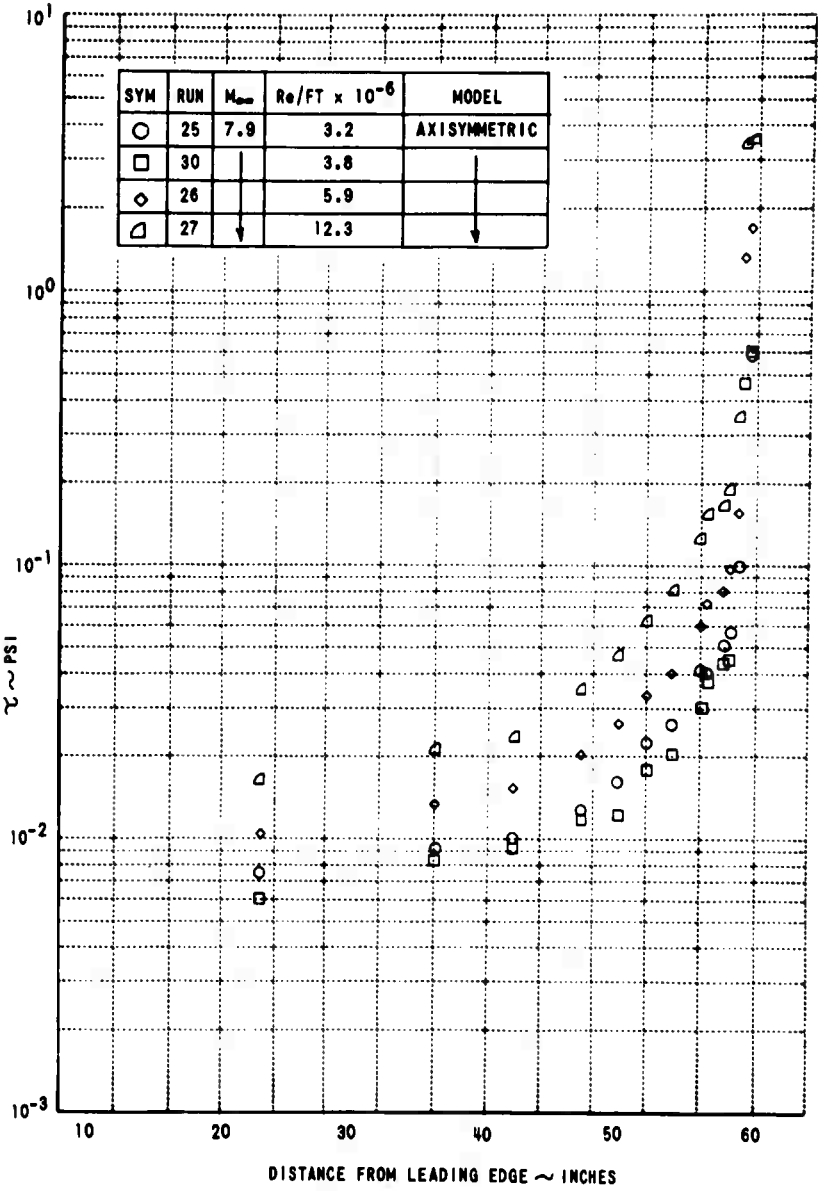

Figure 17 (CONTINUED) (c) MACH NUMBER 8, SHARP NOSE

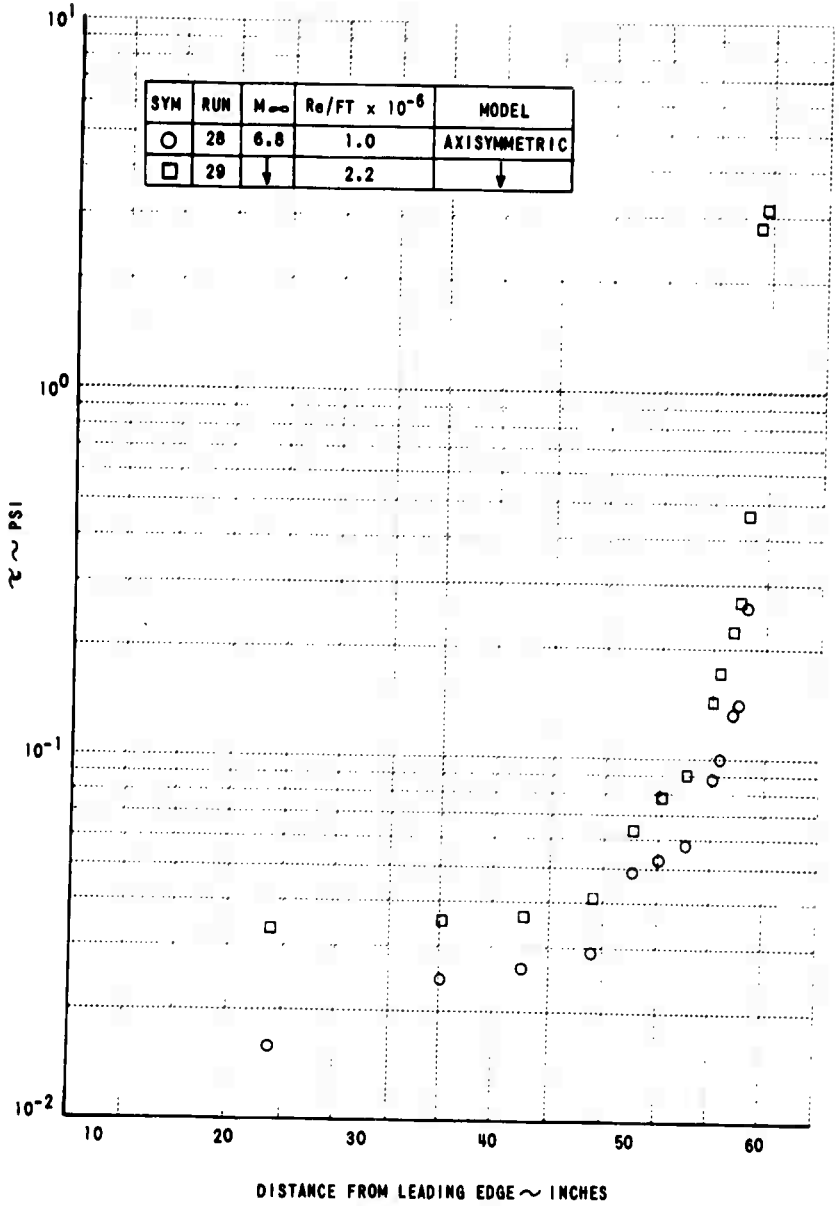

Figure 17 (CONTINUED) (d) MACH NUMBER 7, SHARP NOSE

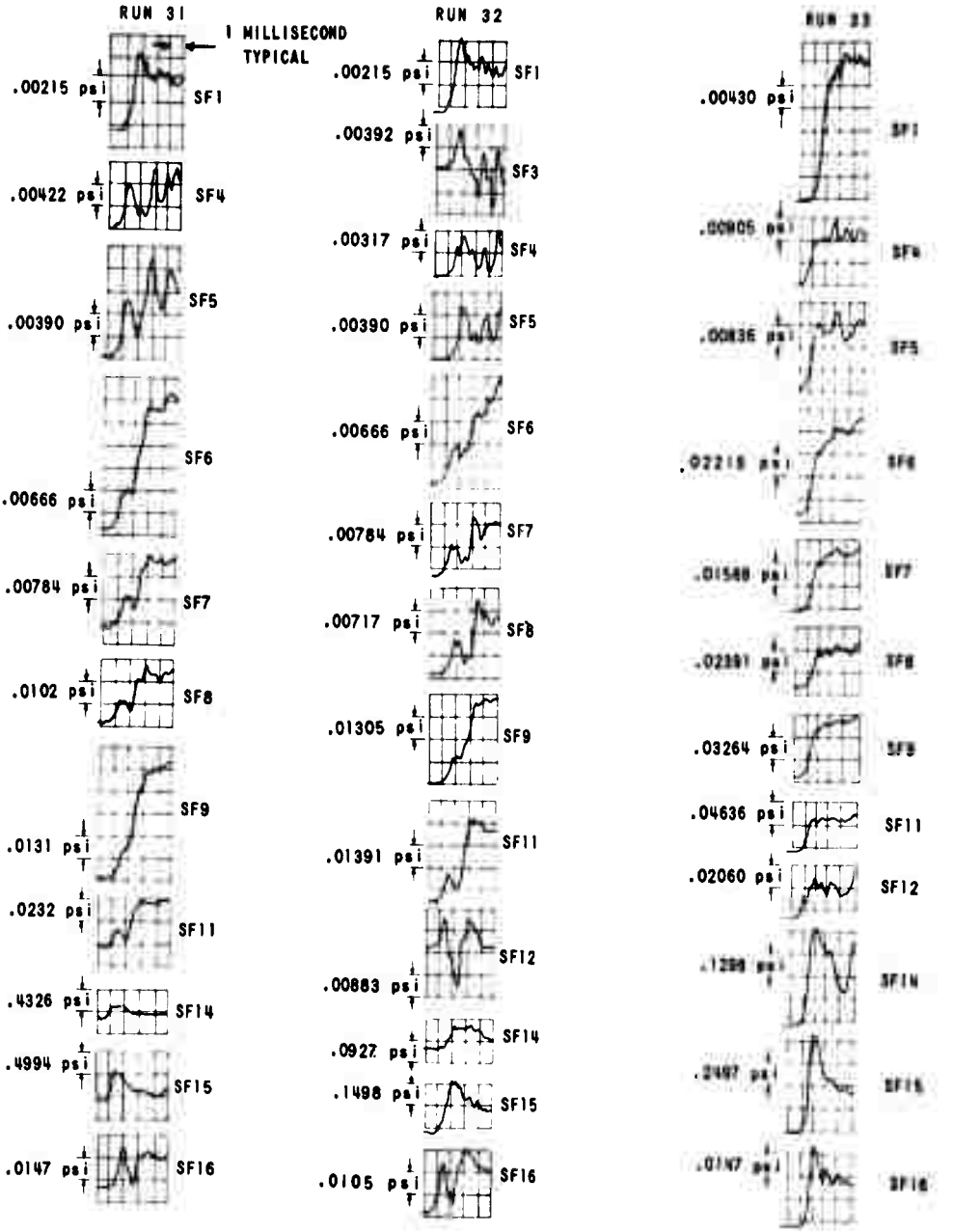

Figure 17 (CONCLUDED) (e) MACH NUMBER 7, BLUNT NOSE

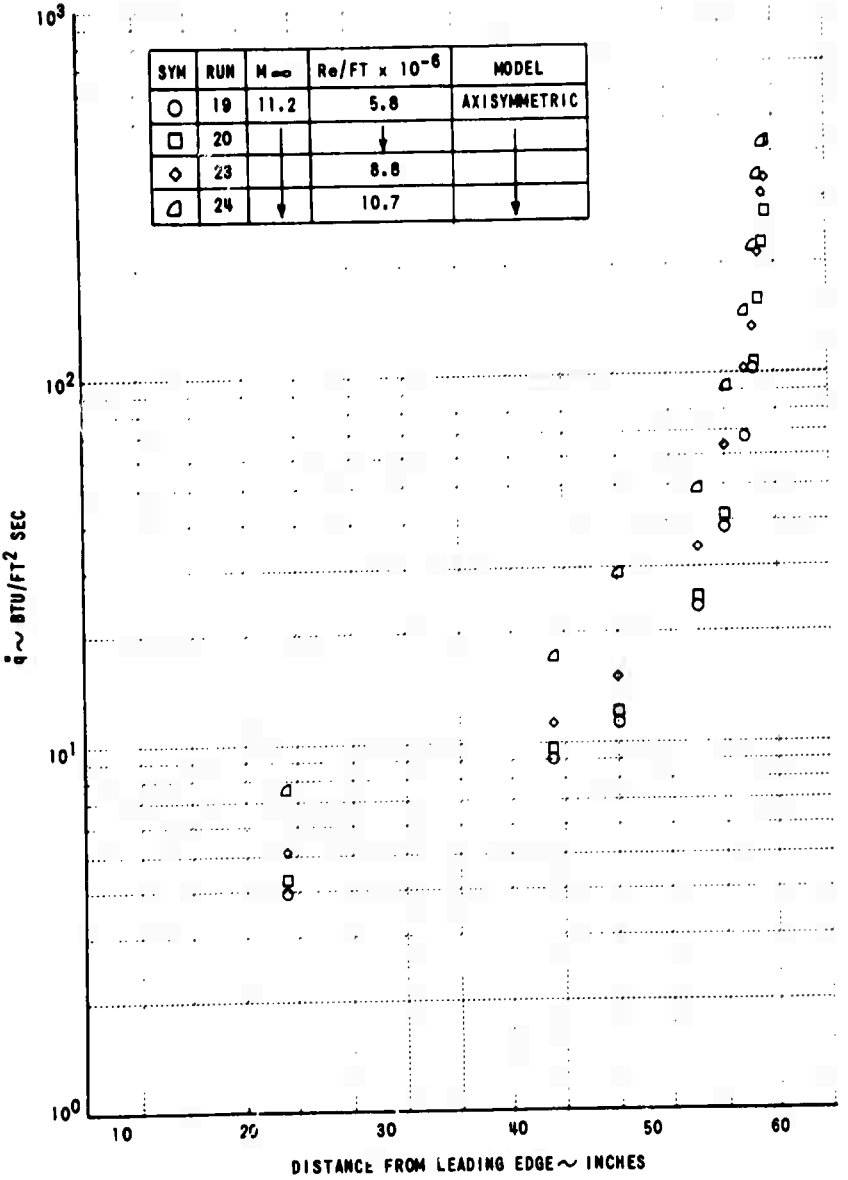

Figure 18 HEAT TRANSFER DISTRIBUTIONS ON THE AXISYMMETRIC MODEL
(a) MACH NUMBER 11, SHARP NOSE

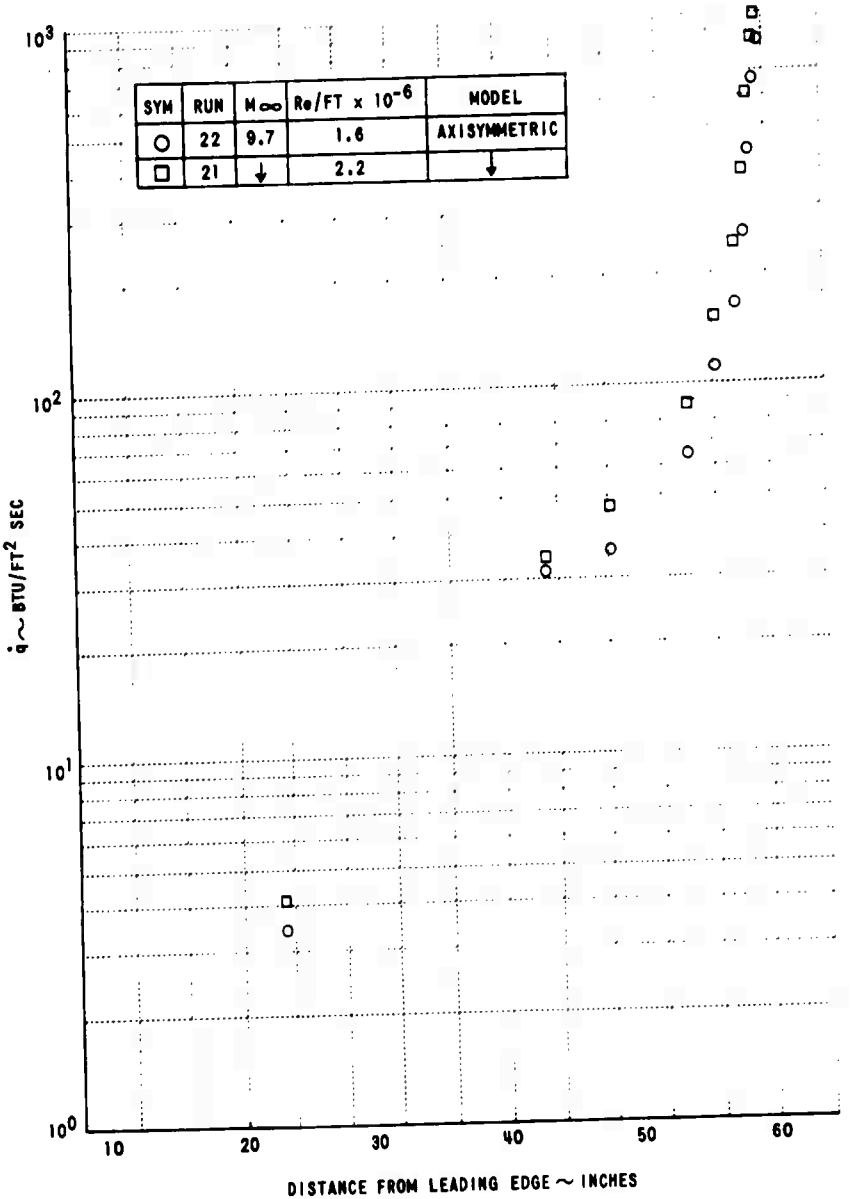

Figure 18 (CONTINUED) (b) MACH NUMBER 10, SHARP NOSE

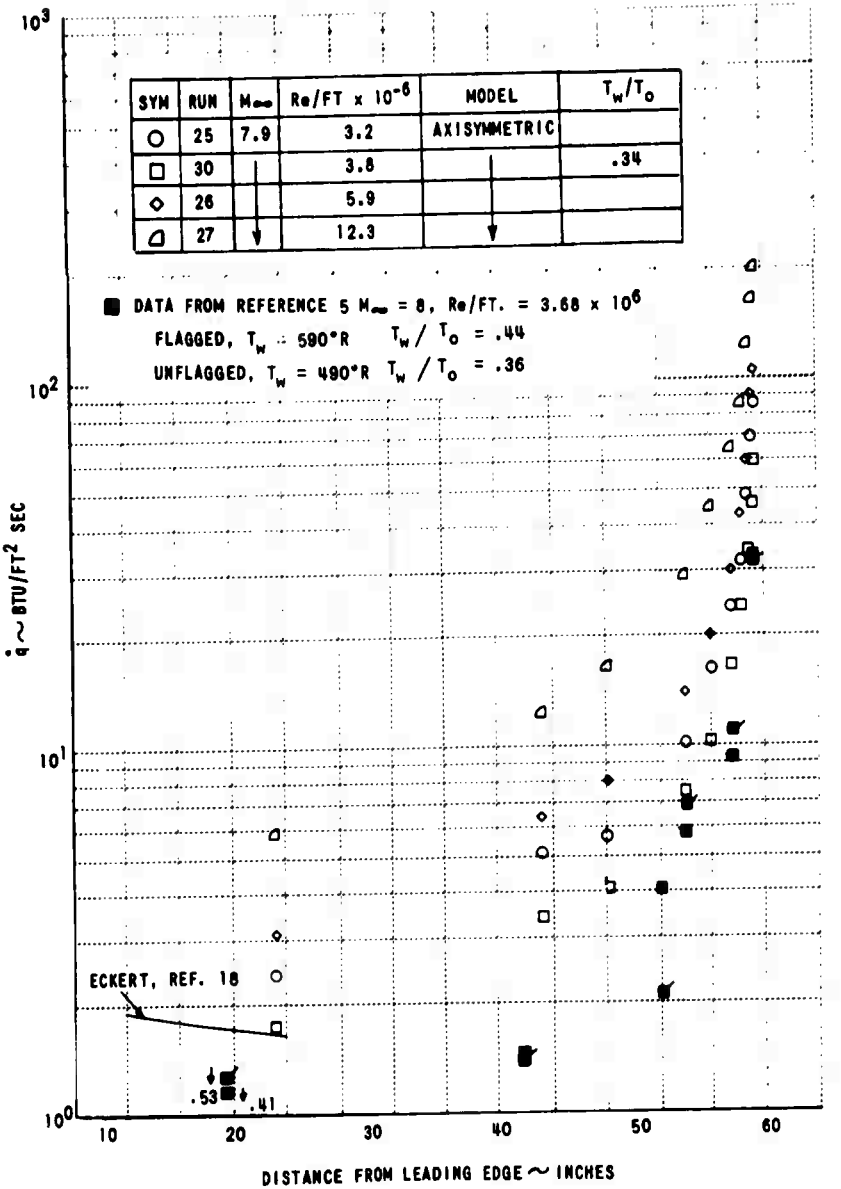

Figure 18 (CONTINUED) (c) MACH NUMBER 8, SHARP NOSE

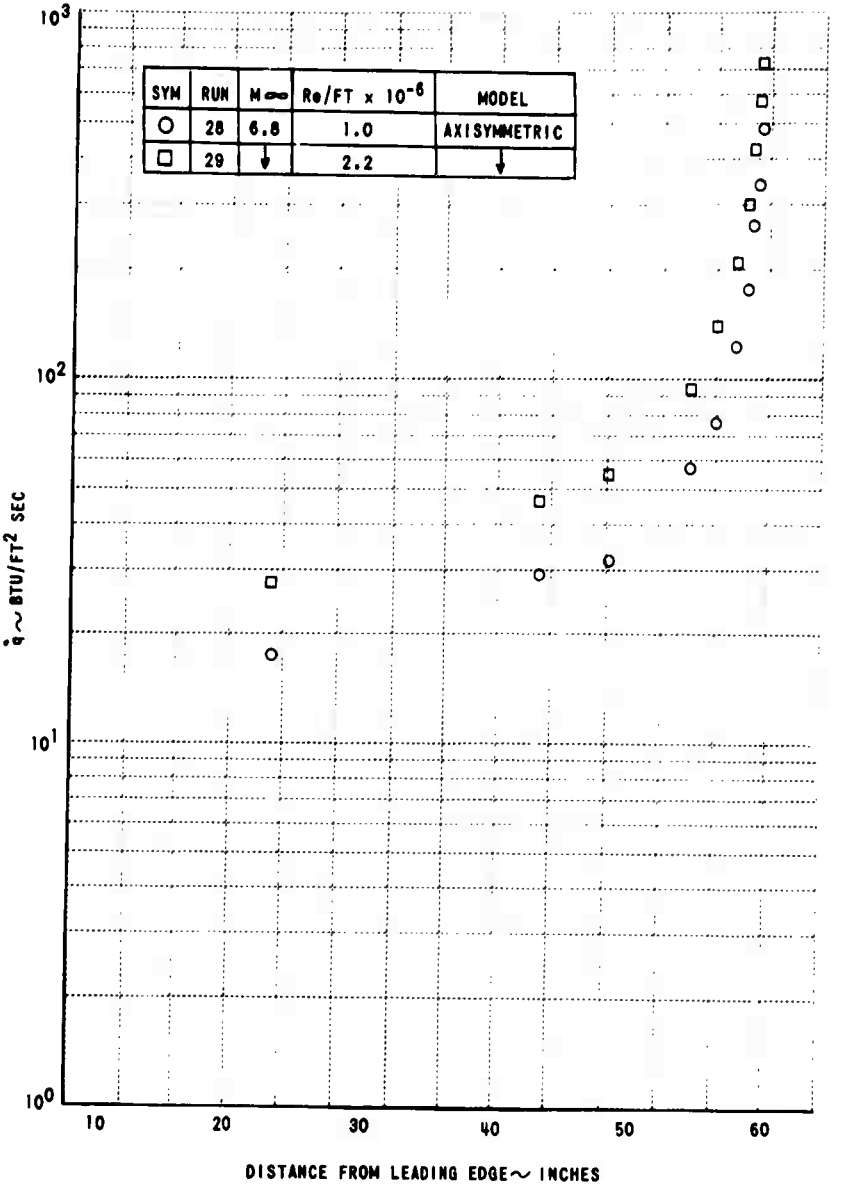

Figure 18 (CONTINUED) (d) MACH NUMBER 7, SHARP NOSE

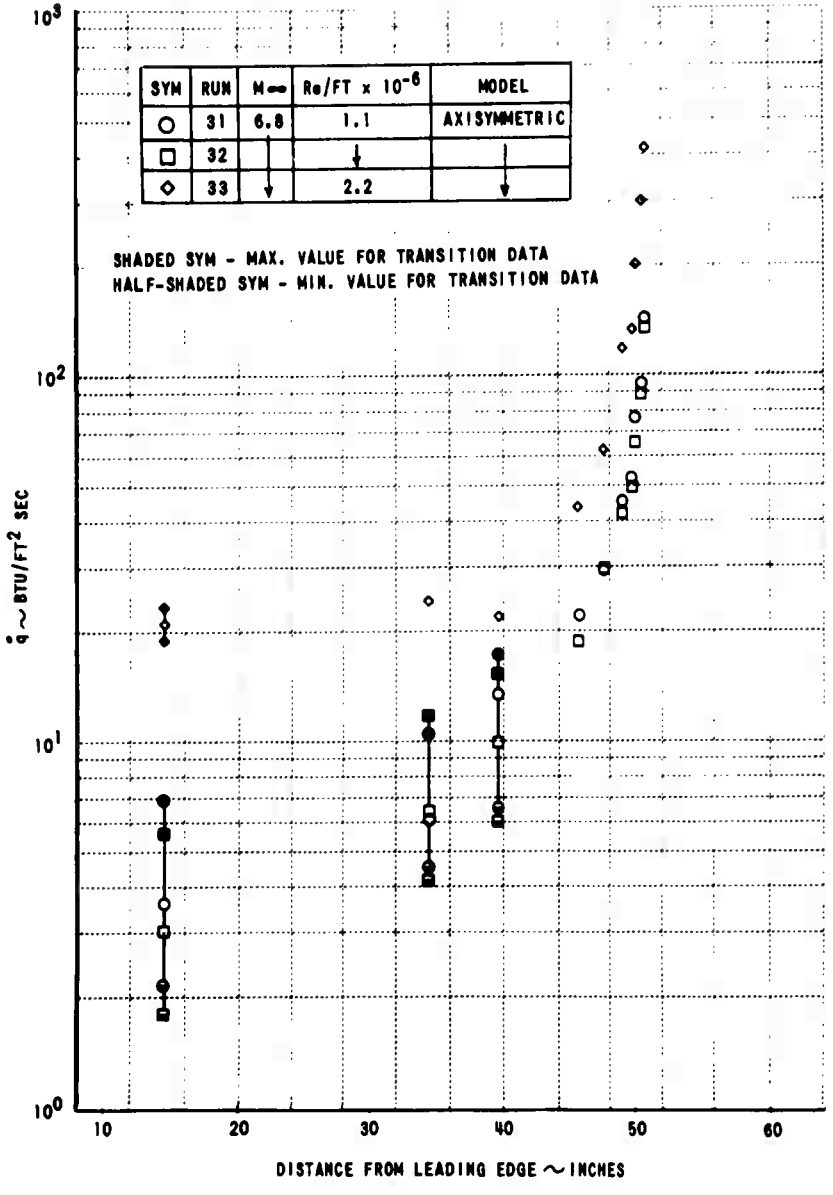

Figure 18 (CONCLUDED) (e) MACH NUMBER 7, BLUNT NOSE

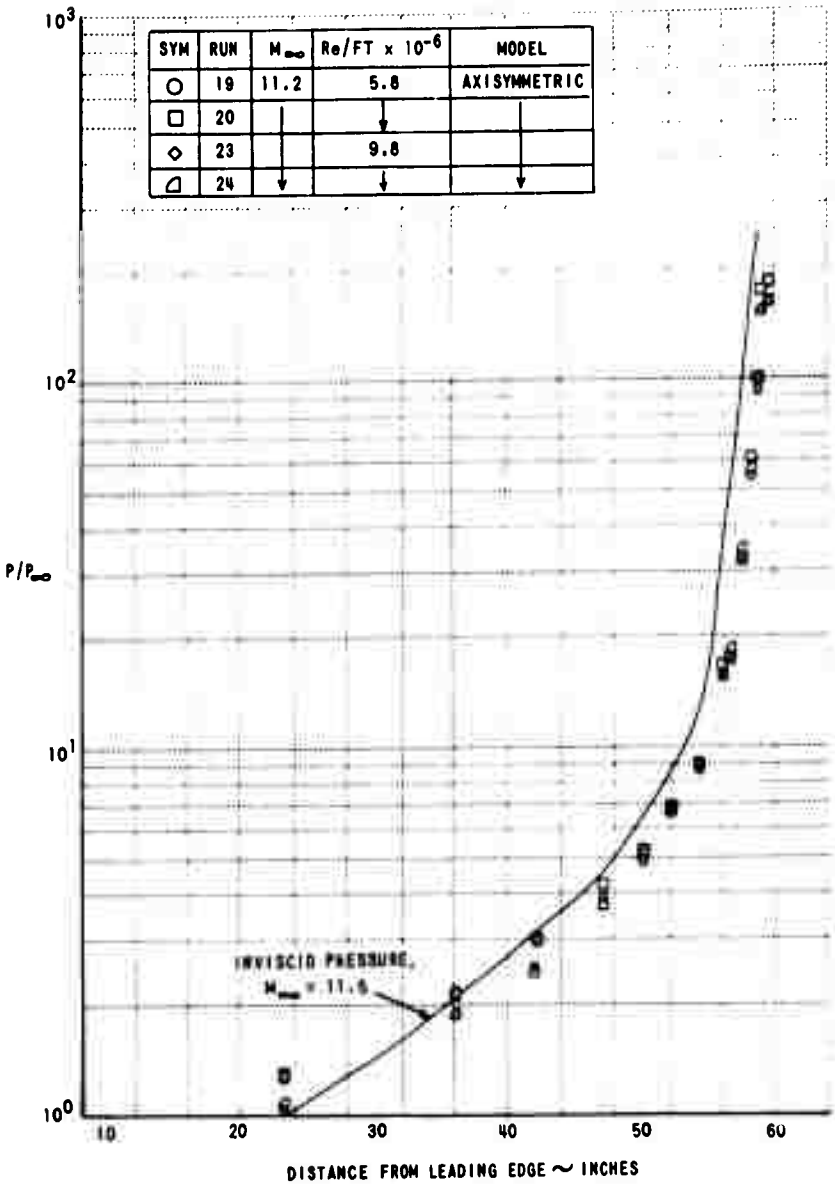

Figure 19 PRESSURE DISTRIBUTIONS ON THE AXISYMMETRIC MODEL
(a) MACH NUMBER 11, SHARP NOSE

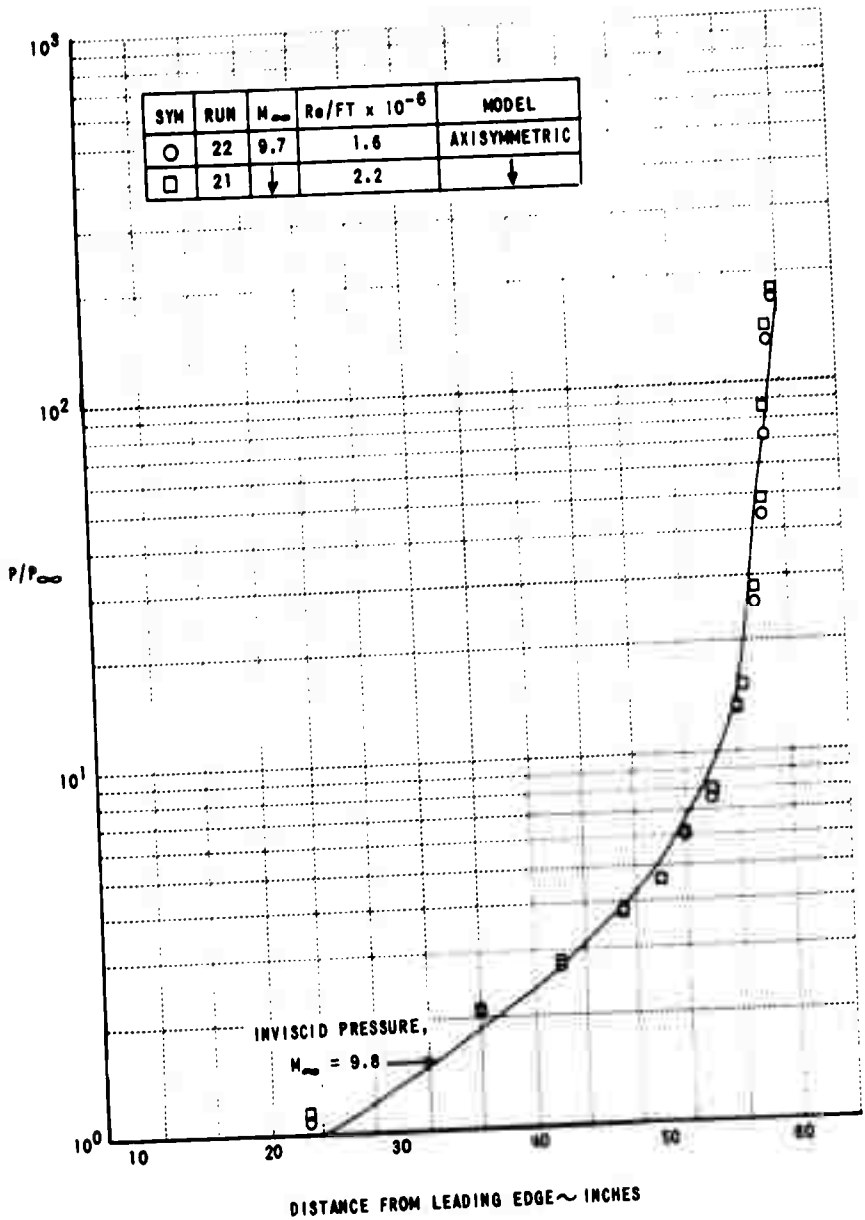

Figure 19 (CONTINUED) (b) MACH NUMBER 10, SHARP NOSE

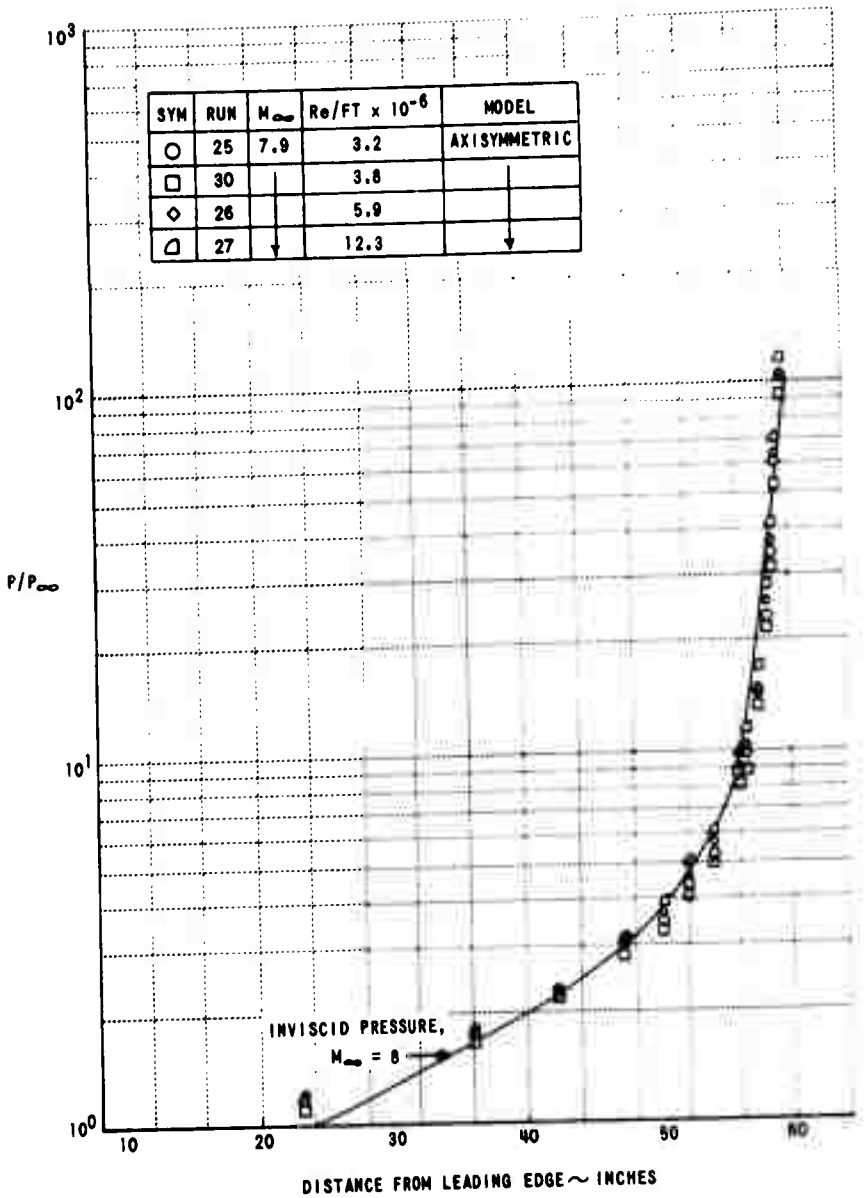

Figure 19 (CONTINUED) (c) MACH NUMBER 8, SHARP NOSE

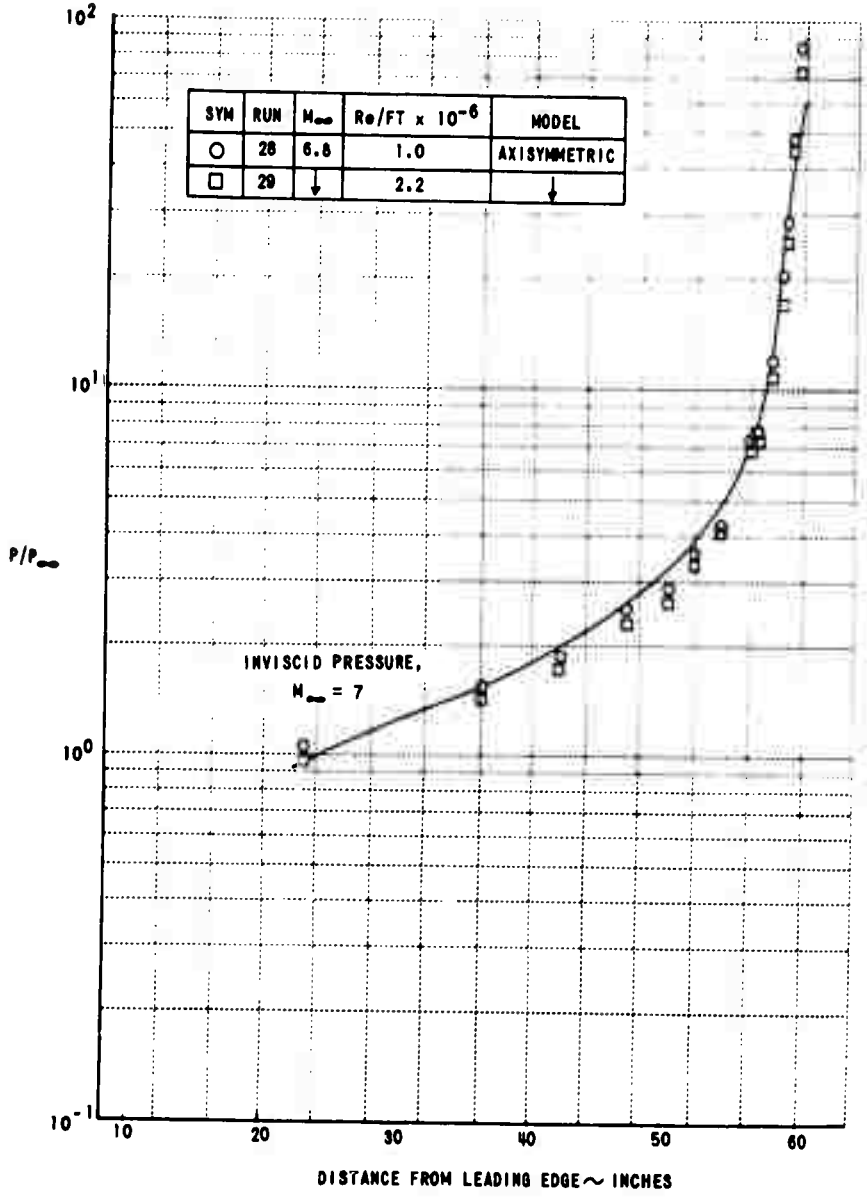

Figure 19 (CONTINUED) (d) MACH NUMBER 7, SHARP NOSE

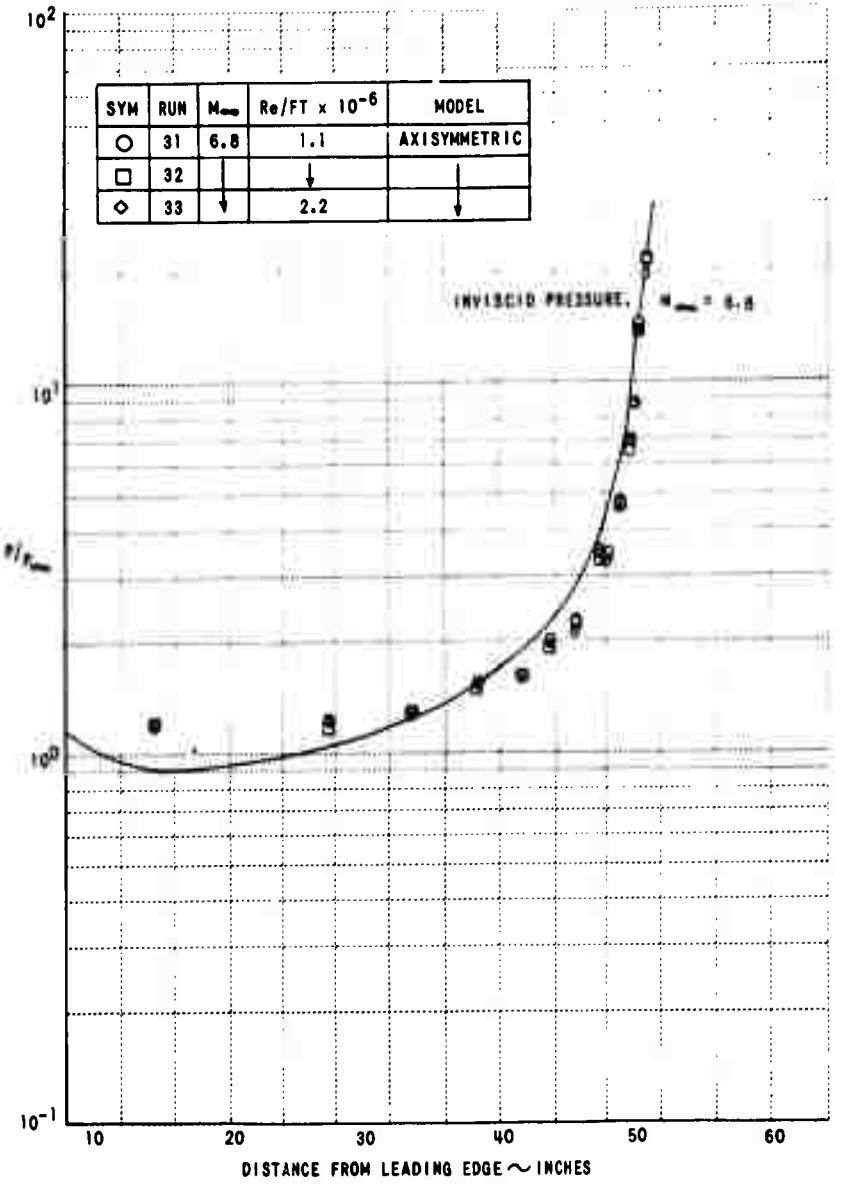

Figure 19 (CONCLUDED) (e) MACH NUMBER 7, BLUNT NOSE

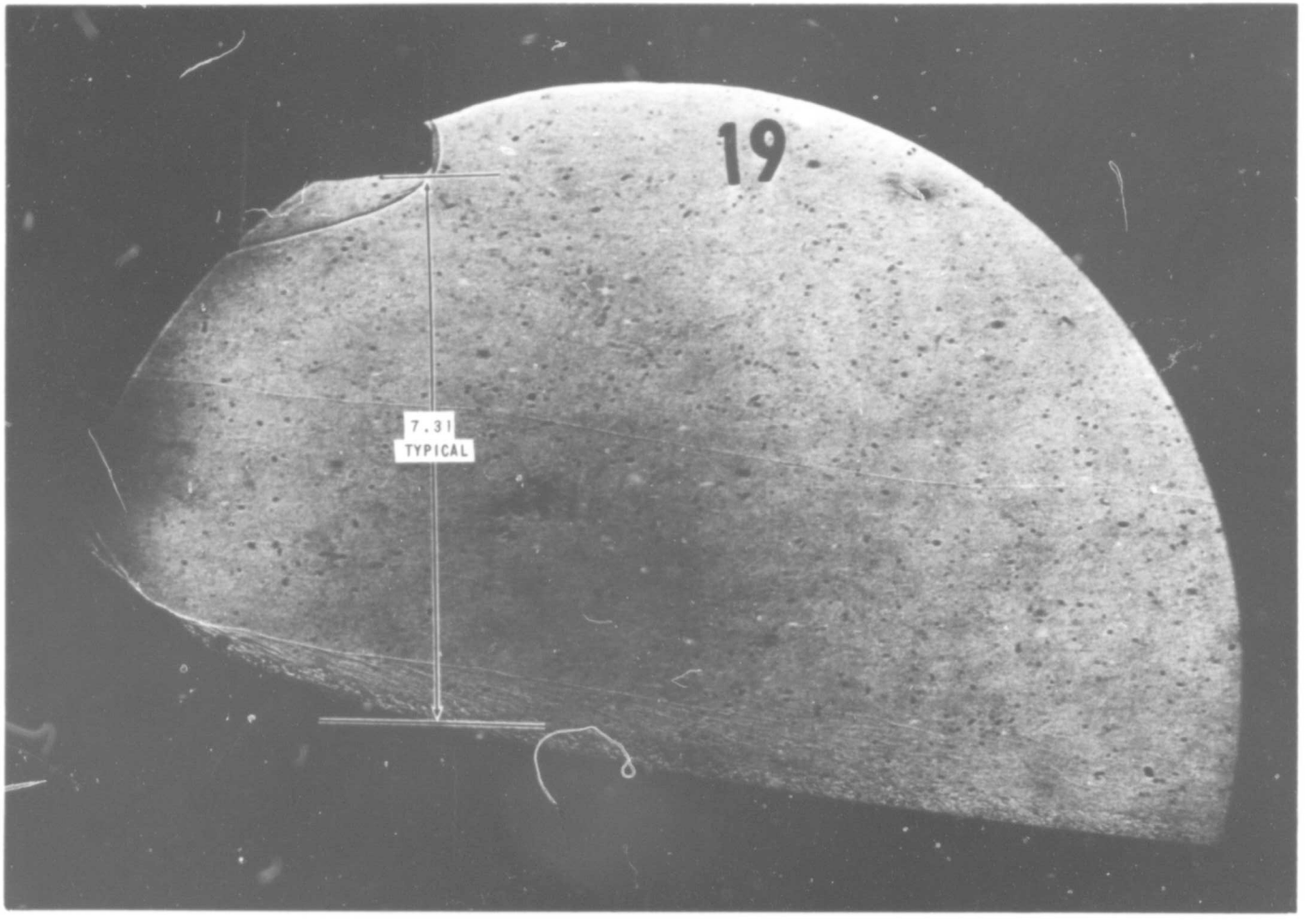

Figure 20 AXISYMMETRIC MODEL FLOW PHOTOGRAPHS
(a) AXISYMMETRIC MODEL SHADOWGRAPH, RUN 19

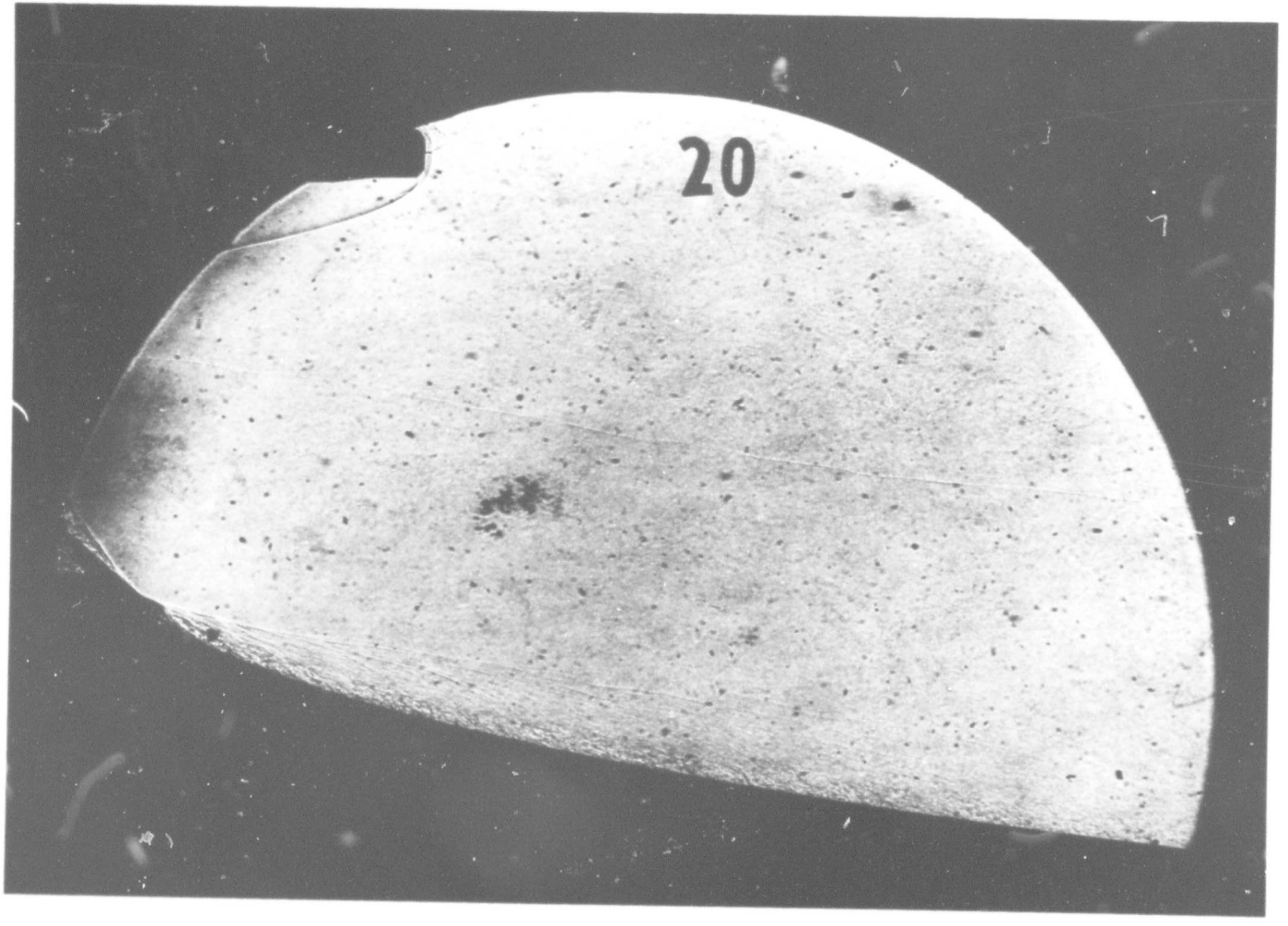

Figure 20 (CONTINUED) (b) AXISYMMETRIC MODEL SHADOWGRAPH, RUN 20

Figure 20 (CONTINUED) (c) AXISYMMETRIC MODEL SHADOWGRAPH, RUN 21

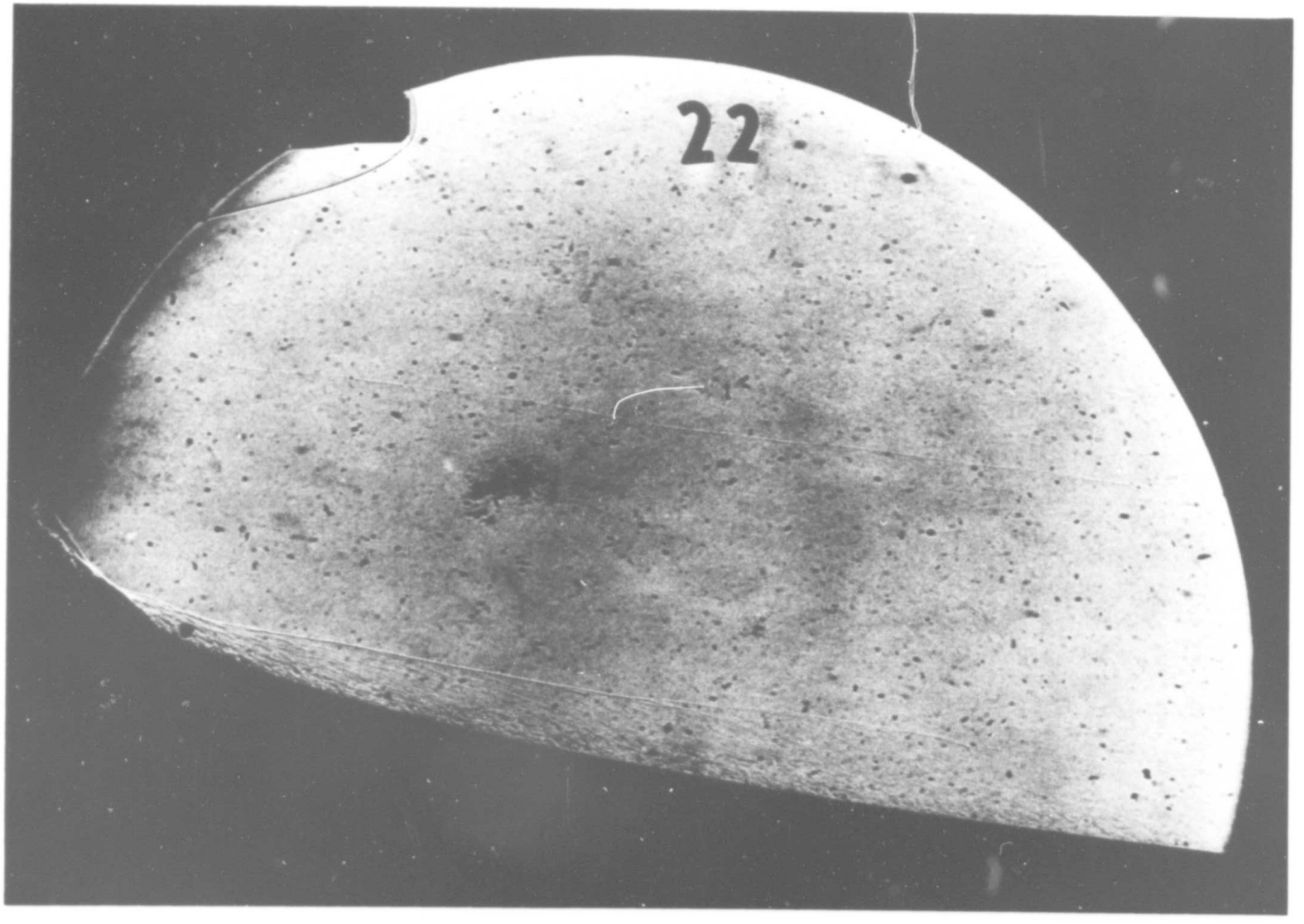

Figure 20 (CONTINUED) (d) AXISYMMETRIC MODEL SHADOWGRAPH, RUN 22

Figure 20 (CONTINUED) (e) AXISYMMETRIC MODEL SHADOWGRAPH, RUN 23

Figure 20 (CONTINUED) (f) AXISYMMETRIC MODEL SHADOWGRAPH, RUN 24

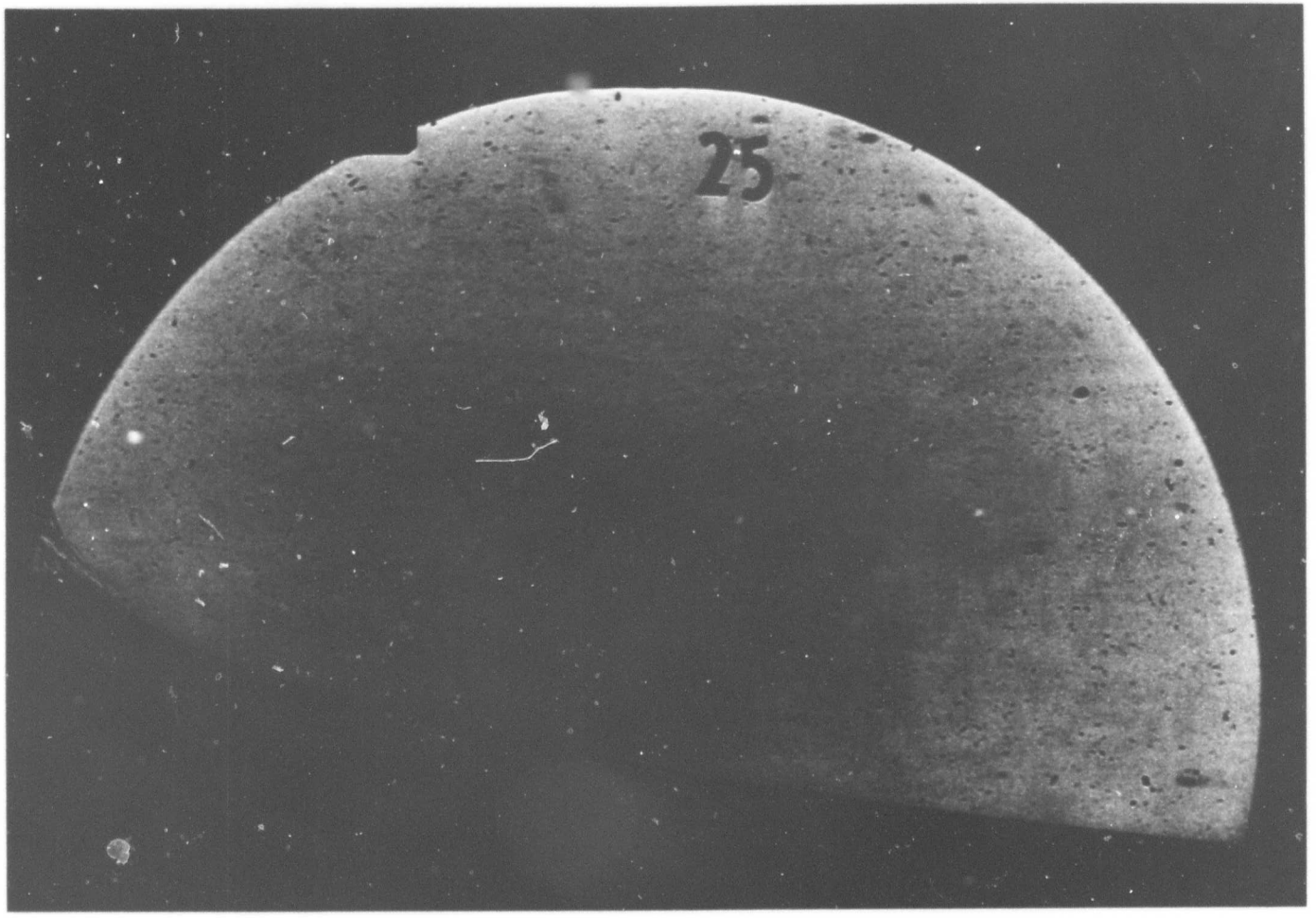

Figure 20 (CONTINUED) (g) AXISYMMETRIC MODEL SHADOWGRAPH, RUN 25

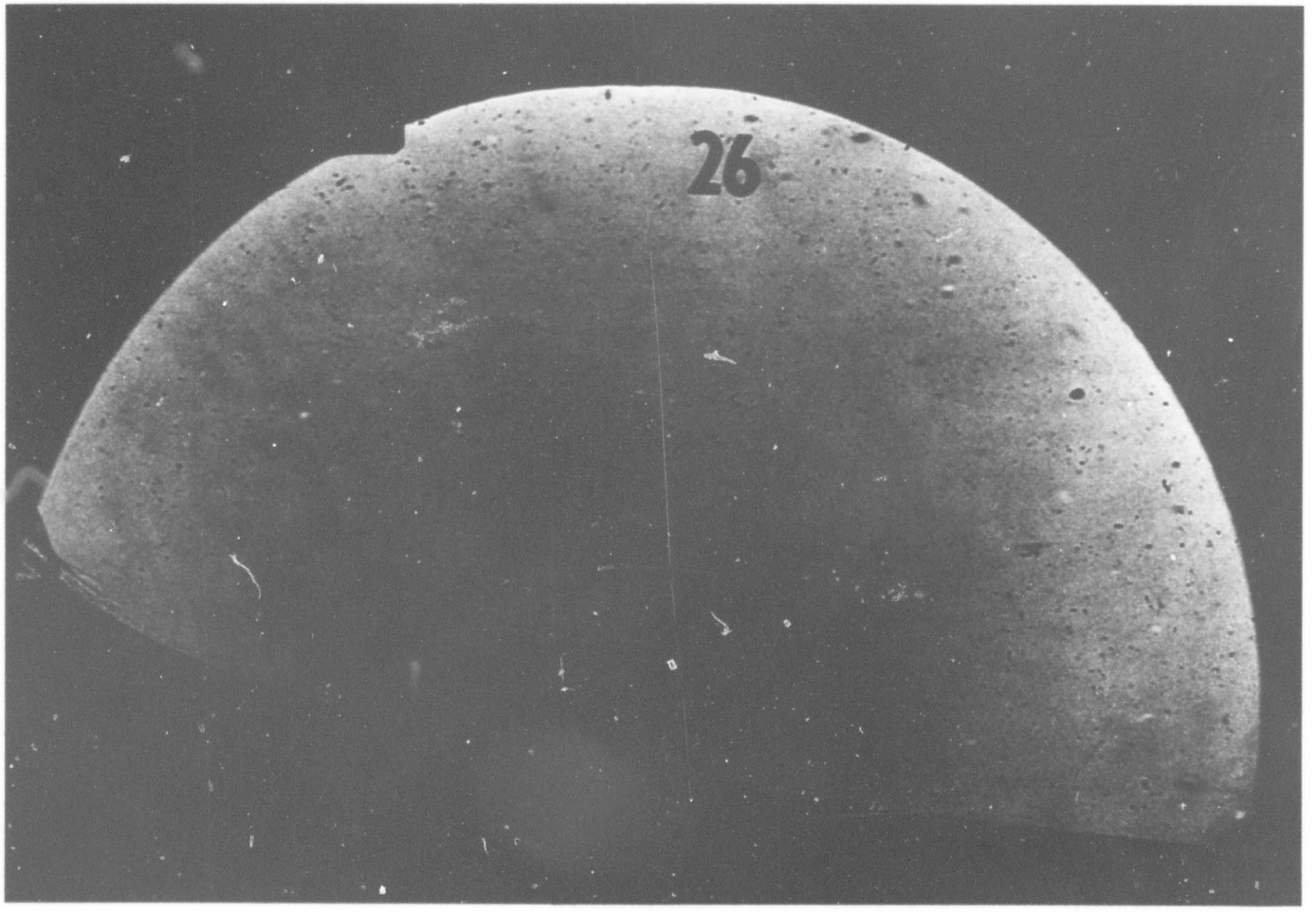

Figure 20 (CONTINUED) (h) AXISYMMETRIC MODEL SHADOWGRAPH, RUN 26

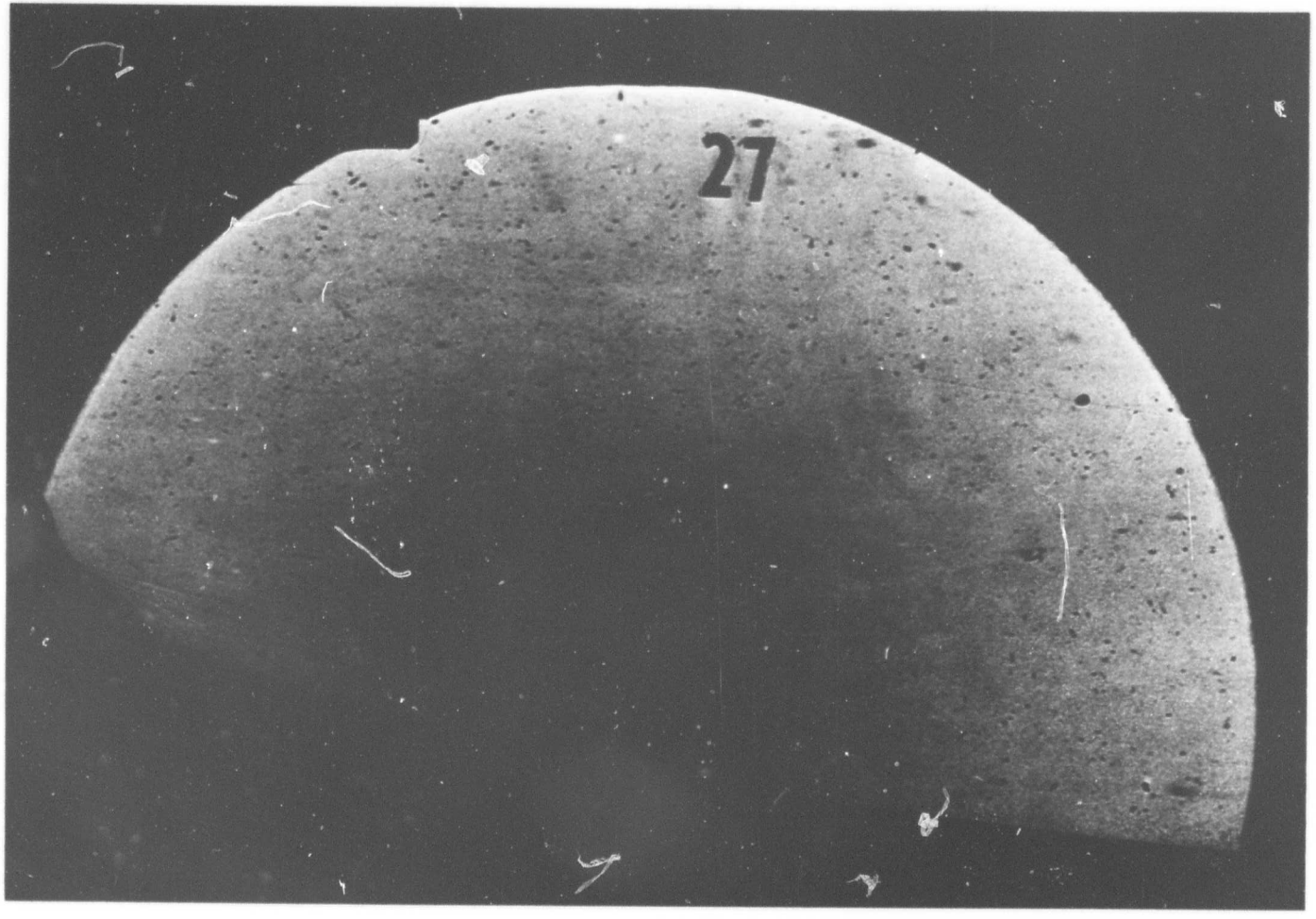

Figure 20 (CONTINUED) (i) AXISYMMETRIC MODEL SHADOWGRAPH, RUN 27

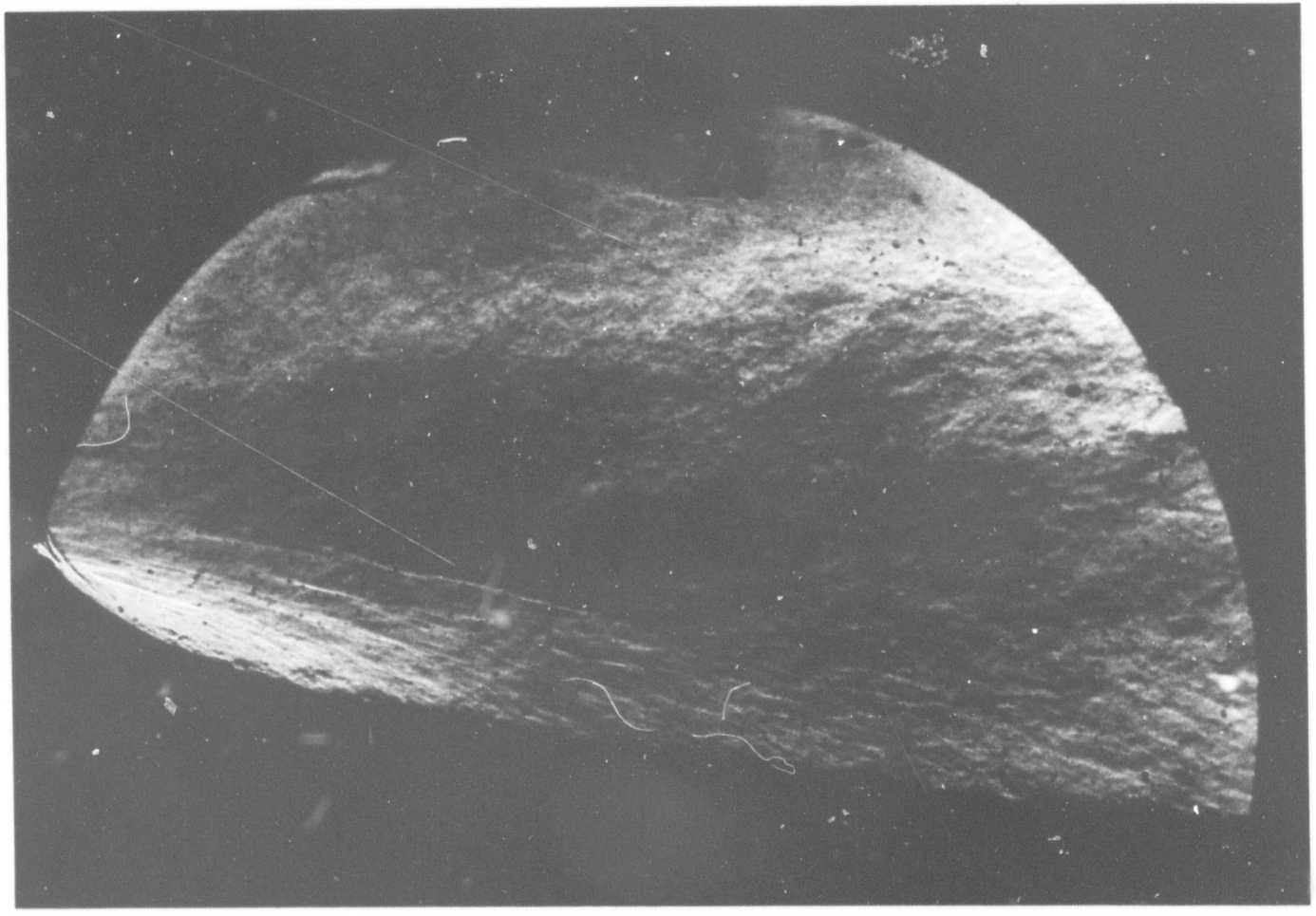

Figure 20 (CONTINUED) (j) AXISYMMETRIC MODEL SCHLIEREN, RUN 28

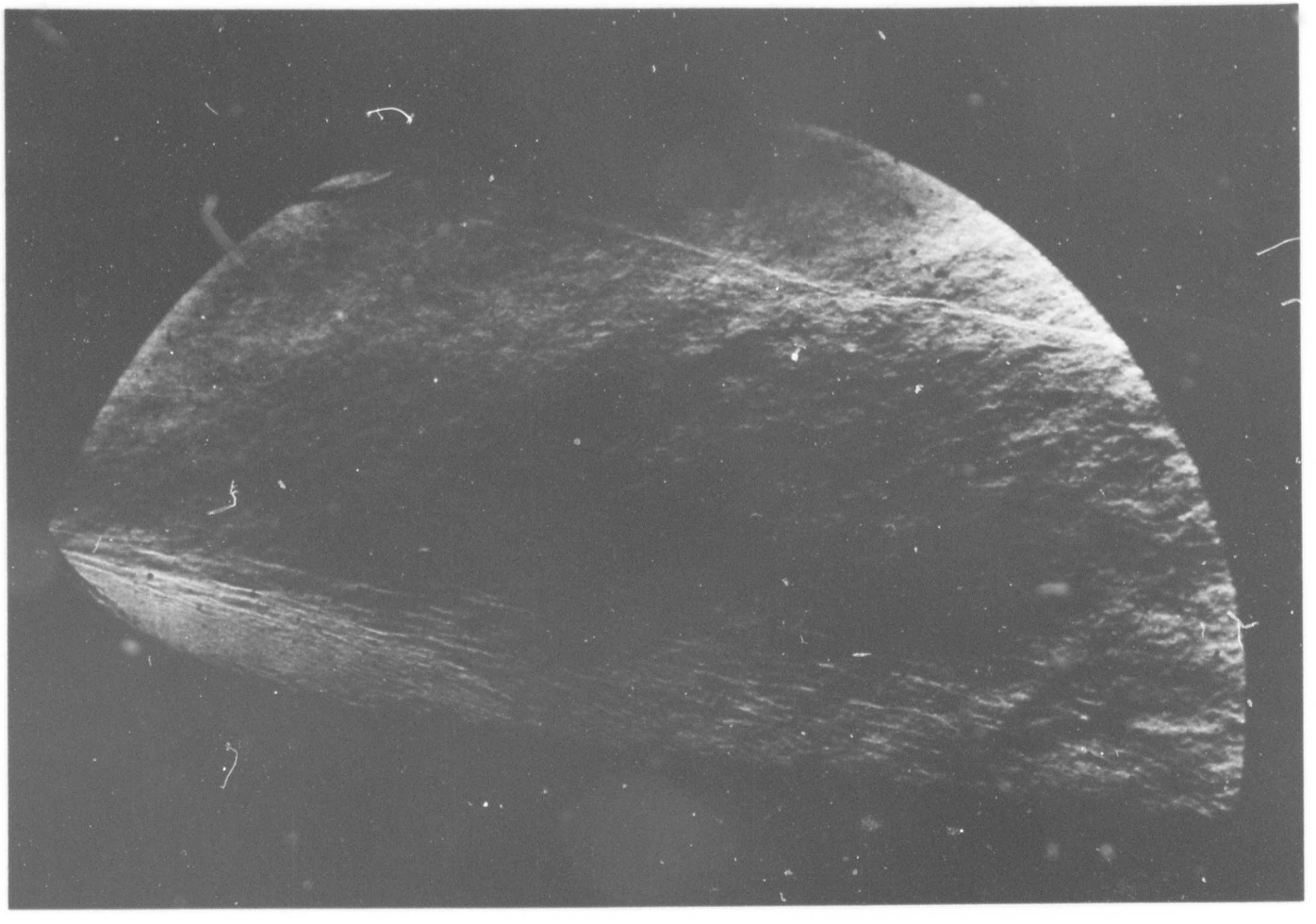

Figure 20 (CONTINUED) (k) AXISYMMETRIC MODEL SCHLIEREN, RUN 29

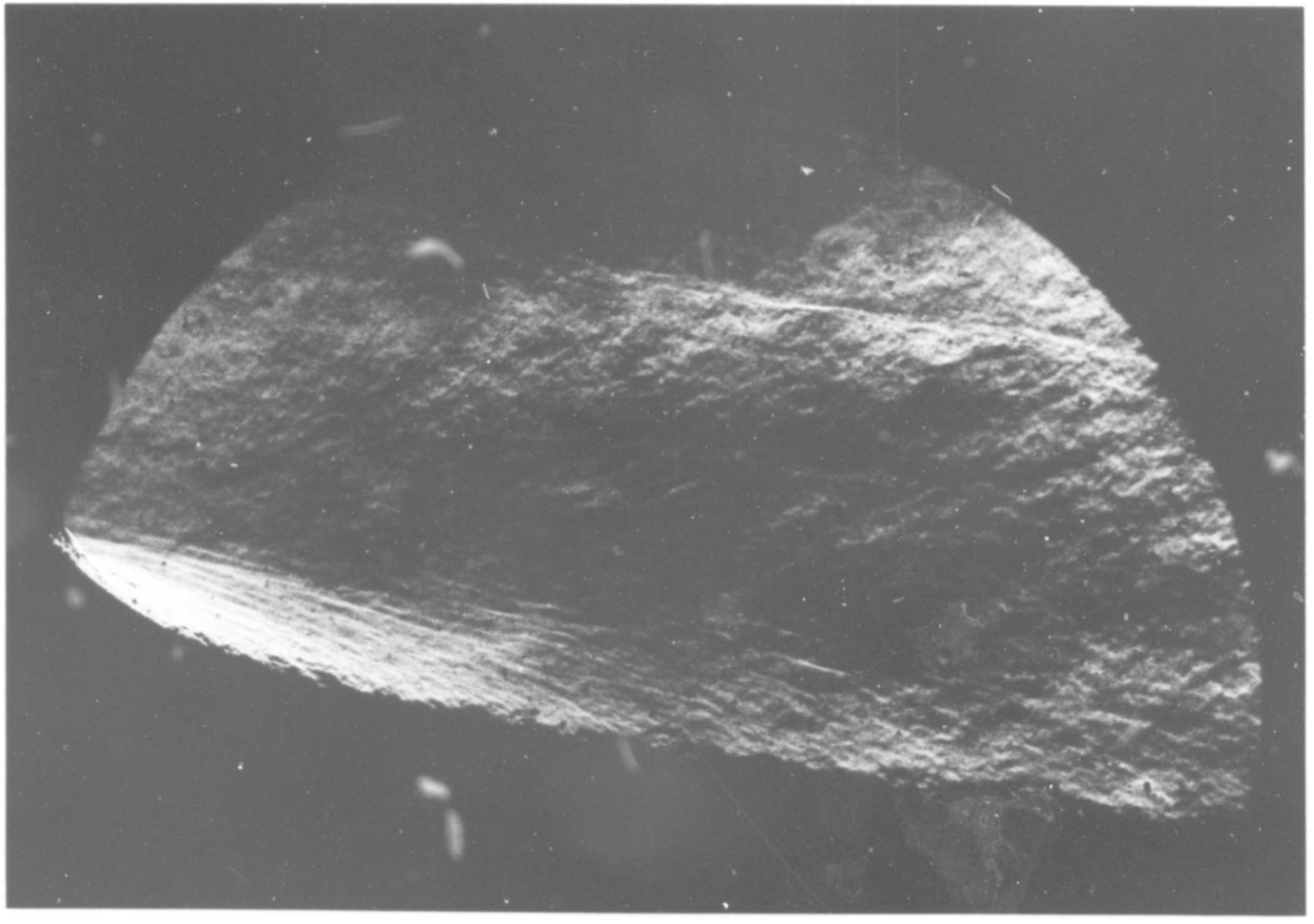

Figure 20 (CONTINUED) (ℓ) AXISYMMETRIC MODEL SCHLIEREN, RUN 30

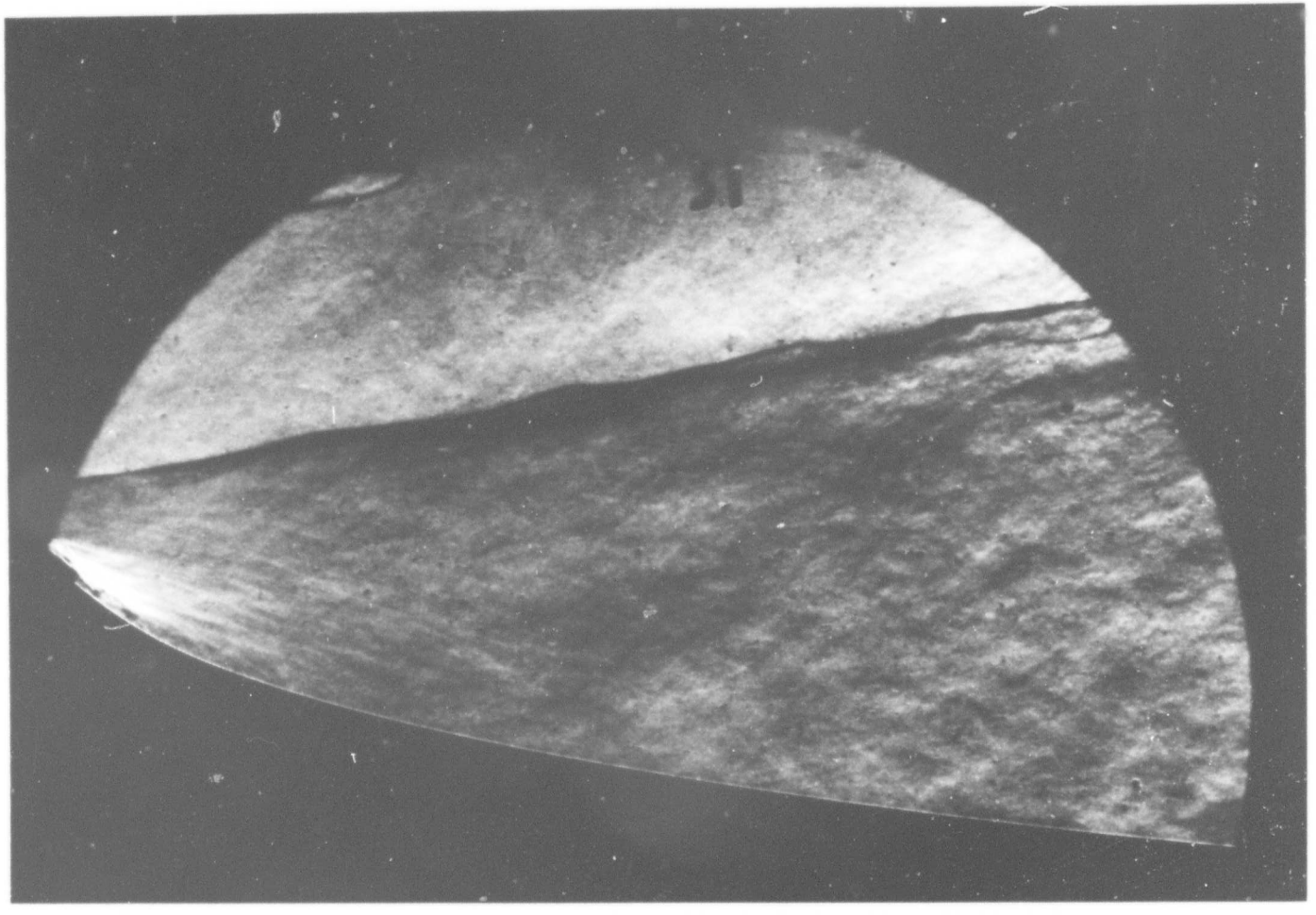

Figure 20 (CONTINUED) (m) AXISYMMETRIC MODEL SCHLIEREN, RUN 31

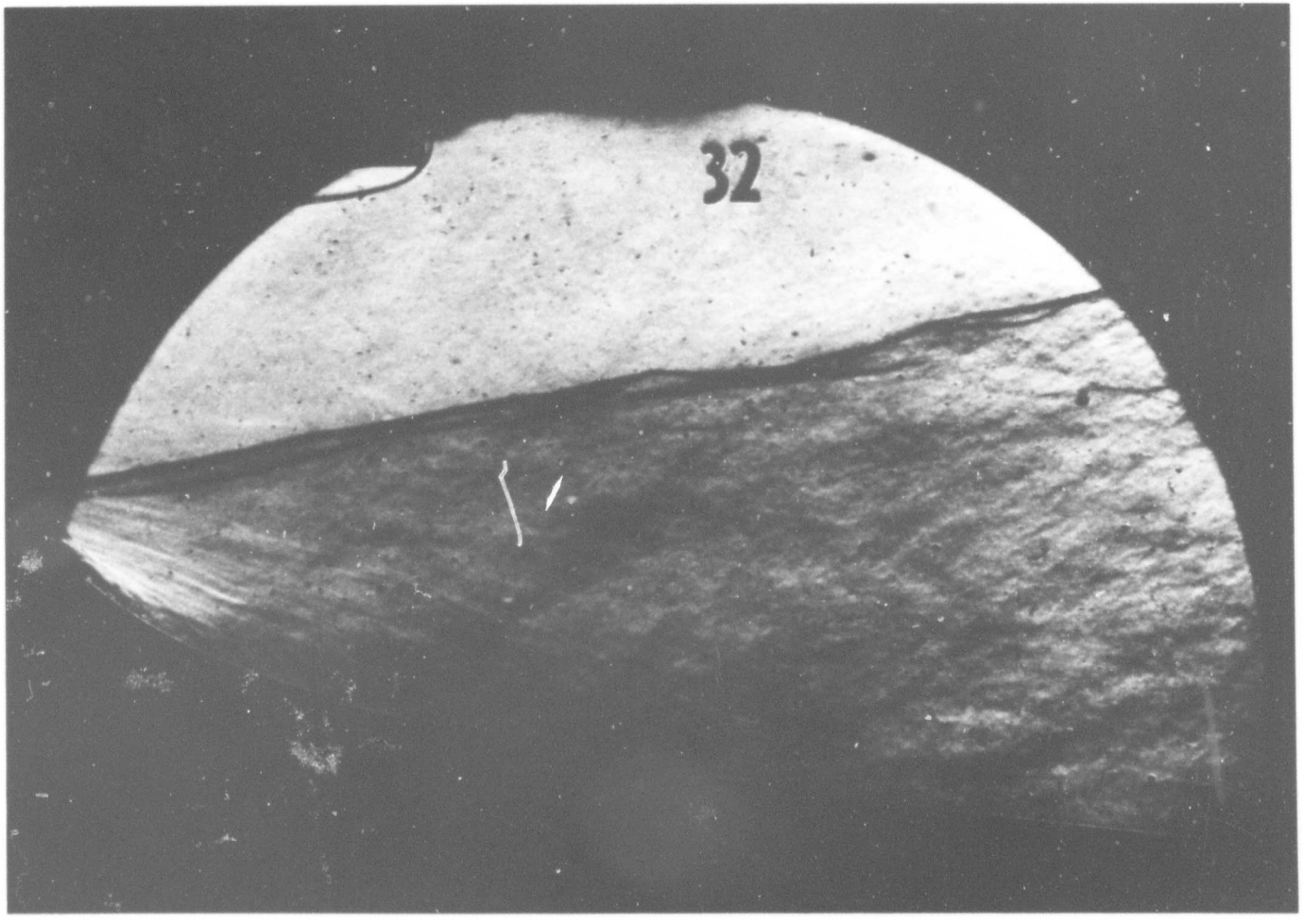

Figure 20 (CONTINUED) (n) AXISYMMETRIC MODEL SCHLIEREN, RUN 32

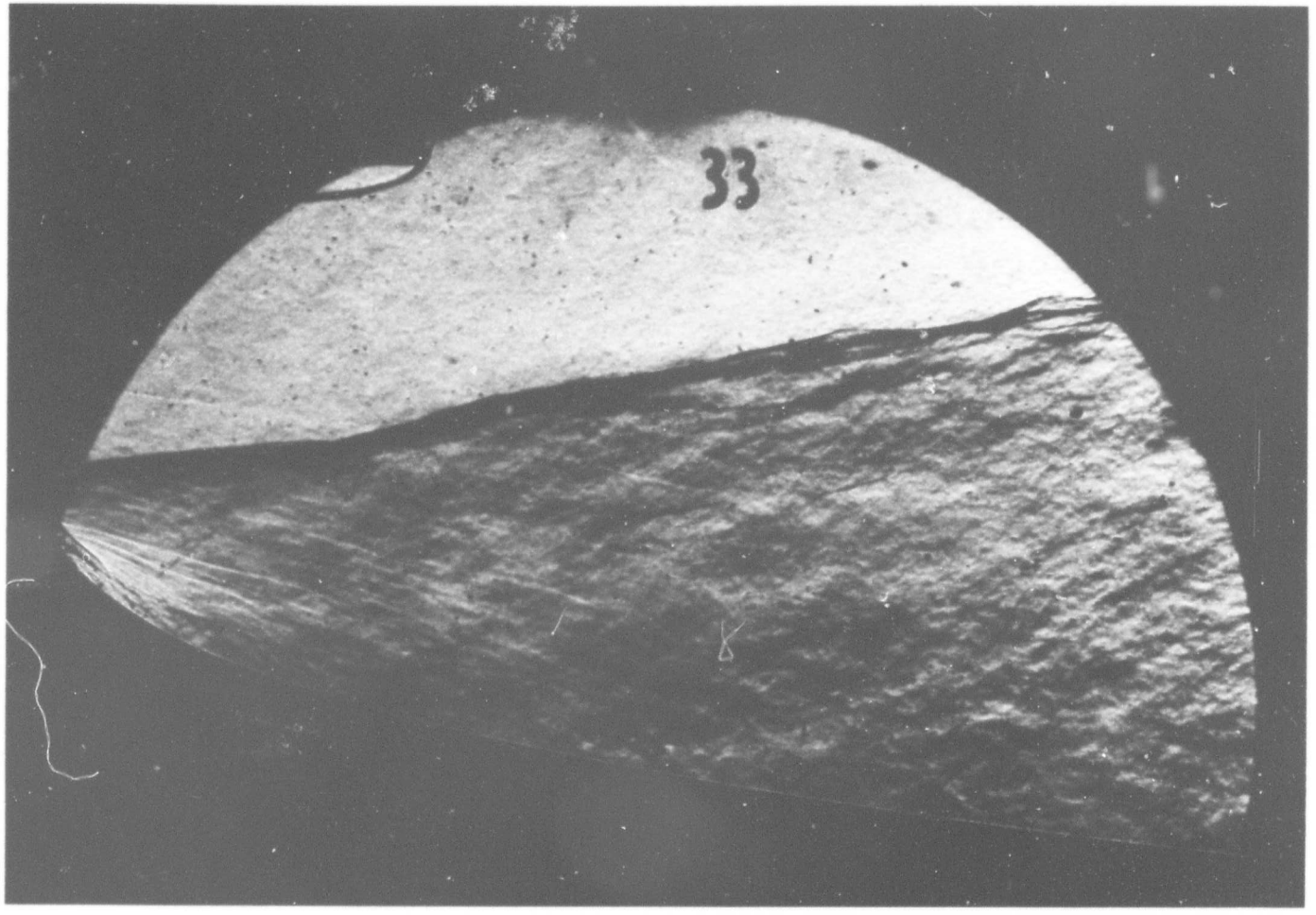

Figure 20 (CONTINUED) (o) AXISYMMETRIC MODEL SCHLIEREN, RUN 33

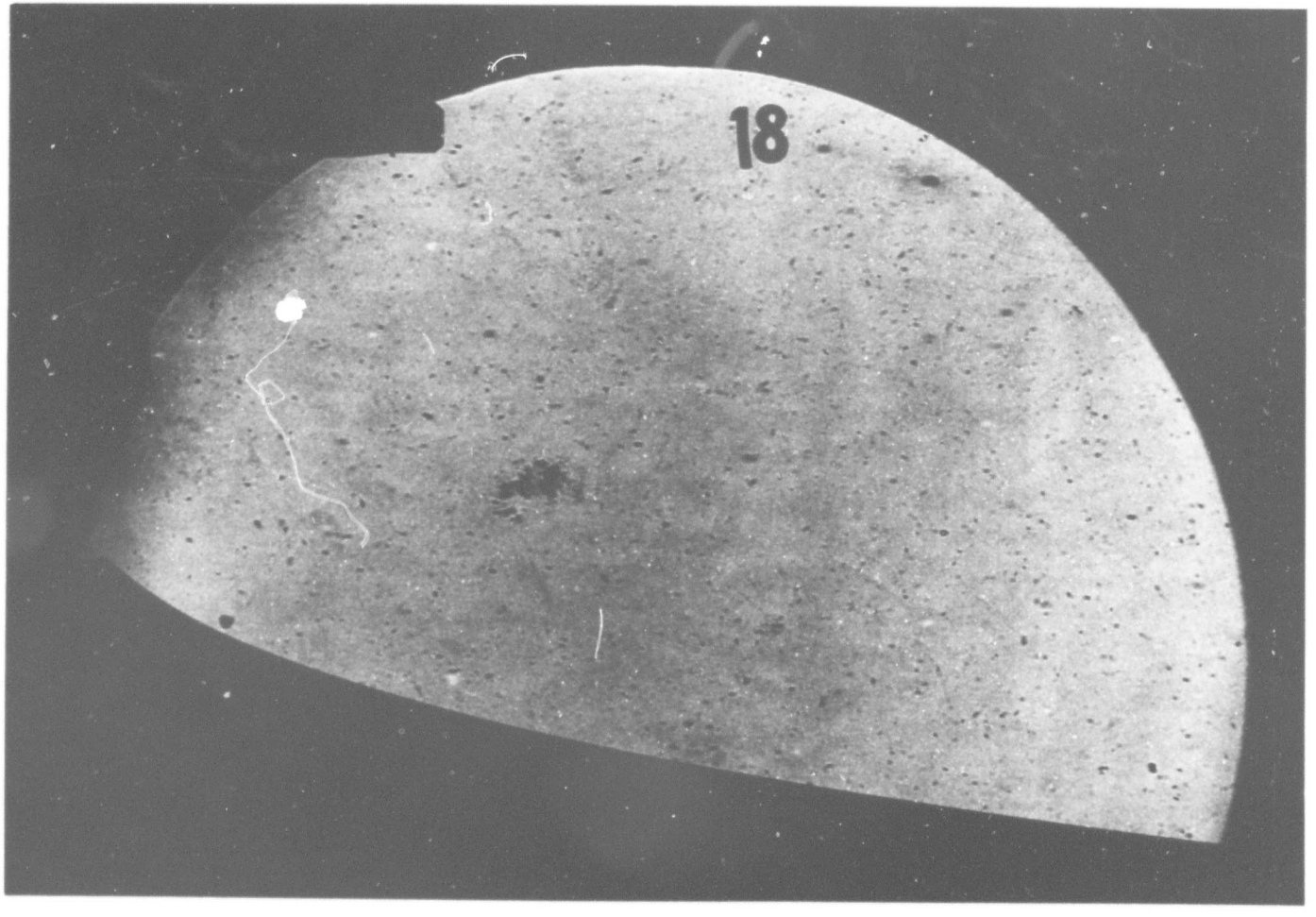

Figure 20 (CONCLUDED) (p) AXISYMMETRIC MODEL SHADOWGRAPH, NO FLOW

Unclassified

Security Classification

DOCUMENT CONTROL DATA - R & D

(Security classification of title, body of abstract and indexing annotation must be entered when the overall report is classified)

1. ORIGINATING ACTIVITY *(Corporate author)*

Cornell Aeronautical Laboratory, Inc.
Buffalo, New York

2a. REPORT SECURITY CLASSIFICATION
Unclassified

2b. GROUP
none

3. REPORT TITLE
Turbulent Boundary Layer Skin Friction, Heat Transfer and Pressure Measurements on Hypersonic Inlet Compression Surfaces.

4. DESCRIPTIVE NOTES *(Type of report and inclusive dates)*
Final Report, January 1967 - July 1968

5. AUTHOR(S) *(First name, middle initial, last name)*

Melvin O. Ryder, Jr.

6. REPORT DATE	7a. TOTAL NO. OF PAGES	7b. NO. OF REFS
July 1968		19

8a. CONTRACT OR GRANT NO.	9a. ORIGINATOR'S REPORT NUMBER(S)
F33615-67-C-1203	AF-2389-Y-3
b. PROJECT NO. 1366	
c. Task No. 136605	9b. OTHER REPORT NO(S) *(Any other numbers that may be assigned this report)*
d.	AFFDL-TR-68-102

10. DISTRIBUTION STATEMENT
This document has been approved for public release and sale; its distribution is unlimited. In DDC, Available from CFSTI

11. SUPPLEMENTARY NOTES	12. SPONSORING MILITARY ACTIVITY
	Air Force Flight Dynamics Laboratory AF Systems Command, Wright-Patterson AFB

13. ABSTRACT

An experimental study of turbulent boundary layer flow, under the influence of adverse pressure gradients typical of hypersonic inlets, was conducted in the Cornell Aeronautical Laboratory 96-inch leg of the Hypersonic Shock Tunnel on a two-dimensional and an axisymmetric model each instrumented with skin friction, heat transfer and pressure gages. Tests were conducted over a Mach and Reynolds number rage of 6.74 to 11.37 and 1.05×10^6 per ft. to 2.93×10^7 per ft., respectively. These test conditions produced boundary layer transition on the forward portions of the models without resorting to artificial trips. It was possible to attain a fully turbulent boundary layer before the start of the adverse pressure gradient region for most of the axisymmetric model tests but for most of the two-dimentional tests, transition was not completed until after the start of the pressure gradient.

A comparison of the pressure data with the inviscid pressure distribution was made and good agreement is generally found indicating very little change in effective model shape due to boundary layer growth. This result is a consequence of the large model size relative to the boundary layer thickness, i.e. high Reynolds number flows over large models.

An important conclusion resulting from this program was that turbulent boundary layers can negotiate large adverse pressure gradients without separating. Comparison with some existing laminar boundary layer data indicate that a turbulent boundary layer can negotiate adverse pressure gradients at least an order of magnitude greater than those gradients which will separate a laminar layer.

DD FORM 1 NOV 65 1473

Unclassified

Security Classification

14. KEY WORDS	LINK A		LINK B		LINK C	
	ROLE	WT	ROLE	WT	ROLE	WT
Turbulent Boundary Layer						
Adverse Pressure Gradients						
Skin Friction						
Hypersonic Inlet						
Heat Transfer						